Novel Electronic Behaviors in Graphene Nanostructures

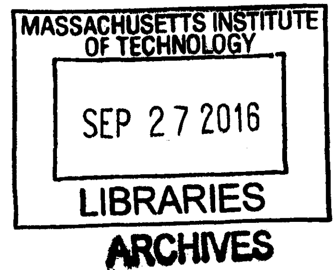

by

Joaquin F. Rodriguez-Nieva

Submitted to the Department of Physics
in partial fulfillment of the requirements for the degree of

Doctor of Philosophy

at the

MASSACHUSETTS INSTITUTE OF TECHNOLOGY

September 2016

© Massachusetts Institute of Technology 2016. All rights reserved.

Author .... Signature redacted
Department of Physics
July 8, 2016

Certified by..................... Signature redacted
Mildred S. Dresselhaus
Professor of Physics
Thesis Supervisor

Certified by............ Signature redacted ....
Leonid S. Levitov
Professor of Physics
Thesis Supervisor

Accepted by............ Signature redacted
Nergis Mavalvala
Professor of Physics
Associate Department Head

Novel Electronic Behaviors in Graphene Nanostructures

by

Joaquin F. Rodriguez-Nieva

Submitted to the Department of Physics
on July 8, 2016, in partial fulfillment of the
requirements for the degree of
Doctor of Philosophy

Abstract

Recently, it has been shown that graphene can be combined with a variety of nanoscale systems, such as other two-dimensional crystals, to form novel electronic nanostructures. These systems inherit the unique characteristics of graphene, such as high mobility, Berry phase, photoresponse mediated by hot carriers, and at the same time aquire new features due to nanoscale heterogenities. In this thesis, I explore the novel electronic behaviors which emerge in this fashion. I focus on two types of systems: (i) vertically-stacked structures in which graphene layers are interspaced with insulating materials and (ii) in-plane structures formed by spatially-varying electrostatic potentials in graphene.

The outline of this thesis is as follows: first, I show that the vertical structures grant access to distinct transport behaviors and new kinds of photoresponse. Those include, in particular, photo-induced negative differential resistance, bistability, and hysteretic I-V characteristics. This wide variety of behaviors is enabled by a number of interesting physical phenomena which can be accessed in these structures, such as resonant tunneling, thermionic emission and field emission. I explore the different knobs which are available to control these phenomena and new ways to employ them to design the I-V response.

Second, I study in-plane nanostructures such as *pn* junction rings induced by local charges, and show that they enable confinement of electronic states in graphene. Confined states in these graphene quantum dots arise due to constructive interference of electronic waves scattered at the *pn* junction and inward-reflected from the ring by the so-called Klein scattering process. Key fingerprints of confined states are resonances appearing periodically in scanning tunneling spectroscopy maps. Besides the novel mechanism for confinement, I also demonstrate that graphene quantum dots can be exploited for accessing exotic and potentially useful behavior which is not available in conventional quantum dots. An example of such behavior is a giant non-reciprocal effect of quantum dot resonances which is induced by the Berry phase.

Third, I study manifestations of defects in the Raman spectral maps of disordered graphene systems. Two salient Raman features, namely the D and D$'$ bands, provide useful information about the nature of defects. I perform a detailed analysis

of the origin of the Raman scattering cross section which is routinely measured in experiments and discuss how it can be used to obtain information about defects.

Overall, this thesis demonstrates the versatility of graphene nanostructures. This is manifested in numerous phenomena which have implications both in basic science, e.g. Berry phase effects, as well as in applied research, e.g. photodetection in graphene Schottky junctions. Furthermore, several of the ideas discussed here can be extended to achieve other interesting and potentially useful effects, such as localized valley-polarized states in graphene quantum dots and exciton confinement.

Thesis Supervisor: Mildred S. Dresselhaus
Title: Professor of Physics

Thesis Supervisor: Leonid S. Levitov
Title: Professor of Physics

To my parents

Acknowledgments

MIT, because of the remarkable people it hosts, has left an indelible mark in my life. Many have left their imprints on me and to many I am deeply indebted.

First, I owe a huge debt of gratitude to my advisor Millie Dresselhaus. Millie inspired me to explore a path in Physics during my first two years at MIT. Having an engineering background, this transition, though hard at first sight, was very natural thanks to her constant encouragement and scientific stimulation. Importantly, she also gave me freedom to discover my own interests and design my own projects. Millie has been been, and will always be, a source of inspiration and a role model for me. Her curious spirit, her scientific productivity, her caring attitude towards students, collaborators, and even strangers, the generosity with her time, her inspiring way of communicating science, have all set new standards for me. Most importantly, I have been particularly touched by her geniune humbleness, which remains pristine regardless of her tremendous impact in carbon science and her countless awards.

I am also immensely indebted to Leonid Levitov. Not only did he play a key role as advisor, but also he was one of the best teachers I ever had; he was crucial to my development as a physicist. I learnt from his illuminating insights and his clarity of thought. His influence also impacted the way I communicate physics. His careful thinking and his precise choice of words made scientific writing a highly enjoyable (and extremely challenging) task. I feel incredibly priviledged to have learnt from him. I am very grateful for his generosity, for showing me how to become a physicist, and for being extremely caring and supportive throughout my time at MIT.

Both Millie and Leonid encouraged me to collaborate with several other remarkable scientist, both at MIT and elsewhere. Of special importance were the collaborations with experimentalists. I am particularly grateful to Joe Stroscio for sharing with me his data, his enthusiasm and his beautiful science. The interaction with him and his group has stimulated many of the ideas I pursued afterwards. I was also very fortunate to collaborate with Michael Crommie's group: I thank Dillon Wong, Juwon Lee and Jairo Velasco for all our scientific dicussions, their insights, and their

enthusiasm to do science together.

I also had the priviledge to work with great theorists. Among them, I am very grateful to Saito-sensei from Tohoku University. His patience, his diligence, and his teachings about carbon materials and Raman spectroscopy were invaluable to me. Also invaluable was interacting with Justin Song. Not only did Justin offer his time generously to feed me with new ideas, but he was also a great source of advice and support.

Many local experimentalists played an important role in my scientific development. I thank Nathan Gabor, Qiong Ma, Javier Sanchez-Yamagishi, Trond Andersen, Nityan Nair for sharing with me their work on graphene nanostructures; Mario Hofman, Yong Cheol Shin, Cosmi Lin, Xi Ling, Sheng-Xi Huang, Paulo Araujo and Daniela Mafra for teaching me about 2D material synthesis and characterization techniques; Albert Liao, Shuang Tang and Ricardo Pablo Pedro for teaching me about topics beyond graphene. I also thanks Prof. Jing Kong for her kindness and support throughout these years, and the many visitors of our group for sharing their work with us, particularly Ado Jorio, Luiz Gustavo Cançado, Marcos Pimenta, Eduardo Barros, Martin Kalbac, Thomas Hirschmann and Gaby Borin. I specially acknowledge Eduardo Barros for sharing with me his knowledge on graphene optics and Raman spectroscopy.

The Condensed Matter division at MIT has always been an extremely friendly and welcoming environment. I am greatly indebted to Patrick Lee for his inspiring solid-state physics class, for his advice, and for his teachings while I was a TA. I also thank Pablo Jarillo-Herrero and Joe Checkelsky for their extremely supportive and enthusiastic role as thesis committee. I am also very priviledged to have interacted with Brian Skinner, Inti Sodemann, Cyprian Lewandowski and Phong Vo.

Three people are fundamental for our group to function smoothly. I thank Read Schusky and Laura Doughty for their constant help during my Ph.D. Also essential for our group is Gene Dresselhaus; thank you Gene for your cheerfulness and support.

My work would not have been possible without the support of the National Science Foundation (NSF) and the MIT Department of Physics. In particular, I acknowledge

support via the NSF grants DMR-1004147 and DMR-1507806 as well as via TAs in the MIT Department of Physics.

I am also greatly indebted to Eduardo Bringa and Javier Fernandez; back in Argentina, they first introduced me to scientific research and encouraged me to pursue a doctoral degree. I also acknowledge the Balseiro Institute, in Bariloche, for giving me the tools to pursue a career in science.

Several people have made significant contributions to make my life in Cambridge even more enjoyable. For this, I thank Franco Mangiarotti, Denis Loginov, Mikhail Volkov, Andres Abin, Tushar Kulkarni, Kelvin Ng, Sema Ermez, Kunal Mukherjee, Christina Chang, Silvia Espinosa-Gutiez and Emilio Alverne.

For making me feel like at home, I thank Belinda, Marc, Isaac, Anne and Charlie. I greatly appreciate all their invitations for Thanksgiving, Easter and summers in the beach, which gave me a break from the busy life in Cambridge.

Of special importance in my life is Lili Yu, with whom I shared epic adventures. I thank her for being an endless source of support, for constantly challenging me and for driving me to become a better person.

Finally, I thank my brothers, Ricardo and Juan, my parents and grandparents for being a constant source of love and encouragment every single day of my life. My parents have been key in my personal development; I feel grateful for the education based on honesty and hard work that they imparted to me, and for their continuous motivation to pursue my dreams.

Contents

1 Introduction **21**

1.1 A brief overview of graphene 21

1.2 Graphene-based nanostructures 23

1.3 Thesis outline 24

2 Graphene theory **27**

2.1 The graphene lattice 27

2.2 Graphene electrons 29

2.2.1 Static electromagnetic fields 32

2.3 Chiral nature of graphene carriers 33

2.3.1 Helicity 34

2.3.2 Absence of backscattering and Klein tunneling 34

2.3.3 Berry phase and semiclassical quantization 36

2.4 Graphene-light interaction 39

2.4.1 Universal light absorption coefficient 39

2.4.2 Electron lattice cooling and hot carriers 40

2.5 Electrostatic doping and quantum capacitance 42

I Transport in vertical graphene nanostructures **45**

3 Interlayer transport in graphene nanostructures **47**

3.1 Tunability of graphene heterostructures 47

3.2 Vertical transport regimes 50

3.3 Features of vertical transport in graphene 51

4 Resonant tunneling and intrinsic bistability in twisted graphene nanostructures 53

4.1 Bistability in graphene nanostructures 54

4.2 Sequential tunneling model 57

4.3 Electrostatic feedback 61

4.4 Model parameters 62

4.5 Bistable characteristics 63

4.6 Quantum capacitance effects 67

4.7 Other graphene-based bistable systems 68

4.8 Chapter summary 69

5 Thermionic emission and negative dI/dV in photoactive graphene heterostructures 71

5.1 Thermionic transport 72

5.2 Negative differential resistance (NDR) 74

5.3 Thermionic transport model 76

5.4 Electrostatic coupling model 77

5.5 Current-bias characteristics 78

5.6 Hot carrier effects 79

5.7 Zero bias doping effect 83

5.8 Criterion for NDR 83

5.9 Additional comments 86

5.10 Chapter summary 87

6 Thermionic-dominated photoresponse in graphene Schottky junctions 89

6.1 Electronic and optical properties of graphene Schottky junctions . . . 90

6.2 Vertical photocurrent model 94

6.3 Photoresponse in the ideal limit 97

6.4 Photoresponse in real systems 98
6.5 Important features of g/X photodetectors 100
6.6 Chapter summary 101

II Electron-optics behavior in graphene quantum dots 103

7 Graphene quantum dots 105
7.1 Whispering gallery modes in graphene 106
7.2 Description of the NIST experiment 109
7.3 Model for graphene whispering gallery modes 111
7.3.1 Fringe duplicity in the STM spectral maps 114
7.3.2 Electrostatic modeling 115
7.3.3 Model parameters 116
7.3.4 Other experimental features 117
7.4 Discussion 119

8 Berry phase and giant non-reciprocity in Dirac quantum dots 121
8.1 Non-reciprocity in Dirac quantum dots 122
8.2 Non-reciprocity: semiclassical model 122
8.3 Features of the non-reciprocal effect 124
8.4 Non-reciprocity: quantum model 126
8.4.1 Electrostatic potential modeling 127
8.4.2 Details of the numerical simulation 128
8.4.3 Quantum model results 129
8.5 Semiclassical quantization 131
8.6 Semiclassical analysis of quantum dot resonances 133
8.7 Semiclassical equations of motion 134
8.8 Discussion 135
8.9 Chapter summary 136

III Photophysics in disordered graphene systems **137**

9 Disorder-induced Raman spectroscopy **139**

9.1 Current status of the double resonance theory 140

9.2 Raman intensity calculation 143

9.2.1 Effective Hamiltonian description 146

9.3 Phase interference effects: phonon momentum selectivity and relevant diagrams 148

9.4 Integrated Raman intensity 151

9.4.1 Details of the Raman intensity calculations 153

9.4.2 Comparison with experiments 157

9.5 Discussion 159

9.6 Chapter summary 160

10 Conclusions **163**

Bibliography **167**

Index of Notation

Fundamental constants:

$\hbar$: Planck's constant over 2π [$= 1.054571800(13) \times 10^{-34}\,\mathrm{J \cdot s}$].

e: electron charge [$= 1.6021766208(98) \times 10^{-19}\,\mathrm{C}$].

k_{B}: Boltzmann constant [$= 1.38064852(79) \times 10^{-23}\,\mathrm{J/K}$].

c: speed of light ($= 299792458\,\mathrm{m/s}$).

m_e: electron rest mass [$= 9.10938215(45) \times 10^{-31}\,\mathrm{kg}$].

α: fine-structure constant ($= e^2/\hbar c$).

Graphene-related constants:

v_{F}: graphene Fermi velocity ($\approx 10^6\,\mathrm{m/s}$).

a_0: carbon-carbon distance in graphene ($= 1.42\,\mathrm{Å}$).

t: carbon-carbon nearest neighbor coupling strength ($\approx 2.8\,\mathrm{eV}$).

ρ: graphene mass density ($\approx 7.6 \times 10^{-11}\,\mathrm{kg/cm^{-2}}$).

ω_0: optical phonon frequency ($\hbar\omega_0 \approx 0.2\,\mathrm{eV}$).

c_{s}: sound velocity ($\approx 2 \times 10^4\,\mathrm{m/s}$).

N_{s}, N_{v}: spin and valley degeneracy ($= 2$).

λ_{abs}: absorption coefficient ($\approx 2.3\,\%$).

$\mathbf{K}, \mathbf{K}'$: inequivalent corners of the graphene hexagonal Brillouin zone.

General notation:

$\boldsymbol{\sigma}$: Pauli matrices, $\boldsymbol{\sigma} = (\sigma_x, \sigma_y, \sigma_z)$.

$\boldsymbol{r}$: position vector.

$\boldsymbol{p}$, $\boldsymbol{q}$, $\boldsymbol{k}$: canonical momentum, kinetic momentum, and wavevector.

ε: electron energy (also ε_i when specifying quantum number i).

m_e^*: electron effective mass.

γ: particle lifetime.

m: azimuthal quantum number.

ψ, ψ': two-component electronic wavefunction near the K and K$'$ points.

Ψ: four-component electronic wavefunction including sublattice and valley pseudospin.

T, T_0: electronic and lattice temperature.

μ: chemical potential.

n_i: graphene carrier density of layer i.

D: density of states.

$A_{i,s}$: electron spectral function of layer i and band s.

f, $f_{\rm B}$: Fermi-Dirac and Bose-Einstein distribution functions.

T: transmission probability.

$\boldsymbol{A}$, U: vector and scalar electromagnetic potentials.

B: magnetic field.

E: electric field.

ℓ_B: magnetic length.

ℓ_U: characteristic length of electrostatic potential.

$\ell_{\rm d}$: characteristic disorder length.

$\ell_{\rm wkb}$: WKB decay length.

S: system surface area.

V: system volume.

$N_{\rm u}$: Number of unit cells in the graphene lattice.

$\tilde{\boldsymbol{A}}_{\boldsymbol{q}}$: Berry connection.

$\varphi_{\rm B}$, $\varphi_{\rm orb}$: Berry phase and orbital phase.

$\mathcal{C}, S(\mathcal{C})$: semiclassical electron path and surface inside $\mathcal{C}$.

$\boldsymbol{m}_{\boldsymbol{q}}$: orbital magnetic moment.

ν: Maslov index.

Electron operators

$\hat{\mathcal{H}}_0$, $\hat{\mathcal{H}}$: bare and full Hamiltonian.

$\hat{\mathcal{H}}_{\rm er}, \hat{\mathcal{H}}_{\rm ep}, \hat{\mathcal{H}}_{\rm d}$: electron-radiation, electron-phonon and electron-disorder coupling.

$\hat{c}_{i,\alpha}, \hat{c}^{\dagger}_{i,\alpha}$: creation and destruction operators at i-unit cell, sublattice $\alpha = A, B$.

$\hat{\psi}$, $\hat{\psi}^{\dagger}$, $\hat{\psi}'$, $\hat{\psi}'^{\dagger}$: electron annihilation and creation operator at the K and K′ points.

$\hat{\Psi}$, $\hat{\Psi}^{\dagger}$: electron annihilation and creation operator.

Photon-related quantities and operators:

$\boldsymbol{Q}$, λ: photon wavevector and polarization mode.

$\boldsymbol{e}_{\boldsymbol{Q},\lambda}$: photon polarization vector.

$\hat{a}_{\boldsymbol{Q}\lambda}, \hat{a}^{\dagger}_{\boldsymbol{Q}\lambda}$: photon annihilation and creation operators.

Phonon-related quantities and operators:

$\boldsymbol{q}_{\rm ph}$, β: phonon wavevector and phonon mode.

$\boldsymbol{e}_{\boldsymbol{q}_{\rm ph},\beta}$: acoustic phonon polarization vector.

$\omega_{\boldsymbol{q}_{\rm ph},\beta}$: phonon frequency.

$\hat{b}_{\boldsymbol{q}_{\rm ph},\beta}, \hat{b}^{\dagger}_{\boldsymbol{q}_{\rm ph},\beta}$: phonon annihilation and creation operators.

F_{μ}: force constant.

U_D: deformation potential energy.

Graphene nanostructure parameters:

$V_{\rm b}, V_{\rm g}$: bias and gate potential.

$E_{\rm b}$: electric field between biased graphene layers.

Φ: Schottky barrier height.

d: interlayer distance (also d_{ij} when specifying layers).

θ: twist angle.

$\boldsymbol{q}_{A,B,C}$: K-point displacement in a twisted bilayer system.

$\varphi_{A,B,C}$: angle of vector $\boldsymbol{q}_{A,B,C}$.

$\mathcal{T}_{\alpha\beta}$: tunneling coupling matrix element.

$n_{\rm g}$: carrier density in the gate.

$\epsilon_{\rm r}$: dielectric constant.

Transport variables:

$t_{\perp}$: tunneling coupling.

I_{ij}: interlayer tunneling current between layers i and j

V_{ij}: bias potential between layers i and j.

ϕ_{ij}: electrostatic potential between layers i and j.

G_{ij}: interalayer tunneling conductance between layers i and j.

g_{ij}: interlayer tunneling conductance per unit area between layers i and j.

P_{in}, P_{abs}: incident and absorbed power per unit area.

$P_{\text{ac}}, P_{\text{d}}, P_{\text{opt}}$: acoustic, disorder-assisted and optical phonon cooling power (per unit area).

P_{loss}: power losses (per unit area).

Z: conductance ratio.

$\mathcal{R}, \mathcal{R}_0$: optoelectronic responsivity and optimal responsivity.

χ: dimensionless responsivity.

STM-induced graphene quantum dot:

B_{c}: critical magnetic field for spectral non-reciprocity.

κ: curvature of the electrostatic potential.

r_*, ε_*, B_*: characteristic units of distance, energy and magnetic field.

V_{cpd}: contact potential difference.

R: STM tip radius.

Raman notation:

E_{L}: laser energy.

I_{D}, I_{G}: Raman intensity of the D and G bands.

n_{d}: defect concentration.

$\mathcal{I}_{\text{DR}}$: double resonance Raman probability.

$\mathcal{M}_{ij}^{\alpha}$: interaction matrix element.

List of Figures

2-1 Hexagonal graphene lattice and graphene band structure. 28

2-2 Klein tunneling of Dirac electrons. 36

2-3 Dominant cooling mechanism in graphene. 42

2-4 Quantum capacitance effects in graphene nanostructures. 43

3-1 Tunable parameters in graphene-based nanostructures. 49

3-2 Vertical transport regimes in graphene-dielectric-graphene nanostructures. 51

4-1 Bistable I-V response of a trilayer graphene heterostructure. 55

4-2 Hexagonal superlattice of twisted graphene layers. 59

4-3 Regions in $\boldsymbol{k}$-space contributing to the resonant tunneling current for fixed V. 64

4-4 Self-consistent bistable solutions including quantum capacitance effects. 68

5-1 The Negative Differential Resistance (NDR) effect in a photoactive heterostructure operated in the thermionic emission regime. 73

5-2 The closed-circuit current I_{cc} induced by optical pumping. 75

5-3 Map of the open-circuit current I induced by optical pumping. 81

5-4 Photoresponse as a function of pump power and disorder. 85

6-1 Thermionic-dominated heat transport in a graphene Schottky junction. 91

6-2 Graphene/X Schottky junction photoresponse. 96

7-1 Confined electronic states in microscopic electron cavities defined by pn junction rings in graphene. 107
7-2 Confined electronic states probed by STM measurements from NIST. 110
7-3 Contributions of the WGM resonances with different m to the DOS for the relativistic Dirac model. 112
7-4 Radial Fermi energy profile obtained from the Thomas-Fermi model. . 118

8-1 Manipulation of the Berry phase $\varphi_{\rm B}$ of confined Dirac electrons using magnetic fields. 123
8-2 Magnetic response of quantum dot resonances in a gapless Dirac system. 125
8-3 Modeling of the electrostatic potential. 128
8-4 Spectral maps showing the splitting of periodic time-reversed resonances under weak magnetic fields in (a) gapless and (b) gapped Dirac quantum dots. 130
8-5 Off-centered spectral maps for a gapless Dirac quantum dot displaying large m splitting of resonances in weak magnetic fields. 131
8-6 Topologically distinct mappings of $\boldsymbol{q}$ to the surface of a torus. 132
8-7 Comparison between semiclassical and quantum models. 134

9-1 Dependence of the integrated Raman intensity on laser energy and impurity density. 142
9-2 Feynman diagrams contributing to the double resonant Raman scattering process. 149
9-3 Dominant phonon modes contributing to the Raman peak. 150
9-4 Momenta where the double resonance conditions are satisfied. 154

Chapter 1

Introduction

Graphene is a monolayer of carbon atoms tightly packed into a two-dimensional (2D) honeycomb lattice with exceptionally high crystal quality. Since it was first isolated in 2004 [1], the graphene field burgeoned into a dynamic research area with several thousands of papers published each year. Intrinsic graphene hosts a wide range of intriguing phenomena which result from its unique combination of electronic, chemical, mechanical and optical properties. As recently shown, graphene-based nanostructures, which result from combining graphene with other nanoscale systems, host new behaviors not present in bare graphene. In this chapter, I present a broad overview of the graphene field, with special emphasis on the intrinsic properties of graphene and the recent advances in nanostructure fabrication.

1.1 A brief overview of graphene

Despite the recent growth of the field, two of graphene's salient electronic characteristics were predicted several decades ago, well before graphene was a reality [2–4]. First, in 1946, P. R. Wallace uncovered the unusual semimetallic behavior of graphite monolayers. Although originally intended to describe graphite, Wallace's work set the grounds to describe other carbon-based materials, such as fullerenes, carbon nanotubes and graphene itself. Forty years later, it was realized that graphene provides a condensed matter analogue of (2+1)-dimensional quantum electrodynamics

(QED) [5–7]. In particular, electrons in graphene mimick the quantum electrodynamics of massless fermions, except for the fact that in graphene Dirac fermions move with a speed 300 times smaller than the speed of light.

These unique electronic properties of graphene are condensed in the low energy Hamiltonian, valid for energies $|\varepsilon| \lesssim 1\,\mathrm{eV}$, describing charge carriers in graphene:

$$v_\mathrm{F}(\boldsymbol{\sigma} \cdot \boldsymbol{p})\psi(\boldsymbol{r}) = \varepsilon\psi(\boldsymbol{r}). \quad (1.1)$$

Here $v_\mathrm{F} \approx 10^6\,\mathrm{m/s}$ is the Fermi velocity for electrons and holes, and $\boldsymbol{p} = -i\hbar\partial_{\boldsymbol{r}}$ is the momentum operator. This effective Hamiltonian arises from the covalent bonding of p_z orbitals in the hexagonal graphene lattice. As first pointed out by Wallace, the Dirac Hamiltonian in Eq.(1.1) gives rise to a conical bandstructure $\varepsilon_{\boldsymbol{k},\pm} = \pm\hbar v_\mathrm{F}|\boldsymbol{k}|$, with $\boldsymbol{k}$ the electron wavevector. Given that in neutral graphene the chemical potential crosses exactly at the Dirac point, graphene is a zero-gap semiconductor, i.e. a semimetal.

The close connection with QED is manifested in the two-component nature of $\psi(\boldsymbol{r})$ in Eq.(1.1): electronic states in graphene are composed of states belonging to two different sublattices, and their relative contributions to the total wavefunction $\psi(\boldsymbol{r})$ needs to be taken into account. This is similar to the spin index in QED and, therefore, is referred hereafter as sublattice pseudospin. Pseudospin-related effects in graphene can dominate those due to the real spin. One such effect is the so-called Klein tunneling, which allows unit transmission through classically forbidden regions.

In addition, graphene has a wide range of other interesting properties. The exposed nature of graphene's 2D electronic states enables direct probing of such states. This feature contrasts with conventional 2D materials such as GaAs heterostructures, where the electronic states are deeply buried. Graphene is also characterized by a pronounced ambipolar electric field effect [1], such that charge carriers can be tuned continuously between electrons and holes in concentrations as high as $10^{13}\,\mathrm{cm}^{-2}$. This knob enables experimentalists to control, for instance, the strength of electron-electron interactions or the electron-phonon scattering rate. Graphene also features

micrometer scale ballistic transport at room temperature [8, 9] and low temperature carrier mobilities in suspended devices on the order of $\sim 10^6\,\mathrm{cm^2V^{-1}s^{-1}}$ [10]. This grants access to electron-optics behavior in graphene, such as electronic lenses and resonators. When compared to ordinary electrons, electrons in graphene also behave in unusual ways if subjected to magnetic fields. This leads to new physical phenomena, such as the anomalous integer quantum hall effect which can be observed even at room temperatures [11] (a further indication of the system's extreme electronic quality).

1.2 Graphene-based nanostructures

The unique electronic behaviors of graphene have been the object of intense research during the last decade. While many questions regarding intrinsic graphene remain open, particularly in the many-body physics realm, the graphene field has by now reached maturity. For this reason, and motivated by graphene's intrinsic stability, researchers have applied graphene synthesis techniques to many layered materials which can potentially be exfoliated.[1] Successfully synthesized crystals include hBN, MoS_2, WS_2, WSe_2 and $MoSe_2$.[2] As a result, graphene can now be assembled into designer electronic heterostructures made layer-by-layer in any determined sequence. The resulting stack represents an artificial material assembled with blocks defined with one atomic plane precision. While lateral covalent bonds provide in-plane stability, weak van der Waals forces keep the stack stable. This emerging research field, graphene-based nanostructures, has been gaining momentum in the last few years.

There has already been important progress in this field. Graphene was first combined with hBN, which was demonstrated to serve as a high-quality substrate for graphene [14]. Afterwards, few layers of hBN, MoS_2 and WS_2 were used as tunnel barriers for two graphene electrodes in vertically-stacked devices. Fabricated with

[1] Of the thousands of materials that can potentially be exfoliated, not all are stable. In some cases, the melting temperature is dramatically decreased for a nanometer scale thickness; in other cases, the materials are highly reactive or corrosive.

[2] Some of these are interesting on their own; for instance, MoS_2 has broken centro-symmetry, which allows efficient spin and valley polarization by optical pumping [12, 13].

atomic precision, such devices operated as field-effect transistors [15, 16], resonant tunneling diodes [17, 18] and photodetectors [19, 20]. Such heterostructures also provided a platform to explore the Coulomb Drag effect [21] and the metal-insulator transition [22].

More recently, crystallographic alignment of 2D monolayers (with an accuracy of less than 1°) became possible. This results in Moiré patterns that depend on the rotation angle between two adjacently stacked crystals and their lattice mismatch. Two notable examples include twisted graphene bilayers [23, 24] and graphene-hBN superlattices [25,26]. The resulting van der Waals heterostructures exhibit optical and electronic properties distinct from its constituent components as well as interesting collective phenomena.

Graphene has also been combined with local charges to uncover exotic electronic behaviors. One such example is the atomic collapse of electronic states [27]. This unique behavior arises from the relativistic behavior of graphene charge carriers with a fine-structure constant which is enhanced by a factor $c/v_{\mathrm{F}} \approx 300$ [28–30].

1.3 Thesis outline

In this thesis, I explore new electronic behaviors induced by nanoscale heterogeneity in graphene nanostructures. In this direction, I explore two different ways to manipulate electronic states: (i) by vertically stacking graphene in-between monolayers of insulating materials and (ii) by patterning local electrostatic potentials in graphene. As we will see, these systems inherit the unique electronic properties of graphene (Chapter 2), and acquire new electronic behaviors due to nanoscale heterogeneity.

In Part 1, I explore the vertical transport in graphene nanostructures. Transport in such structures feature a wide range of interesting regimes, such as resonant tunneling, thermionic emission and field emission (Chapter 3). Transition between these regimes gives rise to distinctive behaviors which include intrinsic bistability (Chapter 4), photo-induced negative differential resistance (Chapter 5) and highly-sensitive photoresponse mediated by hot carriers (Chapter 6). I also explore the knobs which

are available to control these phenomena. In particular, these knobs arise from the various 2D insulating materials (e.g. hBN, MoS_2, WSe_2) which can be combined with graphene. Furthermore, I also stress that vertical nanostructures have other features of interest. For instance, the short interlayer transport lengths facilitate extraction of carriers, enabling ultra-fast response times while minimizing losses. In the context of optoelectronics, vertical heterostructures can also exploit the entire active area of graphene; this contrasts from graphene-based pn junction photodetectors where the active area is a negligibly small stripe centered on the pn region.

In Part 2, I study optics-inspired behavior in graphene quantum dots. First, I show that pn junction rings enable confinement of electronic states in graphene (Chapter 7). Such pn rings, acting as the boundaries of the graphene quantum dot, are induced by patterning an electrostatic potential in graphene, e.g. by local charges. I also show that the pseudospin degrees of freedom grants access to novel behaviors which are not available in conventional quantum dots. In particular, I predict a giant-nonreciprocal effect of the quantum dot spectrum which is induced by the Berry curvature in graphene (Chapter 8).

In Part 3, I consider the photophysics of disordered graphene systems. Disorder produces distinctive Raman features in the optical spectra of graphene, namely the D and D$'$ bands. I perform a detailed analysis of the origin of the Raman scattering cross section, which is routinely measured in experiments, and discuss how it can be used to obtained information about disorder (Chapter 9).

Finally, in Chapter 10, the main results of this work are summarized and potential extensions of our work are discussed.

Chapter 2

Graphene theory

In this chapter, I introduce the basic theoretical aspects of the graphene theory which will be recurrent in subsequent chapters. In addition to the electronic description within the Dirac theory, recurrent topics include Dirac electrons embedded in electromagnetic fields and the interaction between graphene and light. Several sections of this chapter are dedicated to discuss some of the peculiar phenomena that make graphene a unique electronic system. Naturally, there are many excellent reviews on every single topic discussed in this chapter [31–33]; special emphasis will be given to the essential elements necessary to make this thesis self-contained. For the experts in the field, this chapter serves as an introduction to the notation that will be used hereafter (see also index of notation).

2.1 The graphene lattice

The graphene lattice is comprised of carbon atoms arranged in a two-dimensional hexagonal structure [Fig.2-1(a)]. The carbon atoms are bound in-plane by sp^2 hybridization: one s orbital and two p orbitals ($p_{x,y}$) form a σ bond. The p_z orbital, which is perpendicular to the graphene plane, can also bind covalently with its nearest neighbours and form the π-bond. The σ bond is mainly responsible for the large stiffness and high crystal quality of the crystal, whereas the π-bond is responsible of the unique electronic properties of graphene.

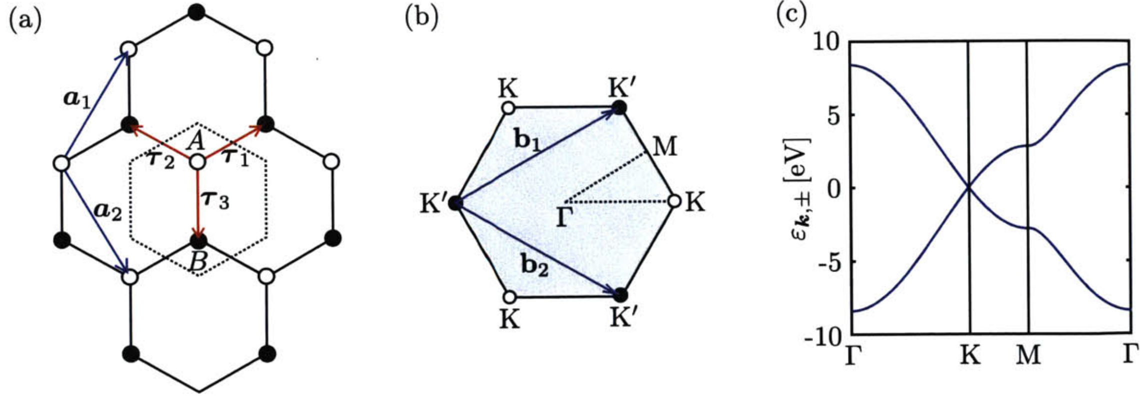

Figure 2-1: Hexagonal graphene lattice and graphene band structure. (a) Shown is the hexagonal lattice comprised of sublattice A (open circles) and B (closed circles), with translation vector $\boldsymbol{a}_{1,2}$. The vector $\boldsymbol{\tau}_{1,2,3}$ indicate the nearest neighbor vectors with magnitude $a_0 \approx 1.42\,\text{Å}$. (b) Hexagonal Brillouin zone of graphene displaying high symmetry points: the zone-center Γ-point, the zone boundary M-point, and the two inequivalent corners K and K′. Here $\boldsymbol{b}_{1,2}$ are the reciprocal lattice vectors. (c) Electronic band structure corresponding to the p_z orbital in carbon (i.e. the π band). Notably, the band structure is conical in the vicinity of the K and K′ points, with this behavior persisting up $\sim 1\,\text{eV}$.

The hexagonal structure can be described as a triangular lattice with a two atom basis. The two elements of the basis — two carbon atoms indicated with open and closed circles in Fig.2-1(a) — are labelled A and B. Each atom in sublattice A is surrounded by three atoms in sublattice B with nearest neighbour vectors

$$\boldsymbol{\tau}_1 = a_0(\sqrt{3}/2, 1/2), \quad \boldsymbol{\tau}_2 = a_0(-\sqrt{3}/2, 1/2), \quad \boldsymbol{\tau}_3 = a_0(0, -1), \tag{2.1}$$

where $a_0 = 1.42\,\text{Å}$ is the carbon-carbon distance in graphene. In addition, the translation vectors for the A and B sublattices are

$$\boldsymbol{a}_1 = a_0(\sqrt{3}/2, 3/2), \quad \boldsymbol{a}_2 = a_0(\sqrt{3}/2, -3/2). \tag{2.2}$$

In reciprocal space, the hexagonal lattice defines a hexagonal Brillouin zone (BZ), which is rotated 90° with respect to the unit cell [see Fig.2-1(b)]. The reciprocal vectors of the BZ are

$$\boldsymbol{b}_1 = \frac{4\pi}{3a_0}(\sqrt{3}/2, 1/2), \quad \boldsymbol{b}_2 = \frac{4\pi}{3a_0}(\sqrt{3}/2, -1/2). \tag{2.3}$$

Of special importance in graphene are the six corners of the hexagonal BZ, the so-called Dirac points. It is clear that, because $\boldsymbol{b}_1$ and $\boldsymbol{b}_2$ connect one corner of the BZ with another two [Fig.2-1(b)], the six corners of the BZ fall into two groups. For each group, labelled K and K′ in Fig.2-1(b), only two distinct coordinates need to be considered:

$$\mathbf{K} = \frac{4\pi}{3\sqrt{3}a_0}(1,0), \quad \mathbf{K}' = -\mathbf{K}. \tag{2.4}$$

As we will see, most of the interesting physics in graphene occurs in the vicinity of these points.

2.2 Graphene electrons

The simplest model to describe graphene electrons is a one-parameter tight-binding model that couples nearest-neighbor p_z orbitals:

$$\hat{\mathcal{H}} = -t\sum_{\langle i,j\rangle} \hat{c}^\dagger_{i,A}\hat{c}_{j,B} + \text{h.c.}. \tag{2.5}$$

Here $\hat{c}_{i,\alpha}$ ($\hat{c}^\dagger_{i,\alpha}$) is the annihilation (creation) operator of an electron in a p_z orbital located in the i-th unit cell, sublattice α ($\alpha = A, B$), $t \approx 2.8\,\text{eV}$ is the nearest neighbor coupling strength and $\sum_{\langle i,j\rangle}$ denotes summation over nearest neighbours. Given that only spin-independent phenomena will be considered, I exclude the spin index in the notation and include spin degeneracy at the end of the calculations.

Importantly, the simple tight-binding description in Eq.(2.5) works because the bands associated with the $p_{x,y}$ and σ orbitals have relatively large energies $|\varepsilon_{p_x,p_y,\sigma}| \gtrsim 3\,\text{eV}$ referred to the Fermi level. Therefore, these bands have negligible contributions to all the phenomena of interest in this thesis, such as transport or interaction with light.

Replacing the operators $\hat{c}_{i,A}$ and $\hat{c}_{i,B}$ in Eq.(2.5) with their Fourier transforms,

$$\hat{c}_{\boldsymbol{k},\alpha} = \frac{1}{\sqrt{N_\text{u}}}\sum_i e^{i\boldsymbol{k}\cdot\boldsymbol{r}_{i,\alpha}}\hat{c}_{i,\alpha}, \quad \alpha = A, B, \tag{2.6}$$

results in

$$\hat{\mathcal{H}} = \sum_{\boldsymbol{k},\alpha\beta} \mathcal{H}_{\boldsymbol{k},\alpha\beta} \hat{c}^{\dagger}_{\boldsymbol{k},\alpha} \hat{c}_{\boldsymbol{k},\beta}, \quad \mathcal{H}_{\boldsymbol{k}} = \begin{pmatrix} 0 & \gamma_{\boldsymbol{k}} \\ \gamma^*_{\boldsymbol{k}} & 0 \end{pmatrix}, \quad \gamma_{\boldsymbol{k}} = -t \sum_{j=1,2,3} e^{-i\boldsymbol{k}\cdot\boldsymbol{\tau}_j}. \tag{2.7}$$

Here $\boldsymbol{k}$ is a wavevector within the BZ, N_{u} is the number of unit cells in the graphene crystal, and $\boldsymbol{r}_{i,\alpha}$ is the position of the atom in the i-th unit cell, sublattice α. The energy spectrum of $\mathcal{H}$, shown in Fig.2-1(c), is

$$\varepsilon_{\boldsymbol{k},\pm} = \pm|\gamma_{\boldsymbol{k}}|, \tag{2.8}$$

where the plus sign corresponds to the electron band and the minus sign to the hole band. Importantly, given that $\gamma_{\boldsymbol{k}} = 0$ only at $\boldsymbol{k} = \mathbf{K}$ or $\boldsymbol{k} = \mathbf{K}'$, the zero energy surface $\varepsilon_{\boldsymbol{k},\pm} = 0$ cuts the band structure only at the K and K$'$ points. In particular, in the vicinity of the Dirac points, $\boldsymbol{k} = \mathbf{K} + \delta\boldsymbol{k}$ and $\boldsymbol{k} = \mathbf{K}' + \delta\boldsymbol{k}$, the spectrum is linear with wavevector,

$$\varepsilon_{\mathbf{K}+\delta\boldsymbol{k},\pm} = \varepsilon_{\mathbf{K}'+\delta\boldsymbol{k},\pm} \approx \pm\hbar v_{\mathrm{F}}|\delta\boldsymbol{k}|, \tag{2.9}$$

where $v_{\mathrm{F}} = 3ta_0/2\hbar \approx 10^6\,\mathrm{m/s}$ is the Fermi velocity. The linear spectrum yields a linear density of states close to the Dirac points,

$$D(\varepsilon) = \frac{N_{\mathrm{s}}N_{\mathrm{v}}|\varepsilon|}{2\pi(\hbar v_{\mathrm{F}})^2}, \tag{2.10}$$

where $N_{\mathrm{s}} = 2$ and $N_{\mathrm{v}} = 2$ is the spin and valley degeneracy, respectively. Interestingly, the linear density of states in Eq.(2.10) is different from the $1/\sqrt{\varepsilon}$ dependence observed in nanotubes and the constant density of states in conventional 2D metals.

Another significant feature of the graphene band structure is that, since the energy band is exactly symmetric about the point $\varepsilon_{\boldsymbol{k},\pm} = 0$, the Fermi level at half-filling lies exactly at the Dirac point. The half-filling condition is exactly satisfied in the case of undoped graphene. This occurs because there is one electron per p_z orbital combined with the $N_{\mathrm{s}} = 2$ spin degeneracy. As such, the hole band in undoped graphene is

completely filled and graphene is a semimetal.

Because of the semimetallic nature of graphene, it is necessary to find an effective (long-wavelength) Hamiltonian which is valid close to the Dirac points. The procedure for deriving such an effective theory consists on expanding $\gamma_{\boldsymbol{k}}$ at the K-point, which yields $\gamma_{\mathbf{K}+\boldsymbol{k}} \approx 3at(k_x - ik_y)/2 + \mathcal{O}(\boldsymbol{k}^2)$. Using this expansion of $\gamma_{\boldsymbol{k}}$ on Eq.(2.7), and redefining $\hat{c}_{\mathbf{K}+\boldsymbol{k},\alpha}$ for small $\boldsymbol{k}$ values as $\hat{\psi}_{\boldsymbol{k}}$, the effective Hamiltonian

$$\hat{\mathcal{H}} = \sum_{\boldsymbol{k}} \hbar v_{\mathrm{F}} \hat{\psi}^{\dagger}_{\boldsymbol{k}} (\boldsymbol{\sigma} \cdot \boldsymbol{k}) \hat{\psi}_{\boldsymbol{k}}, \tag{2.11}$$

is obtained. Similarly, in the vicinity of K$'$ the expansion of $\gamma_{\boldsymbol{k}}$ yields $\gamma_{\mathbf{K}'+\boldsymbol{k}} = -k_x - ik_y$, resulting in the effective Hamiltonian

$$\hat{\mathcal{H}} = \sum_{\boldsymbol{k}} \hbar v_{\mathrm{F}} \hat{\psi}'^{\dagger}_{\boldsymbol{k}} (\bar{\boldsymbol{\sigma}} \cdot \boldsymbol{k}) \hat{\psi}'_{\boldsymbol{k}}, \tag{2.12}$$

where $\bar{\boldsymbol{\sigma}} = (-\sigma_x, \sigma_y)$ and $\hat{\psi}'_{\boldsymbol{k}}$ denotes the annihilation operator in the vicinity of the K$'$-point. The presence of two valleys allows us to define a valley degree of freedom, or valley pseudospin; this makes the graphene wavefunction a four component spinor described by the Hamiltonian

$$\hat{\mathcal{H}} = \sum_{\boldsymbol{k}} \hbar v_{\mathrm{F}} \hat{\Psi}^{\dagger}_{\boldsymbol{k}} \begin{pmatrix} \boldsymbol{\sigma} \cdot \boldsymbol{k} & 0 \\ 0 & \bar{\boldsymbol{\sigma}} \cdot \boldsymbol{k} \end{pmatrix} \hat{\Psi}_{\boldsymbol{k}}, \quad \hat{\Psi}_{\boldsymbol{k}} = \begin{pmatrix} \hat{\psi}_{\boldsymbol{k}} \\ \hat{\psi}'_{\boldsymbol{k}} \end{pmatrix}. \tag{2.13}$$

The eigenstate solutions of (2.11) and (2.12) are

$$|\psi_{\boldsymbol{k},\pm}\rangle = \frac{1}{\sqrt{2}} \begin{pmatrix} e^{-i\phi_{\boldsymbol{k}}/2} \\ \pm e^{i\phi_{\boldsymbol{k}}/2} \end{pmatrix}, \quad |\psi'_{\boldsymbol{k},\pm}\rangle = \frac{1}{\sqrt{2}} \begin{pmatrix} e^{i\phi_{\boldsymbol{k}}/2} \\ \pm e^{-i\phi_{\boldsymbol{k}}/2} \end{pmatrix}, \tag{2.14}$$

with eigenvalues $\varepsilon_{\boldsymbol{k},\pm} = \pm \hbar v_{\mathrm{F}} |\boldsymbol{k}|$. The $\pm$ signs correspond to the electron (+) and hole (-) bands, and $\phi_{\boldsymbol{k}}$ is the polar angle of $\boldsymbol{k}$, i.e. $\phi_{\boldsymbol{k}} = \mathrm{atan}(k_x/k_y)$.

A salient feature of the wavefunctions is that, if $\phi_{\boldsymbol{k}}$ is shifted by 2π, then the wavefunction changes sign. This change of sign under rotations is characteristic of spinors: the wavefunction in each valley is a two-component spinor, just as the electron spin.

In particular, the pseudospin $|\psi_{\boldsymbol{k},\pm}\rangle$ represents a spin locked in the x-y plane with direction $\boldsymbol{k}$, or opposite to it (see Sec.2.3).

The real space representation of the Dirac equation is obtained by identifing $\hbar\boldsymbol{k}$ in Eqs.(2.11)-(2.12) with the momentum operator, $\boldsymbol{p} = -i\hbar\nabla_{\boldsymbol{r}}$. This results in the eigenvalue equations

$$v_{\rm F}(\boldsymbol{\sigma}\cdot\boldsymbol{p})\psi_{\boldsymbol{r}}, = \varepsilon\psi_{\boldsymbol{r}}, \quad v_{\rm F}(\bar{\boldsymbol{\sigma}}\cdot\boldsymbol{p})\psi'_{\boldsymbol{r}} = \varepsilon\psi'_{\boldsymbol{r}}. \tag{2.15}$$

2.2.1 Static electromagnetic fields

The effective Hamiltonian describing graphene electrons in electromagnetic fields is obtained by a combination of Peierls substitution $\boldsymbol{p} \to \boldsymbol{p} - e\boldsymbol{A}/c$, with $\boldsymbol{A}$ the vector potential, and inclusion of a scalar potential $U(\boldsymbol{r})$:

$$\mathcal{H} = v_{\rm F}\,\boldsymbol{\sigma}\cdot(\boldsymbol{p} - e\boldsymbol{A}/c) + U(\boldsymbol{r}). \tag{2.16}$$

The scalar term $U(\boldsymbol{r})$ describes an external electrostatic potential which acts on-site in the tight-binding description. For Eq.(2.16) to be valid, $U(\boldsymbol{r})$ needs to vary on a scale much larger than the lattice constant a_0. If this condition fails, then intervalley scattering may occur and a coupling between ψ and ψ' arises.

Electrostatic potentials play an important role in the physics of graphene insofar as they allow local control of the Fermi energy (or Fermi wavelength) in graphene. Essential for this work, electrostatic potentials also allow researchers to create interfaces between regions with opposite polarity, i.e. *pn* interfaces. Such *pn* interfaces have peculiar scattering properties induced by the chiral nature of graphene carriers, as will be discussed in more detail in Sec.2.3. The electrostatic potential is characterized by the lengthscale

$$\ell_U = \sqrt{\frac{\hbar v_{\rm F}}{|\nabla_{\boldsymbol{r}}U|}}. \tag{2.17}$$

The value of ℓ_U at the *pn* junction quantifies its sharpness. Typical values achievable in laboratory for ℓ_U can go as low as several tens of nm. Two chapters (Chapters 7

and 8) are devoted to study the physics of confined Dirac electrons inside pn rings.

The Dirac equation (2.16) is also characterized by a second length scale, the magnetic length:

$$\ell_B = \sqrt{\frac{\hbar c}{eB}} = \frac{26\,\text{nm}}{\sqrt{B\,[\text{T}]}}, \tag{2.18}$$

where $B = |\nabla_{\boldsymbol{r}} \times \boldsymbol{A}|$. Magnetic fields induce cyclotron motion with a characteristic energy $\hbar\omega_{\text{c}} = \sqrt{2}\hbar v_{\text{F}}/\ell_{\text{B}}$. [31] The behavior of graphene electrons in the presence of strong magnetic fields, $\ell_B \ll \ell_U$, is distinct from the behavior of non-relativistic electrons. For instance, the cyclotron energy scales as $\sqrt{B}$, which is different from the linear B-dependence in the non-relativistic case. In addition, the energy scales associated with the cyclotron motion are rather different in each case: for fields $B \sim 10\,\text{T}$, the cyclotron energy for a typical 2D electron gas is on the order of $10\,\text{K}$, whereas in graphene the cyclotron energy is on the order of $1000\,\text{K}$. As a result, the quantum Hall effect can be observed in graphene even at room temperature [11]. Finally, the energy of the Landau levels in graphene are not equally spaced; instead, they follow a square root dependence $\varepsilon_{n,\pm} = \pm\hbar\omega_{\text{c}}\sqrt{n}$, with n a positive integer, and feature a zero-energy state ($n = 0$) which is responsible for the anomalies observed in the quantum Hall effect. Magnetic fields do play an important role in this work (see Chapter 8), but we will always be limited to the small field regime $\ell_U \ll \ell_B$.

2.3 Chiral nature of graphene carriers

Besides the light-like behavior, graphene charge carriers also feature a pseudospin degree of freedom which is associated to the A, B sublattice components of the graphene wavefunction. This pseudospin is locked to the direction of propagation, i.e. graphene electrons have a well-defined chirality. In this section I discuss the concept of helicity and its manifestations on the physics of graphene. These effects will play a central role in the creation of graphene quantum dots (Chapter 7) and their anomalous behavior in magnetic fields (Chapter 8).

2.3.1 Helicity

Electrons in graphene are described by the same equations as an ultra-relativistic (or massless) particle. By analogy to QED, one can then introduce a relevant operator, the helicity $\hat{\eta}$, that characterizes the Dirac eigenfunctions. In particular, $\hat{\eta}$ is defined as the projection of the momentum operator along the *pseudospin* direction:

$$\hat{\eta} = \frac{1}{2}\frac{\boldsymbol{\sigma} \cdot \boldsymbol{p}}{|\boldsymbol{p}|}. \tag{2.19}$$

This definition differs from the one in QED in which $\hat{\eta}$ acts on the real spin of the electron. The eigenvalues of $\hat{\eta}$ are

$$\hat{\eta}\,|\psi_{\boldsymbol{k},\pm}\rangle = \pm\frac{1}{2}|\psi_{\boldsymbol{k},\pm}\rangle, \tag{2.20}$$

and similarly for K′ but with an inversed sign. This imples that the pseudospin $\boldsymbol{\sigma}$ has its two eigenvalues in the direction (or against) the momentum.[1] Crucially, the concepts of helicity and pseudospin are important because many electronic processes in graphene, e.g. Klein tunneling and the absence of backscattering, result from the conservation of these quantities.

2.3.2 Absence of backscattering and Klein tunneling

Both the absence of backscattering and Klein tunneling arise from the sublattice pseudspin $\boldsymbol{\sigma}$ being aligned with the wavevector $\boldsymbol{k}$. Such alignment results in pseudospin phase cancellations of the form $\langle\psi_{-\boldsymbol{k},\pm}|\psi_{\boldsymbol{k},\pm}\rangle = 0$. For instance, in the case of long-ranged disorder, the scattering potential has the same strength in both sublattices. As a result, the scattering matrix element $\langle\psi_{-\boldsymbol{k},\pm}|U|\psi_{\boldsymbol{k},\pm}\rangle = 0$ vanishes and electrons cannot be backscattered. This effect arising from the chiral nature of graphene electrons was first studied in the context of carbon nanotubes [34, 35].

Similar arguments lead to Klein tunneling, the unit transmission of massless Dirac

[1] It is important to keep in mind that the helicity values in Eq.(2.20) are good quantum numbers so long as the Dirac Hamiltonian is valid, i.e. at small enough energies.

electrons at normal incidence. A simple semiclassical way to understand Klein tunneling in the context of graphene is as follows: because the Fermi velocity v_{F} in graphene is energy-independent, an electron moving along the field lines cannot be backscattered as that would imply that $v_{\mathrm{F}} = 0$ at the classical return point. Such behavior, which implies that electron trajectories are deflected for $p_y \neq 0$ but are perfectly transmitted for $p_y = 0$, is schematically shown in Fig.2-2(a) for the electrostatic potential $U(x) = eEx$. The reason why an electron is able to propagate through an arbitrarily large potential barrier is because the electron can make a transition from the conduction band to the valence band. In this transition, the electron is able to continue moving in the same direction along the field lines even when its *momentum* goes through zero and changes sign.

Quantum-mechanically, not only can electrons avoid backscattering at $p_y = 0$ but also at small but finite p_y; in this case, interband tunneling occurs. In particular, the transmission probability $\mathrm{T_K}(p_y)$ has an exponential dependence on p_y^2:

$$\mathrm{T_K}(p_y) = \exp(-\pi v_{\mathrm{F}} p_y^2/\hbar E), \tag{2.21}$$

which is valid if $|p_x| \gg |p_y|, \sqrt{\hbar E/v_{\mathrm{F}}}$ [36]. Transmission is also unity at normal incidence in a *pnp* junction [37], in marked contrast with conventional resonant tunneling through a double-barrier junction.

Interestingly, Klein tunneling is a direct consequence of the so-called Klein paradox [38], which was predicted in 1929 by Oskar Klein in the context of high-energy physics. The Klein paradox presented a quantum mechanical objection to the notion of electronic confinement inside a nucleus. Specifically, Klein showed that if the potential barrier V is much larger than the electron mass energy, m_0c^2, then the potential barrier is transparent.

Klein tunneling plays an imporant role in several situations. One example is Veselago lensing [39], which enables the focusing of transmitted hole states emerging from an electron source [Fig.2-2(b)]. This behavior is analogous to photons moving in a medium with a negative refractive index. A second example is electron transport

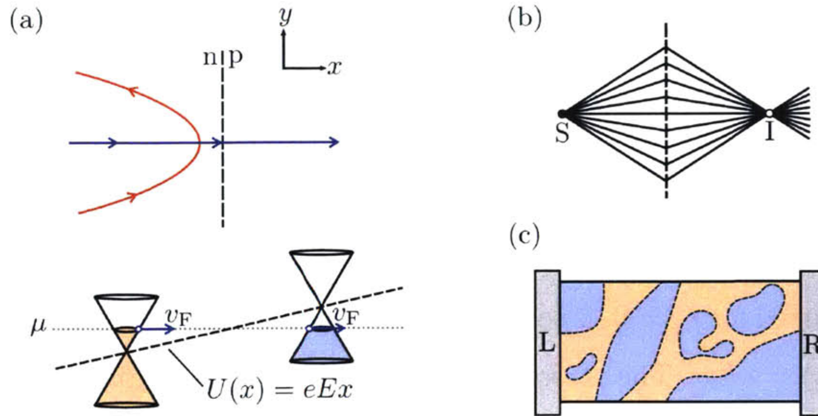

Figure 2-2: Klein tunneling of Dirac electrons. (a) Semiclassical trajectories of a massless Dirac electron in the presence of a uniform electric field, displaying distinct behavior between normal and oblique incidence. Oblique trajectories (red) are backscattered at the *pn* juntion; because the velocity for massless particless is constant, normal trajectories cannot be backscattered and are thus perfectly transmitted. (b) The *pn* interface mimicks materials with negative refractive index. This has motivated the idea of focusing electronic waves [39]. (c) At charge neutrality, transport is dominated by the transmission of Dirac electrons across electron-hole puddles. As such, transport is governed by Klein scattering.

in disordered graphene at half-filling. Because of disorder, graphene can be divided in puddles with n and p doping. [Fig.2-2(c)]. As such, transport is mainly governed by the transmission across the pn junctions between these puddles [40, 41]. A final example, which will be important in this work, are graphene quantum dots, where the inner and outer regions contain electrons and holes, respectively. Interestingly, the fact that electrostatic barriers do not impede the transmission of normally incident electrons does not preclude the existence of sharp resonances due to confinement of graphene electrons. This leads to the possibility of fabricating quantum dots with electrostatic potential barriers, as will be discussed in Chapter 7 and 8.

2.3.3 Berry phase and semiclassical quantization

The sublattice pseudospin is also manifested via the Berry phase. Berry phase effects have permeated through all branches of physics [42]; in solid-state physics, they lead to profound effects such as orbital magnetism and various Hall effects [33]. As we will see, the Berry phase in graphene will have dramatic manifestations in the energy spectrum of confined electronic states. In particular, these effects leat to exotic manifestations

which are not available for confined electrons in conventional electronic systems.

In essence, the Berry phase can be understood as the quantum phase acquired by a specific state as it evolves *adiabatically* via a time-dependent Hamiltonian $\mathcal{H}[\boldsymbol{h}(t)]$. Here $\boldsymbol{h}(t)$ are N time-dependent parameters $\boldsymbol{h}(t) = [h_1(t), \ldots, h_N(t)]$, and the n-th eigenstate and eigenvalue of $\mathcal{H}$ are denoted as $|\boldsymbol{h}(t), n\rangle$ and $\varepsilon_n[\boldsymbol{h}(t)]$, respectively. If the Hamiltonian returns to the same initial point at time T, the time-dependent eigenstate $|\boldsymbol{h}(t), n\rangle$ acquires, in addition to the usual phase $\int_0^T dt \varepsilon_n[\boldsymbol{h}(t)]$, the extra (Berry) phase

$$\varphi_{\mathrm{B}} = \oint_{\mathcal{C}} d\boldsymbol{h} \cdot \tilde{\boldsymbol{A}}_{\boldsymbol{h}}, \quad \tilde{\boldsymbol{A}}_{\boldsymbol{h}} = i\langle \boldsymbol{h}, n|\nabla_{\boldsymbol{h}}|\boldsymbol{h}, n\rangle. \tag{2.22}$$

Here $\mathcal{C}$ denotes a closed path in parameter space along which $\boldsymbol{h}$ evolves and $\tilde{\boldsymbol{A}}_{\boldsymbol{h}}$, the Berry connection, resembles a vector potential in parameter space.[2] For Eq.(2.22) to be meaningful, it is necessary to pick a gauge such that $|\boldsymbol{h}(t), n\rangle$ is a smooth function of $\boldsymbol{h}$ along the path $\mathcal{C}$.[3]

The Berry phase φ_{B} has three key properties. First, the Berry phase is geometrical. This means that φ_{B} depends only on the path $\mathcal{C}$, but is independent of the rate of change of $\boldsymbol{h}(t)$. Second, the Berry phase is gauge invariant. As such, a gauge transformation $|\boldsymbol{h}, n\rangle \rightarrow e^{ig(\boldsymbol{h})}|\boldsymbol{h}, n\rangle$, with $g(\boldsymbol{h})$ a smooth function of $\boldsymbol{h}$, does not modify the value of φ_{B}. Third, the Berry phase features close connections to gauge field theories thus providing Berry-phase-related phenomena with a rich mathematical structure.

In solid-state physics, there are several ways to create 'closed' paths in momentum space. One simple way is to apply a magnetic field. In this case, the induced cyclotron motion results in closed orbits both in real and momentum space. Similarly, closed orbits can also be created using electrostatic potentials, as will be studied in great detail in Chapters 7 and 8.

[2]For Eq.(2.22) to be valid, two important conditions must be met. First, the time scale in which $\boldsymbol{h}(t)$ varies must be large compared to $\hbar/\delta\varepsilon$, with $\delta\varepsilon$ the typical eigenvalue separation of $\mathcal{H}$ (i.e. the adiabatic condition). In this case, as the system evolves, there is no mixing between the $|\boldsymbol{h}, n\rangle$ state and other $|\boldsymbol{h}, m\rangle$ states. Second, the state $|\boldsymbol{h}, n\rangle$ has to be non-degenerate throughout the evolution of $\boldsymbol{h}$; otherwise, a more general non-abelian formulation is required [43].

[3]In general, finding a smooth gauge along $\mathcal{C}$ is possible; therefore, this condition does not pose any limitation to the concept of Berry phase.

In the context of confined electronic states, the Berry phase enters naturally as a shift to the classical action, affecting the energies of the quantized levels. Indeed, for integrable semiclassical dynamics, such as Bloch oscillations and cyclotron orbits, one can use the Bohr-Sommerfeld quantization rule,

$$\oint_{\mathcal{C}} d\boldsymbol{r} \cdot \boldsymbol{k} + \varphi_{\mathrm{B}} = 2\pi(n+\nu), \tag{2.23}$$

which includes the Berry phase contribution φ_{B}. Here $\mathcal{C}$ is the semiclassical trajectories and ν is a constant which depends on the potential slope at the classical return point. Equation (2.23) is crucial to find energy levels of confined electronic systems, such as those studied in Chapters 7 and 8.[4]

For two-band systems as in graphene, $\tilde{\boldsymbol{A}}_{\boldsymbol{h}}$ resembles the vector potential of a magnetic monopole centered at the Dirac point. Furthermore, because of the chiral nature of graphene electrons, the Berry phase in graphene can only take multiple values of π. Indeed, a general two-band Hamiltonian can be described in terms of four parameters:

$$\mathcal{H}(\boldsymbol{h}) = \boldsymbol{\sigma} \cdot \boldsymbol{h} + h_0, \quad \mathcal{H}|\boldsymbol{h}_{\pm}\rangle = (\pm|\boldsymbol{h}| + h_0)|\boldsymbol{h}_{\pm}\rangle, \tag{2.24}$$

where, in general, $\boldsymbol{h} = (h_x, h_y, h_z)$ and h_0 can be functions of position, momentum and time. Note that the scalar term h_0 only affects the Hamiltonian eigenvalues but not the eigenstates $|\boldsymbol{h}_{\pm}\rangle$. As such, h_0 does not play any role in the Berry phase. In particular, the eigenstates of Eq.(2.24) are

$$|\boldsymbol{h}_+\rangle = \begin{pmatrix} e^{-i\phi_{\boldsymbol{h}}/2}\cos(\theta_{\boldsymbol{h}}/2) \\ e^{i\phi_{\boldsymbol{h}}/2}\sin(\theta_{\boldsymbol{h}}/2) \end{pmatrix}, \quad |\boldsymbol{h}_-\rangle = \begin{pmatrix} e^{-i\phi_{\boldsymbol{h}}/2}\sin(\theta_{\boldsymbol{h}}/2) \\ e^{i\phi_{\boldsymbol{h}}/2}\cos(\theta_{\boldsymbol{h}}/2) \end{pmatrix}, \tag{2.25}$$

where $\theta_{\boldsymbol{h}}$ is the polar angle and $\phi_{\boldsymbol{h}}$ the azimuthal angle of the vector $\boldsymbol{h}$. It can be shown that the Berry connection $\tilde{\boldsymbol{A}}_{\boldsymbol{h}} = i\langle \boldsymbol{h}_+|\nabla_{\boldsymbol{h}}|\boldsymbol{h}_+\rangle$ corresponds to a magnetic

[4] In Chapter 8, a small variation of Eq.(2.23) is used in which $\mathcal{C}$ are curves defined on an invariant tori. This method, called EBK quantization, is geometric in nature (i.e., it is coordinate independent) and is applicable even in chaotic systems.

monopole at the Dirac point in $\boldsymbol{h}$-space: $\tilde{\boldsymbol{B}} = \nabla_{\boldsymbol{h}} \times \tilde{\boldsymbol{A}}_{\boldsymbol{h}} = \boldsymbol{h}/2|\boldsymbol{h}|^3$. As a result, φ_{B} is proportional to the solid angle subtended by $\boldsymbol{h}$ along $\mathcal{C}$:

$$\varphi_{\mathrm{B}} = \oint_{\mathcal{C}} d\boldsymbol{h} \cdot \tilde{\boldsymbol{A}}_{\boldsymbol{h}} = \iint_{S(\mathcal{C})} d^2\boldsymbol{h} \cdot \boldsymbol{h}/2|\boldsymbol{h}|^3 = S(\mathcal{C})/2. \tag{2.26}$$

Because $\boldsymbol{h}$ is locked to the x-y plane in gapless Dirac systems as in graphene, $S(\mathcal{C})$ can only be multiples of 2π; thus φ_{B} is a multiple of π. For gapped Dirac systems, because $\boldsymbol{h}$ is no longer locked to the x-y plane, φ_{B} can vary continuously.

2.4 Graphene-light interaction

The optical response of graphene features a unique combination of characteristics which sets graphene apart from any other optoelectronic system. For instance, graphene is characterized by a universal light absorption coefficient which is proportional to the fine structure constant. Furthermore, the energy absorbed from light can be efficiently redistributed between the electronic degrees of freedom thus resulting in a long-living hot carrier distribution which governs the graphene photoresponse. These effects will be crucial to understand the photoresponse of vertically-stacked graphene nanostructures (Chapters 5 and 6). Other important effects which are not discussed in this thesis are, for instance, the giant Faraday rotation [44, 45] and the unique plasmonic response in graphene [46].

2.4.1 Universal light absorption coefficient

An important characteristic of gapless two-dimensional electronic systems is the universal light absorption coefficient. In graphene, the absorption coefficient is proportional to the fine structure constant α:

$$\lambda_{\mathrm{abs}} = \frac{P_{\mathrm{abs}}}{P_{\mathrm{in}}} = \pi \frac{e^2}{\hbar c} = \pi\alpha, \tag{2.27}$$

where P_{in} (P_{abs}) denotes incident (absorbed) power. This results from using Fermi Golden's rule, $P_{\text{abs}} = (2\pi/\hbar)|\mathcal{M}_{\text{er}}|^2 D(\hbar\omega/2)\hbar\omega$, to calculate absorbed energy by direct electron-hole transitions. Here $D(\hbar\omega/2)$ is the density of states at the optical transition energy and $\mathcal{M}_{\text{er}}$ is the electron-light matrix element. The matrix element $\mathcal{M}_{\text{er}}$ is obtained from the electron-photon coupling, which is obtained from the Peierls substitution $\boldsymbol{p} \to \boldsymbol{p} - e\boldsymbol{A}/c$:

$$\mathcal{H}_{\text{er}} = -\frac{ev_{\text{F}}}{c}\int_S d\boldsymbol{r}\,\hat{\Psi}_{\boldsymbol{r}}^\dagger \begin{pmatrix} \boldsymbol{\sigma}\cdot\boldsymbol{A} & 0 \\ 0 & \bar{\boldsymbol{\sigma}}\cdot\boldsymbol{A} \end{pmatrix} \hat{\Psi}_{\boldsymbol{r}}. \tag{2.28}$$

In general, photon-induced transitions are momentum-conserving. This occurs because the photon wavevector $|\boldsymbol{Q}| = \omega/c$ for frequencies in the visible range or below is much smaller than the unit cell length scale $1/a_0$; this results in $\mathcal{M}_{\text{er}} = -iev_{\text{F}}\langle\psi_{\boldsymbol{k},+}|\boldsymbol{\sigma}\cdot\boldsymbol{A}|\psi_{\boldsymbol{k},-}\rangle$. Equation (2.27) then follows from using $P_{\text{in}} = c\boldsymbol{E}^2/4\pi$, with $\boldsymbol{E} = -i\omega\boldsymbol{A}$.

Interestingly, λ_{abs} is independent of material properties, i.e. independent of the Fermi velocity v_{F}. In the case of a zero-gap semiconductor with a parabolic spectrum, the same analysis leads to $\lambda_{\text{abs}} = 2\pi\alpha$. In other words, the optical properties of graphene are due to the gapless 2D nature of electrons and not due to the conical band structure.

2.4.2 Electron lattice cooling and hot carriers

In addition to the special universal light absorption coefficient, graphene also features an unusual kind of intrinsic photoresponse. Such a photoresponse, which is mediated by hot carriers, originates from the quenching of electron-lattice cooling when the system is close to charge-neutrality [47, 48]. Quenching of cooling mechanisms occurs for two reasons: (i) the small phase space available for momentum transfer into acoustic phonon states and (ii) the exceptionally large optical phonon energies $\hbar\omega_0 \sim 0.2\,\text{eV}$. Given the intrinsic inability of graphene to relax energy into the lattice by electron-phonon interactions, the absorbed energy is quicky redistributed between

the electronic degrees of freedom by fast electron relaxation mediated by electron-electron interactions. As a result, an exceptionally long-lived hot carrier distribution proliferates across the entire system [49–51].

Because of the fast relaxation mediated by electron-electron interactions, graphene can be described by a two-temperature model characterizing the electron and lattice subsystems by two different temperatures, T and T_0. In pump probe experiments, typical hot carrier temperatures can be on the order of $T \sim 10^3\,\mathrm{K}$.

Although small, it is important to quantify electron-lattice cooling in order to understand the thermal imbalance in graphene. Electron cooling in graphene is dominated by three main mechanisms: acoustic and optical phonon emission [47,48], and disorder-assisted acoustic phonon emission [52]. The two acoustic phonon mechanisms are limited by the small phase space available for scattering and the small acoustic phonon energies which can be transfered per scattering event. As such, both the intrinsic and disorder-assisted cooling power, P_{ac} and P_{dis}, feature a strong dependence on Fermi energy:

$$P_{\mathrm{ac,d}} \propto \mu^a (T^b - T_0^b), \tag{2.29}$$

which is valid in the degenerate limit $\mu \gg k_{\mathrm{B}}T$. In Eq.(2.29), a and b are constants that depend on the cooling mechanism. Optical phonon cooling, on the other hand, is limited by the large phonon frequencies $\hbar\omega_0 \sim 0.2\,\mathrm{eV}$, making this cooling mechanism thermally activated. In the degenerate limit, the optical phonon cooling power P_{opt} behaves as

$$P_{\mathrm{opt}} \propto \left[e^{-\hbar\omega_0/k_{\mathrm{B}}T} - e^{-\hbar\omega_0/k_{\mathrm{B}}T_0}\right]. \tag{2.30}$$

The explicit dependence of P_{ac}, P_{d} and P_{opt} on model parameters will be discussed in Sec.5.6.

Naturally, in realistic scenarios all three mechanisms are acting simultaneously. The dominant cooling mechanism will be determined by the specific experimental condition, namely the Fermi energy and power pumped into the system. To illustrate such an interplay between the different cooling mechanisms, the dominant cooling mechanisms is plotted in Fig.2-3(a) for various pump powers and Fermi energies.

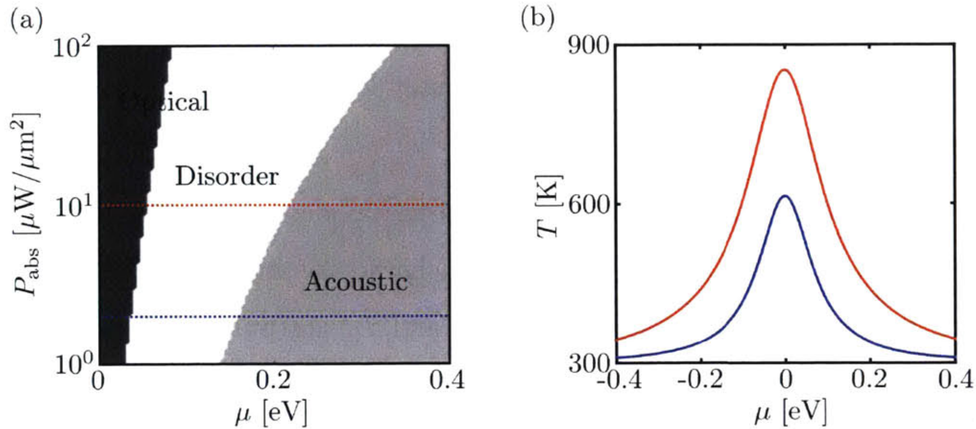

Figure 2-3: Dominant cooling mechanism in graphene. (a) Shown are the dominant cooling mechanisms as a function of cooling power and Fermi energy. The explicit dependence of each cooling mechanism on model parameters is discussed in Sec.5.6. (b) Temperature dependence of graphene as a function of Fermi energy at constant input power, including the three dominant cooling mehanisms involving optical phonons, acoustic phonons and disorder-assisted cooling mechanisms. The red curve indicates a typical $P_{\rm abs} = 10\,\mu\mathrm{W}/\mu\mathrm{m}^2$ and the blue curve indicates $P_{\rm abs} = 2\,\mu\mathrm{W}/\mu\mathrm{m}^2$

Close to the charge neutrality point ($\mu = 0$), both acoustic phonon cooling mechanisms are quenched and optical phonon cooling dominates. At lower temperature, given the thermally-activated nature of $P_{\rm opt}$, this cooling process is quenched and acoustic mechanisms dominate. Figure 2-3(b) shows the temperature for two linecuts of (a) at constant P. Because of the poor electron-phonon cooling, a spike in the electronic temperature is obtained at charge neutrality.

2.5 Electrostatic doping and quantum capacitance

The vanishingly small carrier density close to the neutrality point in graphene leads to unusual electrostatic behaviors. In particular, graphene charge carriers are unable to efficiently screen external charges thus resulting in the permeation of the electric field across the graphene layers. As such, inefficient screening leads to nonlinear charge-bias relations, distinct from the typical linear behavior observed in conventional capacitors. Such effects are relevant in the study of graphene-based nanostructures (Chapters 3-6) as well as in lateral nanostructures (Chapters 7-8).

There are three reasons why it is important to accurately model electrostatic

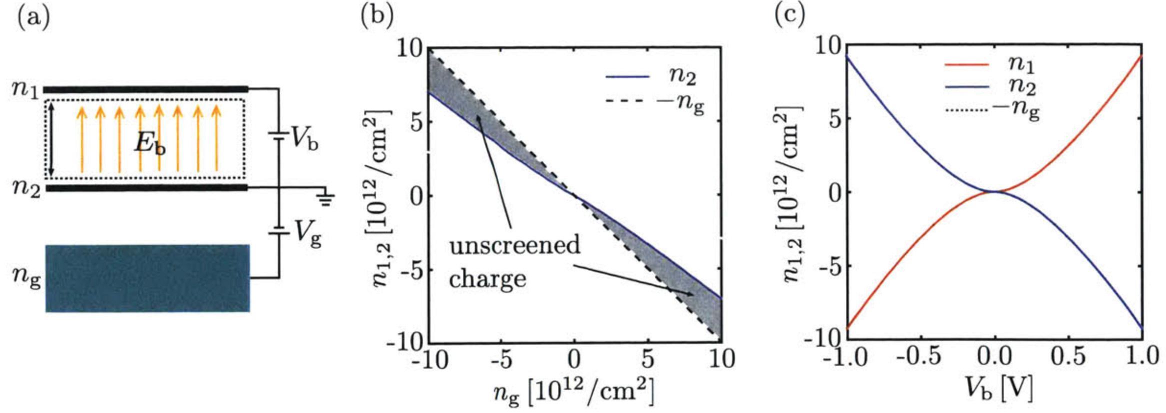

Figure 2-4: Quantum capacitance effects in graphene nanostructures. (a) Shown is a gated graphene device: a gate (V_g) and bias (V_b) potentials are used to vary the top (n_1) and bottom (n_2) carrier densities as well as the gate charge (n_g). (b) Poor screening of the gate charge by the middle graphene layer. Shown is the gate-induced carrier concentrations n_2 in graphene as a function of n_g, for $V_b = 0$, see Eqs.(2.31),(2.32) [$d = 1\,\mathrm{nm}$, $\epsilon_r = 5$]. (c) Nonlinear charge-bias relation for a graphene capacitor. ($n_g = 0$). Close to the neutrality point, carrier concentration behave as $n_{1,2} \propto V_b^2$, different from the usual $n_{1,2} \propto V_b$ dependence.

doping. First, several phenomena in graphene, such as electron-lattice cooling, are sensitive to variations in the Fermi energy. Second, in the context of graphene-to-graphene tunneling, the unscreened electric field between layers determine the energy offset between the band structures of the two layers. Third, the electrostatic field determines the potential barrier shape and, as such, modifies the tunneling coupling in graphene nanostructures.

To illustrate the non-linear screening, I consider a typical gated deviced comprised of two stacked graphene layers, as shown in Fig.2-4(a). The bias-induced carrier density $n_{1,2}$ in the graphene layers, as well as the electric field E_b between the layers, can be described by simple electrostatic considerations. First, the neutrality condition relates the charge densities in the different regions of the device:

$$n_1 + n_2 + n_g = 0, \tag{2.31}$$

where n_g is taken as a fixed charge at the gate (i.e. the gate potential V_g is adjusted so that n_g is constant). A bias voltage V_b between the graphene layers results in a

Fermi energy offset

$$eV_\mathrm{b} = \mu(n_1) - \mu(n_2) + eE_\mathrm{b}d, \tag{2.32}$$

where $E_\mathrm{b} = 4\pi e n_1/\epsilon_\mathrm{r}$ is the interlayer electric field, ϵ_r is the dielectric constant of the barrier, and $\mu(n_{1,2})$ is the Fermi energy for a carrier density $n_{1,2}$. Here I use the zero-temperature relation $\mu(n_{1,2}) = \mathrm{sign}(n_{1,2})\hbar v_\mathrm{F}\sqrt{\pi|n_{1,2}|}$, which provides a good approximate model over most of the relevant carrier density range. The two unknown variables, n_1 and n_2, can be found from equations (2.31) and (2.32), considering fixed n_g and V_b.

Inefficient screening and non-linear charge-bias relations are shown in Fig.2-4. In particular, Fig.2-4(b) displays the inability of the middle graphene layer to screen the charge of the gate [here $V_\mathrm{b} = 0$ was used]. Figure 2-4(c) illustrates the non-linear bias-charge relations for $n_\mathrm{g} = 0$. Interestingly, graphene is characterized by a quadratic relation $n_{1,2} \propto V_\mathrm{b}^2$ in the vicinity of the neutrality point, distinct from the typical $n_{1,2} \propto V_\mathrm{b}$ relation in a conventional capacitor. In both plots, I consider that both graphene layers are at charge neutrality when $n_\mathrm{g} = 0$ and $V_\mathrm{b} = 0$, and I used values $V_\mathrm{b} = 0$, $d = 1\,\mathrm{nm}$ and $\epsilon_\mathrm{r} = 5$.

Part I

Transport in vertical graphene nanostructures

Chapter 3

Interlayer transport in graphene nanostructures

Vertical heterostructures comprising layers of van der Waals materials have recently emerged as a platform for designer electronic systems [53]. Because of the remarkable progress in nanoscale fabrication which allows layer-by-layer assembly, such nanostructures feature highly tunable interlayer transport characteristics. This, combined with the unique properties of bare graphene, makes graphene-based heterostructures a fertile ground for novel physics.

Here I discuss the main features of interlayer transport between graphene layers in vertically-stacked van der Waals heterostructures. One such feature is their tunability which is manifested by numerous transport parameters which can be controlled with high precision in experiments (Sec.3.1). This grants access to several transport regimes, as will be discussed in Sec.3.2. In Sec.3.3, I discuss how different combinations of nanostructure properties can lead to new phenomena. Such phenomena will be the objective of Chapters 4-6.

3.1 Tunability of graphene heterostructures

As shown in Fig.3-1, graphene nanostructures are characterized by many tunable parameters that govern interlayer transport; all of them can be controlled during

fabrication, and some can be tuned in situ.

First, the contact between graphene and an insulating material X, such as Si, MoS_2 or WSe_2, forms a g/X Schottky junction. Because the two-dimensional electronic states in graphene are fully exposed, they are highly sensitive to the g/X interface [15,16,54–60]. As shown in Table 3.1, different Schottky junctions are characterized by Schottky barriers Φ that span two orders of magnitude $\Phi \approx 0.01$–$1\,\text{eV}$ [15,54,55,59]. Given that the chemical potential μ in graphene can be controlled in situ with gate potentials, the value of Φ can also be controlled within the same energy range $\approx 0.3\,\text{eV}$. The specific value of Φ is relevant for two important reasons: (i) Φ controls the activation energy for thermally driven thermionic emission of charge carriers; (ii) Φ controls the magnitude of the interlayer tunneling coupling.

Second, the interlayer distance d between graphene layers in Fig.3-1 can be controlled by stacking monolayers of X in-between the graphenes. The value of d plays two important roles: (i) d allows one to control the electrostatic coupling via the capacitance effect (see Sec.2.5) and (ii) d provides a fine knob to tune the tunneling coupling. Indeed, the tunneling coupling is controlled by the WKB decay length $\ell_{\text{wkb}} = \hbar/\sqrt{2m_e\Phi} \sim 2\,\text{Å}$, with m_e the effective mass in the barrier region (here I considered typical values of $\Phi \sim 1\,\text{eV}$ and $m_e \sim 10^{-30}\,\text{kg}$). The value of $\ell_{\text{wkb}} \sim 2\,\text{Å}$ is comparable with a typical monolayer thickness d_0. As such, the tunneling coupling can be smoothly varied in small steps of $\exp(-d_0/\ell_{\text{wkb}})$.

Third, the intrinsic properties of graphene can be controlled with carrier density. In particular, the electron-lattice coupling is very sensitive to Fermi energy and becomes quenched at the Dirac point. Optical pumping, for instance, enables the control of the electron temperature in each graphene layer.

Finally, interlayer transport is also sensitive to the details of the band structure of the graphenes. In particular, a twist angle θ between the graphene monolayers, which can be controlled with $\theta \sim 1°$ precision in experiments, induces a displacement between the Dirac cones corresponding to each graphene layer. The magnituce of this displacement is $|\boldsymbol{q}_\theta| = (8\pi/3a_0)\sin(\theta/2)$. Twisted bandstructures activate a resonant tunneling mechanism which dominates the I-V response, see below.

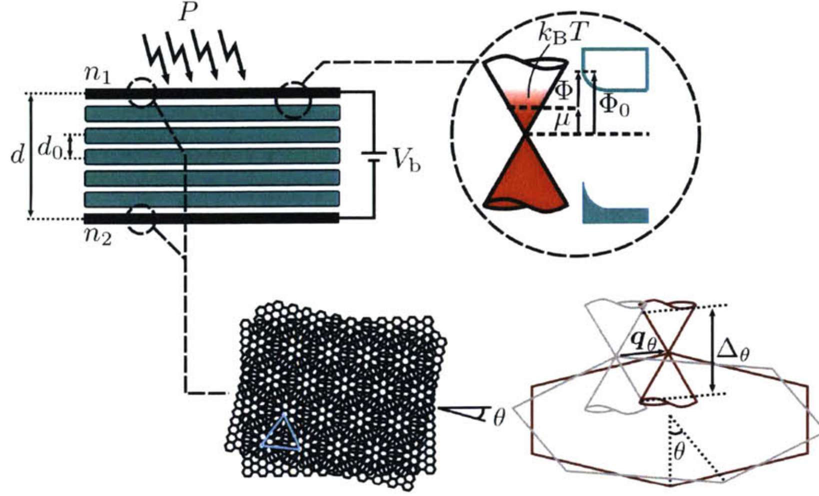

Figure 3-1: Tunable parameters in graphene-based nanostructures. (a) Shown are two graphene layers (black) separated by stacked monolayers of an insulating material X (green). The interlayer distance d between the graphenes can be tuned by adding monolayers of X with thickness d_0. Charge densities $n_{1,2}$ as well as the Fermi level μ can be adjusted by using gate and bias potentials (V_b); variations in the Fermi level modify the Schottky barrier Φ from its charge neutral value Φ_0. Given the poor electron-lattice cooling mechanism (see Sec.2.4.2), the layer temperature T can be adjusted by optical pumping P. A twist angle θ between the graphene layers result in a graphene superlattice and a twisted electronic bandstructure. In this case, the Dirac cones of layers 1 and 2 are is separated by a vector $\boldsymbol{q}_\theta$, which defines an energy scale $\Delta_\theta = \hbar v_F |\boldsymbol{q}_\theta|$.

Barrier Materials	Φ [eV]	Ref.
WS_2	0.05	[59]
MoS_2	0.15	[60]
Si	0.41	[54, 55]
hBN	1.30	[15, 16]

Table 3.1: Schottky barriers for different graphene-dielectric structures. These values should be understood as average values which can be tuned with electrostatic gating.

3.2 Vertical transport regimes

The relevant energy scales, schematically shown in Fig.3-1, that characterize the nanostructures are the Schottky potential $e\Phi$, the bias potential $eV_{\rm b}$, the electronic temperature $k_{\rm B}T$, the capacitor electrostatic energy $U_E = \epsilon_{\rm r}(\hbar v_{\rm F})^2/2e^2d$, and the band structure displacement $\Delta_\theta = \hbar v_{\rm F}|\boldsymbol{q}_\theta|$ induced by the twist angle. The operating interlayer transport regime is controlled by the ratio of the different variables. Using the Schottky barrier height Φ to non-dimensionalize all the variables, a diagram of different transport regimes with four different regions is shown in Fig.3-2.

In the regime $eV_{\rm b}/\Phi \ll 1$, $k_{\rm B}T/\Phi \ll 1$, direct tunneling between electrodes dominates transport. Depending of the details of the model, e.g. twist angle, disorder and bias potential value, transport can be momentum-conserving (resonant tunneling) or can be assisted by phonons or disorder (assisted tunneling). The transition between both regimes occurs at $eV_{\rm b} \approx \Delta_\theta$, where resonant tunneling is activated (see Chapter 4). This transition enables interesting behaviors, such as Negative Differential Resistance (NDR) and bistability in graphene nanostructures.

When $eV_{\rm b}/\Phi \ll 1$ and $k_{\rm B}T/\Phi \gtrsim 1$, thermionic currents dominate over tunneling. This is a thermally activated regime with the current governed by the activation factor $e^{-\Phi/k_{\rm B}T}$.

When $eV_{\rm b}/\Phi \gg 1$, a large electric field between the graphene layers strongly reduce the electrostatic barrier potential. As a results, the electronic current is driven by the strong electric fields and temperature effects are negligible. This is the field emission regime, as described by the Richardson's theory [61].

As discussed in Chapter 2, the factor $\epsilon_{\rm r}(\hbar v_{\rm F})^2/2e^2d$, which defines the capacitance energy U_E, mainly controls whether or not quantum capacitance [62] effects are relevant; namely, U_E affects the details of how doping varies with $V_{\rm b}$. When the capacitance energy is large, the shape of the I-V response is strongly affected but not the underlying transport mechanism.

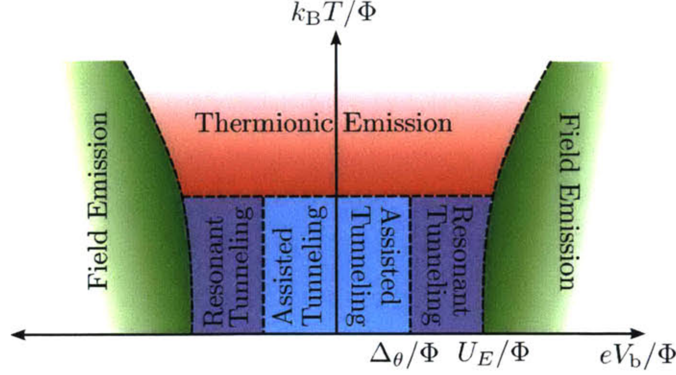

Figure 3-2: Vertical transport regimes in stacked graphene-insulator-graphene nanostructures. Shown are four different vertical transport regimes which are sensitive to tunable device parameters: the Schottky barrier Φ, the electronic temperature T, the capacitance energy U_E and the characteristic energy of the twisted superlattice Δ_θ (see Fig.3-1).

3.3 Features of vertical transport in graphene

The wide range of tunable parameters described in Sec.3.1, combined with the different transport regimes described in Sec.3.2, grants access to a wide spectrum of interesting phenomena. In the following three chapters, I will discuss several phenomena which arise due to different combinations of these characteristics. In Chapter 4, I discuss bistability arising from resonant tunneling and charge coupling in the sequential tunneling regime. In Chapter 5, I study a non-monotonic I–V behavior induced by the interplay between photogenerated hot carriers and charge coupling between graphene layers. In Chapter 6, I show that graphene Schottky junctions, because of the interplay between hot carriers and a tunable Φ, can lead to uniquely sensitive photodetectors operating in the infrared regime. Naturally, many other combinations of interesting and potentially useful behaviors are possible, making graphene nanostructures versatile designer electronic systems.

Chapter 4

Resonant tunneling and intrinsic bistability in twisted graphene nanostructures

In this chapter, I show that vertical transport in nanostructures formed by twisted graphene layers can exhibit a unique bistability mechanism.[1] Intrinsically bistable I-V characteristics arise from resonant tunneling and interlayer charge coupling, enabling multiple stable states in the sequential tunneling regime. I focus on a simple trilayer architecture, with the outer layers acting as source and drain and the middle layer floating. As we will see, the middle layer can be either resonant or non-resonant with the source and drain layers. Such nanostructures feature two notable properties. First, the bistability is controlled by geometric device parameters easily tunable in experiments. Second, the nanoscale architecture can enable uniquely fast switching times.

[1]This chapter has been reproduced from J. F. Rodriguez-Nieva, M. S. Dresselhaus, L. S. Levitov, Resonant Tunneling and Intrinsic Bistability in Twisted Graphene Structures, *Physical Review B* [in production] Copyright (2015) by the American Physical Society.

4.1 Bistability in graphene nanostructures

Nanoscale systems that can switch between distinct macroscopic states upon variation of some control parameter are of high demand in diverse areas of nanoscience research. Bistable electronic systems which exhibit fast switching are of interest for applications, such as low-power memory and logic [63]. Recently, the quest for new realizations of intrinsically bistable system has been increasing at a rapid pace, both in graphene [64–68] and in other systems [69–71]. In particular, van der Waals heterostructures comprising graphene layers sandwiched between insulating hexagonal boron-nitride (hBN) layers afford electronic environments with tailored band structures and transport characteristics [53]. It was demonstrated that introducing a twist between adjacent graphene layers in such heterostructures can result in a resonant behavior of the tunneling current and non-monotonic I-V characteristics [18]. It is therefore tempting to exploit these systems as a platform for bistable nanoscale systems.

Here I predict intrinsic bistability and hysteretic I-V characteristics for vertical transport in heterostructures formed by graphene monolayers separated by hBN barriers, in a twisted arrangement similar to that described in Ref. [18]. Essential for this bistability mechanism are resonances originating from momentum-conserving tunneling between linearly dispersing Dirac bands [72] and occurring when the bands are aligned [17] [see Fig.4-1(b,c)]. Bistability arises due to current-induced charge accumulation producing an interlayer bias that tunes the interband tunneling in and out of resonance.

Below I focus on the simplest case of a two-step sequential tunneling in a device comprising three graphene monolayers. Such trilayer architecture, pictured in Fig.4-1(a), with the top and bottom layers acting as a source and drain and the middle layer electrically decoupled (floating), is similar to previously studied double-barrier quantum-well (QW) structures [73]. However, the graphene-based bistability mechanism, originating from resonant tunneling between Dirac bands in graphene layers, is distinct from that in the QW structures [73]. In our case, multiple stable states arise

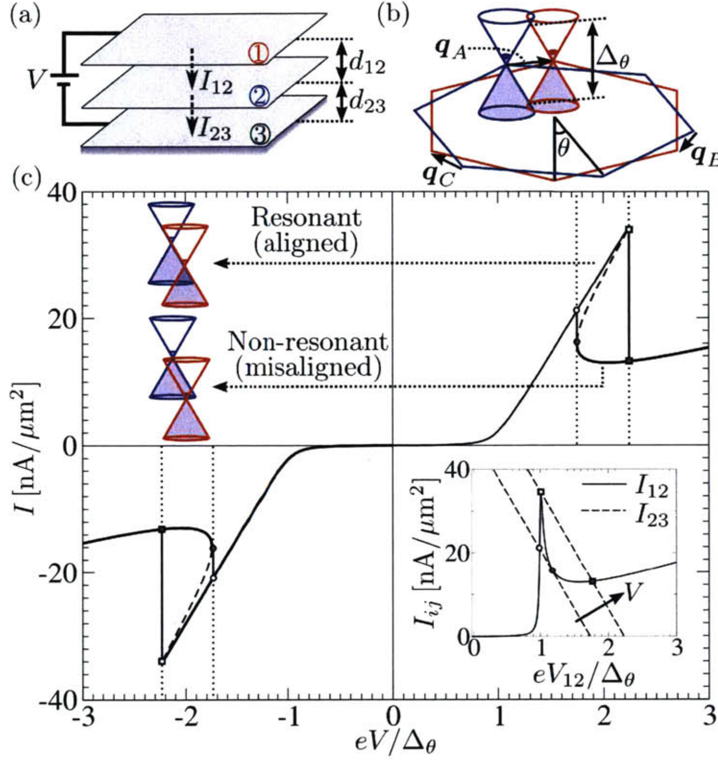

Figure 4-1: Bistable I-V response of a trilayer graphene heterostructure. (a) Trilayer graphene heterostructure schematics, with layers labelled 1 to 3. Here I_{ij} and d_{ij} are the interlayer currents and distances. (b) Band structure of the twisted graphenes 1 (blue) and 2 (red). The twist angle θ defines a characteristic energy Δ_θ [Eq.(4.1)] and three superlattice wavectors $\boldsymbol{q}_{A,B,C}$ [Eq.(4.15)]. (c) Bistable I-V characteristics. The resonant and non-resonant bistable states are illustrated in the upper-left inset (details are discussed in Fig.4-3). The procedure for finding bistable solutions is illustrated in the lower-right inset [see Eq.(4.9) and accompanying discussion].

because the decoupled layer can, for a fixed external bias, be either in a resonant (low resistance) or a non-resonant (high resistance) state. This behavior is illustrated in Fig.4-1(c).

The bistability is governed by geometric parameters – the twist angle θ and the interlayer distances d_{ij} – which are easily tunable in experiments. The twist angle controls the Dirac cones' displacement in the two layers and the energy at which the cones intersect [see Fig.4-1(b)],

$$|\boldsymbol{q}_A| = (8\pi/3a_0)\sin(\theta/2), \quad \Delta_\theta = \hbar v_{\mathrm{F}}|\boldsymbol{q}_A|, \tag{4.1}$$

where $v_{\mathrm{F}} \approx 10^6\,\mathrm{m/s}$ is the carrier velocity and $a_0 \approx 2.46\,\text{Å}$ is the graphene lattice constant. The distances d_{ij}, marked in Fig.4-1(a), determine the interlayer tunnel conductance values $G_{ij} \sim e^{2d_{ij}/\ell_{\mathrm{wkb}}}$, where ℓ_{wkb} is the WKB length governing the tunneling amplitude dependence on barrier width. In what follows, I will use the conductance ratio

$$Z = G_{12}/G_{23} \sim e^{2(d_{23}-d_{12})/\ell_{\mathrm{wkb}}} \tag{4.2}$$

where G_{ij} denotes the conductance between the corresponding ij layers.

The quantities θ and d_{ij} ocurring in Eqs.(4.1) and (4.2) can be controlled with a large degree of precision. The twist angle θ can be tuned within $\sim 1^\circ$ during fabrication [18], whereas d_{ij} can be varied by adding monolayers of dielectric materials, such as hBN or undoped MoS_2. Since typical values $\ell_{\mathrm{wkb}} = \hbar/(2m_e\Phi)^{1/2} \sim 2\,\text{Å}$, estimated for the tunneling barrier height $\Phi \sim 1\,\mathrm{eV}$ and the effective electron mass $m_e^* \sim 10^{-30}\,\mathrm{kg}$, are comparable to the hBN or MoS_2 monolayer thickness, variation in d_{ij} results in a fairly gradual change in the conductance ratio Z.

One appealing aspect of this system is the short interlayer transport length of a nanometer scale, which can allow high operation speeds and fast switching times. This is evident from an estimate for the RC time, $\tau_{RC} = \epsilon_{\mathrm{r}}/4\pi g d \sim 100\,\mathrm{ns}$, where $\epsilon_{\mathrm{r}} \sim 1$ is the dielectric constant, $d \sim 1\,\mathrm{nm}$ is the interlayer separation, and $g \sim 10^{-7}\,\Omega^{-1}\mu\mathrm{m}^{-2}$ is the interlayer conductance per unit area. The combinations of geometric tunability and small transport lengths are not present in previously studied graphene-based

bistable systems, such as graphene flash memories [64, 65] or graphene resistive memories [66–68]. Small thicknesses can also enable large packing densities.

The steep electronic dispersion in graphene makes the bistable state properties distinct from those in QW systems. In our case, the bistability is controlled by the resonances arising due to band alignment. The corresponding bias value, which scales as a power law of the energy Δ_θ given in Eq.(4.1), can be as large as $\delta V \sim$ 100-500 mV (see discussion in Sec.4.5). In QW systems, instead, the bias range where bistability occurs is mainly controlled by the amount of charge $n_{\rm QW}$ that can be stored in a quantum well, $\delta V \approx e n_{\rm QW}/C$, where C is the interlayer capacitance. Typical carrier densities in the 'charged' and 'uncharged' states of a bistable QW system, which is assessed by magnetic oscillation measurements [74], are on the order $n_{\rm QW} \sim 10^{11}/{\rm cm}^2$ and $n_{\rm QW} \sim 0$, respectively. These carrier densities yield typical values $\delta V \sim 50\,{\rm mV}$ in double-barrier quantum wells with a width of tens of nanometers ($C \sim$ 0.1-1 mF). Such values of carrier densities can be as much as an order of magnitude smaller than the above estimate predicts for the graphene case.

4.2 Sequential tunneling model

Vertical transport in our trilayer architecture can be described by a simple sequential model. The model validity relies on the interlayer tunnel coupling being weak such that the inter-layer charge transfer is slow compared to the intra-layer electron relaxation times. Indeed, the values τ_{RC}, estimated above, are much longer than typical thermalization times in graphene, $\tau_{\rm th} \sim 10\,{\rm ps}$ [75]. The RC times, however, are sufficiently fast to be competitive with the speeds of existing switching devices [63].

The interlayer transport mechanism is mainly governed by the twist angle θ, which defines the K-point displacement $\boldsymbol{q}_A$ between graphene lattices in adjacent layers, and the interlayer bias. Under bias, the value $|\boldsymbol{q}_A|$ given in Eq.(4.1) determines the range of momenta and energies for which momentum-conserving tunneling is allowed. Large values of $|\boldsymbol{q}_A|$ hinders resonant tunneling given that phonon and defect scattering are necessary to supply the large momentum mismatch between layers. Momentum-

nonconserving transport can also occur if the top/bottom layers are made of a different material so that there is a large mismatch between the unit cells of either of these layers with respect to that of graphenes. For small $|\boldsymbol{q}_A|$, on the other hand, momentum conserving tunneling is possible for moderately small values of bias.

In the two-step sequential tunneling model, I treat the transport between layers 1 and 2 as momentum-conserving. The second step, between layers 2 and 3, is assumed to be momentum-nonconserving and is described by Ohm's law. The latter assumption allows us to simplify our discussion and focus on the essential aspects of bistability. In addition, I also assume that the contact resistances are sufficiently small so that all the potential voltage drop occurs predominantly between the graphene layers.

Turning to a systematic development of the model, the low energy Hamiltonian $\hat{\mathcal{H}}$ describing coherent transport between a pair of twisted graphene monolayers has contributions $\hat{\mathcal{H}} = \hat{\mathcal{H}}_1 + \hat{\mathcal{H}}_2 + \hat{\mathcal{T}}_{12}$. Here $\hat{\mathcal{H}}_{1,2}$ are the free-particle terms describing massless Dirac particles in each graphene layer, and $\hat{\mathcal{T}}_{12}$ describes the interlayer due to tunneling [76–78]. The free particle terms are

$$\begin{aligned} \hat{\mathcal{H}}_1 &= \sum_{\boldsymbol{k}} \hat{\psi}^{\dagger}_{1,\boldsymbol{k}} [\hbar v_{\mathrm{F}} \boldsymbol{\sigma} \cdot (\boldsymbol{k} + \boldsymbol{q}_A/2) - \mu_1] \hat{\psi}_{1,\boldsymbol{k}} \\ \hat{\mathcal{H}}_2 &= \sum_{\boldsymbol{k}} \hat{\psi}^{\dagger}_{2,\boldsymbol{k}} [\hbar v_{\mathrm{F}} \boldsymbol{\sigma} \cdot (\boldsymbol{k} - \boldsymbol{q}_A/2) - \mu_2] \hat{\psi}_{2,\boldsymbol{k}} \end{aligned} \tag{4.3}$$

where $\mu_{1,2}$ are the Fermi energies measured relative to the Dirac point. For a small twist angle θ, the large-wavenumber processes that couple different valleys to each other can be neglected. In this case, it is sufficient to account for just one of the two valleys (K or K′) in each layer, as given below in Eq.(4.3). I adopt this approximation as discussed next.

The tunneling coupling can be modeled as a local, periodic function of position [76]:

$$\hat{\mathcal{T}}_{12} = \sum_{\boldsymbol{k},\tilde{\boldsymbol{b}}} \hat{\psi}^{\dagger}_{1,\boldsymbol{k}} \boldsymbol{T}_{\boldsymbol{G}} \hat{\psi}_{2,\boldsymbol{k}+\tilde{\boldsymbol{b}}} + \text{h.c..} \tag{4.4}$$

The periodicity of the interlayer coupling, quantified by the $\tilde{\boldsymbol{b}}$ wavevectors, is determined by the hexagonal superlattice unit cell that is formed by the twisted graphene

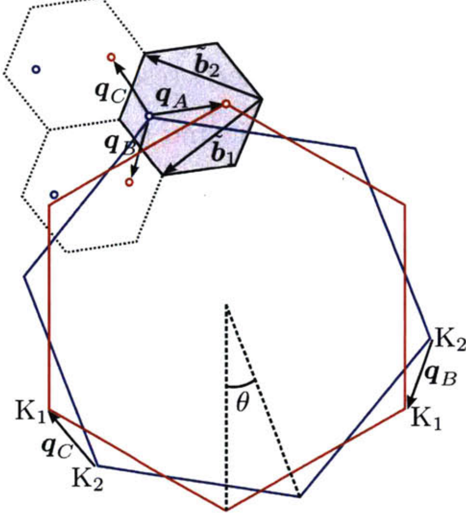

Figure 4-2: Hexagonal superlattice of twisted graphene layers. Twisted graphene layers form a hexagonal superlattice with reciprocal superlattice vectors $\tilde{\boldsymbol{b}}_1$ and $\tilde{\boldsymbol{b}}_2$ [76]. The momentum conserving tunneling coupling the two layers has the periodicity of the superlattice and can be decomposed into Fourier components $\tilde{\boldsymbol{b}} = n\tilde{\boldsymbol{b}}_1 + m\tilde{\boldsymbol{b}}_2$, with n, m integers. For a small twist angle θ, tunneling is dominated by the smallest wavevectors $\boldsymbol{q}_A$, $\boldsymbol{q}_B = \boldsymbol{q}_A - \tilde{\boldsymbol{b}}_1$ and $\boldsymbol{q}_C = \boldsymbol{q}_A - \tilde{\boldsymbol{b}}_2$, see Eq.(4.3).

layers as shown in Fig.4-2. For small θ, only the longest wavelength contributions are relevant for tunneling. Referred from the Dirac point of layer 1, such long wavelength components are given by wavevectors $\boldsymbol{q}_A$, $\boldsymbol{q}_B = \boldsymbol{q}_A - \tilde{\boldsymbol{b}}_1$ and $\boldsymbol{q}_C = \boldsymbol{q}_A - \tilde{\boldsymbol{b}}_2$ (see Fig.4-2), where $\tilde{\boldsymbol{b}}_{1,2}$ are the reciprocal vectors of the superlattice Brillouin zone [smaller than the graphene Brillouin zone by a factor $\sim \sin^2(\theta)$]. Although shorter wavelength Fourier components of the interlayer hopping potential also contribute to tunneling, it can be shown that the hopping potential-related terms fall to zero very rapidly on the reciprocal lattice vector inverse length scale [76, 77]. As such, the tunneling Hamiltonian takes the simple form

$$\hat{\mathcal{T}}_{12} = \sum_{j=A,B,C} \sum_{\boldsymbol{k}} \hat{\psi}^{\dagger}_{1,\boldsymbol{k}} \boldsymbol{T}_j \, \hat{\psi}_{2,\boldsymbol{k}+\boldsymbol{q}_j} + \text{h.c.} \tag{4.5}$$

and $\hat{\mathcal{T}}_{12}$ cantains only three Fourier components. In this expression for $\hat{\mathcal{T}}_{12}$, the $\boldsymbol{k}$ vectors are measured relative to the Dirac point of each layer, i.e. $\boldsymbol{k} - \boldsymbol{q}_A/2 \to \boldsymbol{k}$ in layer 1 and $\boldsymbol{k} + \boldsymbol{q}_A/2 \to \boldsymbol{k}$ in layer 2.

As a side remark, the lattice of the dielectric material separating the graphene

layers can produce slowly varying spatial modulation of the tunneling transition amplitude $\boldsymbol{T}$ in Eq.(4.3), giving rise to the effects resembling those due to a twist angle θ. This would be the case when the dielectric and graphene are nearly lattice-matched, as occurs e.g. in highly-oriented stacked hBN-graphene structures, which have a small lattice mismatch of about 1.8% (a detailed discussion can be found in Ref. [79]). This effect, if present, would alter the values $\mathbf{q}_{A(B,C)}$ but otherwise would not change our discussion in an essential way.

Under an interlayer bias potential V_{12}, the tunneling current I_{12} is

$$\begin{aligned} I_{12} = & \frac{eN}{\hbar} \sum_{\boldsymbol{k}ss'j} |T_j^{ss'}(\boldsymbol{k})|^2 \int_{-\infty}^{\infty} \frac{d\omega}{2\pi} A_{1,s}(\boldsymbol{k}, \omega) \\ & \times A_{2,s'}(\boldsymbol{k} + \boldsymbol{q}_j, \tilde{\omega}) \left[f_1(\omega) - f_2(\tilde{\omega}) \right], \end{aligned} \tag{4.6}$$

where s (s') refers to the electron (+) and hole (−) bands of layer 1 (2), and $N = 4$ is the spin and valley degeneracy. The functions $f_i(\omega) = 1/[e^{\beta(\omega-\mu_i)} + 1]$ are the Fermi distribution functions for each layer, with $\beta = 1/k_{\mathrm{B}}T$ denoting the inverse thermal energy and μ_i the Fermi energies of each layer. The function $A_{i,s}$ is the spectral function of layer i and band s. The energy for the quantities in layer 2 is offset by $\tilde{\omega} = \omega + e\phi_{12}$ due to the built-up interlayer electrostatic potential ϕ_{12} [see Eq.(4.3)] between layers 1 and 2.

Because of capacitance effects, the interlayer electrostatic and chemical potentials are related to one another by

$$eV_{12} = \mu_1 - \mu_2 - e\phi_{12}, \tag{4.7}$$

where μ_i and ϕ_{12} are implicit functions of V_{12}. The quantity $T_j^{ss'}$ in Eq.(4.6) denotes the Hamiltonian coupling the two layers

$$T_j^{ss'}(\boldsymbol{k}) = \langle \boldsymbol{k}, s, 1 | \boldsymbol{T}_j | \boldsymbol{k} + \boldsymbol{q}_j, s', 2 \rangle, \quad |\boldsymbol{k}, s, i\rangle = \frac{1}{\sqrt{2}} \begin{pmatrix} 1 \\ s e^{i\theta_{\boldsymbol{k}}} \end{pmatrix}, \tag{4.8}$$

where $|\boldsymbol{k}, s, i\rangle$ is the two-component eigenvectors of the coupling term $\mathcal{H}_{1,2}$ in Eq.(4.3)

and $\theta_{\boldsymbol{k}}$ is the $\boldsymbol{k}$-vector polar angle.

The bistability can now be described by combining the relations (4.3) and (4.7) as follows. In a steady state, there is zero net flow of carriers into the middle layer. Therefore, when the external bias $V = V_{12}+V_{23}$ between top and bottom layers is fixed at V_{12}, the equilibrium current I is obtained by solving for V_{12} from the non-linear equation

$$I(V) = I_{12}(V_{12}) = I_{23}(V - V_{12}). \tag{4.9}$$

This procedure to obtain the I-V response is shown graphically in the inset of Fig.4-1(c). The straight line describes transport between layers 2 and 3 which is assumed to follow Ohm's law, so that $I_{23} = G_{23}V_{23}$, where G_{23} and V_{23} are the interlayer conductance and interlayer bias potential between layers 2 and 3, respectively.

4.3 Electrostatic feedback

In order to include the electrostatic feedback, Eq.(4.9) needs to be complemented with further electrostatic considerations that relate the variables for the voltage V_{ij}, the electrostatic potential ϕ_{ij} and the Fermi energy μ_i. It is important to note that all variables can be determined once the carrier densities in each layer, n_1, n_2 and n_3, are known. Indeed, assuming that there is no external gate, the neutrality condition relates the charge densities in the different regions of the device through the relation

$$n_1 + n_2 + n_3 = 0. \tag{4.10}$$

Furthermore, the application of an external bias potential V fixes the Fermi level difference between layer 1 and layer 3 as

$$eV = \mu_1 - \mu_3 + \frac{4\pi e^2}{\epsilon_{\rm r}}(n_1 d_{13} + n_2 d_{23}). \tag{4.11}$$

Here d_{ij} is the interlayer distance between layer i and layer j, $\epsilon_{\rm r}$ is the dielectric constant of the barrier material, and $\mu_i = \mathrm{sgn}(n_i)\hbar v_{\rm F}\sqrt{\pi n_i}$. In Eq.(4.11), I implicitly

assume that all layers are undoped at $V = 0$. Equations (4.9)-(4.11) then form a closed set of equations from which n_1, n_2 and n_3 can be obtained. The remaining variables, V_{ij} and ϕ_{ij}, are functions of n_i. In particular, the electrostatic potentials are

$$\phi_{12} = -4\pi e^2 d_{12} n_1/\epsilon_{\rm r}, \quad \phi_{23} = 4\pi e^2(n_1 d_{13} + n_2 d_{23})/\epsilon_{\rm r}, \tag{4.12}$$

whereas the interlayer bias potentials are

$$V_{12} = \mu_1 - (\mu_2 + \phi_{12}), \quad V_{23} = (\mu_2 + \phi_{12}) - (\mu_3 + \phi_{23}). \tag{4.13}$$

For simplicity, here I fix the Fermi energies in Eq.(4.6) to a constant value $\mu_i = \mu$. This is equivalent to turning off all capacitance effects. In this case, $V_{ij} = \phi_{ij}$ (see Fig.4-3). This approximation is valid in the regime

$$4e^2 d_{ij}\Delta_\theta/\epsilon_{\rm r}(\hbar v_{\rm F})^2 \approx 15 \cdot d_{ij}[\text{nm}]\Delta_\theta[\text{eV}]/\epsilon_{\rm r} \gg 1. \tag{4.14}$$

In this regime, minimal changes in carrier concentration induce large interlayer electrostatic potentials. The more realistic scenario which includes quantum capacitance effects [62], such that the $\mu_{1,2}$ is varying with V_{12}, is here considered in Sec.4.6. However, this more realistic picture only introduces small corrections to the tunneling current without major consequences to our bistability discussion.

4.4 Model parameters

In order to solve Eq.(4.9), I need to specify the matrix elements $\boldsymbol{T}_j$ in Eq.(4.8). A simple and explicit model for $\boldsymbol{T}_j$ and the wavevectors $\boldsymbol{q}_j$ is provided by Ref. [76]:

$$\boldsymbol{T}_j = t_\perp \begin{pmatrix} e^{i\varphi_j} & 1 \\ e^{-i\varphi_j} & e^{i\varphi_j} \end{pmatrix}, \quad \boldsymbol{q}_j = \frac{\Delta_\theta}{\hbar v_{\rm F}}(\sin\varphi_j, -\cos\varphi_j), \tag{4.15}$$

with $\varphi_A = 0$, $\varphi_B = 2\pi/3$, $\varphi_C = 4\pi/3$. This representation is obtained for small twisting angles after performing a θ rotation of phase space in layer 2 (see details in

Ref. [76]). It is also implicit in Eq.(4.15) that the top and bottom graphene lattices have a common lattice point [76]; a rigid horizontal translation between lattices adds an additional overall phase to the matrix $\boldsymbol{T}_j$ [77]. I stress, however, that relative phases in $\boldsymbol{T}_j$ do not alter in any significant way the physics of tunneling in Eq.(4.6). Furthermore, while the interlayer hopping amplitude $t_\perp$ is sensitive to several parameters, e.g. twist angle [78] and choice of dielectric material [79], its order of magnitude is mainly governed by the wavefunction overlap between the graphene layers. Such a dependence will be described below within the WKB approximation. Equations (4.3) and (4.15) are expected to be accurate for twist angles $\theta \lesssim 10°$, and energies of 1 eV [78].

For an estimation below, I use the value $\theta = 2°$. This defines an energy scale $\Delta_\theta = 0.37\,\mathrm{eV}$. Furthermore, I take a Lorentzian spectral function in Eq.(4.6) for both layers, $A_{i,s}(\boldsymbol{k},\omega) = 2\gamma/\left[(\omega - s\hbar v_{\mathrm{F}}|\boldsymbol{k}|)^2 + \gamma^2\right]$ with the linewidth $\gamma \sim 10$ meV. A finite linewidth γ is necessary to have a finite value of the peak current when $eV_{12} = \Delta_\theta$ (see Fig.4-3). The temperature and Fermi level of the system were taken to be $T = 0$ and $\mu_i = 0$, respectively. With reference to Eq.(4.6), I define the interlayer conductance

$$G_{12} = S g_{12}, \quad g_{12} = N \frac{|t_\perp|^2}{(\hbar v_{\mathrm{F}})^2} \frac{e^2}{\hbar}, \tag{4.16}$$

where S is the surface area of the device. The value of g_{12} is sensitive to the twist angle and the stacked dielectric material, if any, via the parameter $t_\perp$. Here I use $g_{12} = 10^{-7}\Omega^{-1}\mu\mathrm{m}^{-2}$. Similar values of g_{12} were measured in resonant tunneling devices which contained 4 layers of BN in-between the graphene layers [72]. For Z, I consider a value of $Z = G_{12}/G_{23} = 0.2$.

4.5 Bistable characteristics

The bistable I-V characteristics are shown in Fig.4-1(c). For a sufficiently large bias, $eV \gtrsim \Delta_\theta$, the current branches into two stable states. The low-resistance branch in Fig.4-1(c) corresponds to two layers at resonance (i.e. $eV_{12} \approx \Delta_\theta$), whereas the

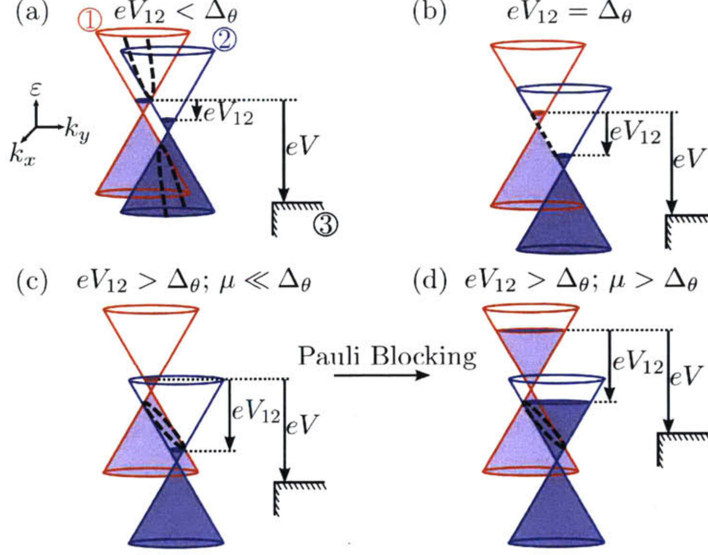

Figure 4-3: Regions in $\boldsymbol{k}$-space contributing to the resonant tunneling current for fixed V. These regions, indicated with black dashed lines at the intersection of the twisted Dirac cones, form conical paths in the $\boldsymbol{k}$-plane: when $eV_{12} < \Delta_\theta$ the lines form hyperbolic curves, and when $eV_{12} > \Delta_\theta$ the lines form ellipsoidal curves. When $eV_{12} = \Delta_\theta$, a van-Hove singularity in the tunneling density of states is obtained. As shown in panel (d), the non-resonant (high-resistance) bistable state ($eV_{12} > \Delta_\theta$) can be Pauli-blocked by adjusting the doping level. Doping thus affords a way to tune the current ratio between bistable branches in Fig.4-1(a). In this work it is assumed that the Dirac cones are aligned at $V = 0$ and capacitance effects are neglected. Layers are labelled 1-3 as in Fig.4-1(a).

high-resistance branch corresponds to a non-resonant state (i.e. $eV_{12} > \Delta_\theta$). I note that a third solution is also possible, indicated with a dashed line in the I-V response [see Fig.4-1(c)]. This solution, however, is unstable given that a small perturbation in δV_{12} will push the system away from this state.

The bistable bias range can be estimated as $\delta V \approx (I_{12}^{(\mathrm{pk})} - I_{12}^{(\mathrm{vl})})/G_{23}$, where $I_{12}^{(\mathrm{pk})}$ is the peak interlayer current and $I_{12}^{(\mathrm{vl})}$ is the valley interlayer current [see inset of Fig.4-1(c)]. To estimate $I_{12}^{(\mathrm{pk})}$ and $I_{12}^{(\mathrm{vl})}$, I first note that the phase factor $T_j^{ss'}(\boldsymbol{k})$ varies, upon integration in $\boldsymbol{k}$-space, in the range $0 \leq |T_j^{ss'}(\boldsymbol{k})| \leq 2t$ taking typical values $|T_j^{ss'}(\boldsymbol{k})| \approx t_\perp$. Thus, it is a good approximation to take energy band and wavevector-independent phase factors $|T_j^{ss'}(\boldsymbol{k})| = \bar{T}$. Furthermore, in the typical case scenario the model parameters satisfy $\gamma(\sim 10\,\mathrm{meV}) \ll \Delta_\theta(\sim 0.1 - 1\,\mathrm{eV})$. With this in mind, the integration of Eq.(4.6) allows an analytical expression in terms of line integrals in conical surfaces (see Fig.4-3). Using $\mu_{1,2} = 0$ and $V_{12} = \phi_{12}$, I find that

the non-resonant interlayer current takes the simple form

$$\frac{I_{12}(x)}{I_{12}^{(\mathrm{vl})}} = \frac{x^2 - 1/2}{\sqrt{2(x^2-1)}}, \quad I_{12}^{(\mathrm{vl})} = \frac{3\sqrt{2}\bar{T}^2}{4}\frac{G_{12}\Delta_\theta}{e}. \tag{4.17}$$

Here $x = eV_{12}/\Delta_\theta \gtrsim 1$ and $I_{12}^{(\mathrm{vl})}$ is the valley current obtained at $x = \sqrt{3/2}$. When $eV_{12}/\Delta_\theta = 1$; however, at the peak the current is at resonance and reaches a maximum value which is sensitive to γ. To leading order in γ, I obtain (see below)

$$I_{12}^{(\mathrm{pk})}/I_{12}^{(\mathrm{vl})} = \pi\sqrt{\Delta_\theta/2\gamma}, \tag{4.18}$$

where γ will in general depend on the amount and type of disorder and/or temperature. Equations (4.17) and (4.18) yield $e\delta V/\Delta_\theta \approx 3\sqrt{2}\bar{T}^2 Z[\pi\sqrt{\Delta_\theta/2\gamma} - 1]/4$. Importantly, very small values of Z ($G_{23} \gg G_{12}$) make the bistable bias range negligibly small, whereas large values of Z ($G_{23} \ll G_{12}$) would push the onset of the bistability region to very large bias potentials. Optimally, values of $Z \sim 1$ and very small γ would make the bistability effect more prominent.

Achieving a large current ratio between bistable states is desirable for applications; this facilitates the reading process in a bistable device. From Eqs.(4.17) and (4.18), we see that the current ratio between bistable branches is controlled by the parameter $Z\sqrt{\Delta_\theta/\gamma}$. For realistic values of disorder, this ratio can be in the 1-20 ballpark. It is interesting to note that these already high values can be boosted by means of Pauli blocking. As shown in Fig.4-3(c,d), for sufficiently heavily doped samples, the non-resonant bistable state (but not the resonant one) is Pauli-blocked. The degree of current ratio enhancement depends on second order processes which assist tunneling, such as carrier scattering with defects or disorder. These second order processes are not considered here.

To derive Eqs. (4.17) and (4.18) above, I assume that the phase factors $T_j^{ss'}$ in Eq.(4.8) are independent of wavevector and band index, i.e. $|T_j^{ss'}(\boldsymbol{k})| = \bar{T}$. Under this assumption, I_{12} depends only on the modulus of $\boldsymbol{q}_j$ but not on its direction, and $\sum_j |T_j^{ss'}(\boldsymbol{k})|^2 = 3\bar{T}^2$. Given that $\gamma \ll \Delta_\theta$, when $e\phi_{12} > \Delta_\theta$ (non-resonant state) we

can set $\gamma \to 0$ and thus take $A_{i,s}(\mathbf{k},\omega) = 2\pi\delta(\omega - s\hbar v_{\mathrm{F}}|\mathbf{k}|)$. The two delta-functions appearing in Eq.(4.6) can then be integrated in $\boldsymbol{k}$-ω space, resulting in a 1D integral along the contour of an ellipse:

$$\begin{aligned}\sum_{ss'}\int \frac{d\boldsymbol{k}}{(2\pi)^2}\int_{\omega_1}^{\omega_2}\frac{d\omega}{2\pi}\delta(\omega - s\hbar v_{\mathrm{F}}|\boldsymbol{k}|)\delta(\tilde{\omega} - s'\hbar v_{\mathrm{F}}|\boldsymbol{k}+\boldsymbol{q}|) \\ = \frac{\delta_{s,-}\delta_{s',+}}{16\pi^3(\hbar v_{\mathrm{F}})^2}\int_{\varphi_1}^{\varphi_2} d\varphi \frac{(e\phi_{12})^2 - \Delta_\theta^2\sin^2\varphi}{\sqrt{(e\phi_{12})^2 - \Delta_\theta^2}}.\end{aligned} \tag{4.19}$$

Here I denote $\tilde{\omega} = \omega + e\phi_{12}$. In addition, the limits of integration on ω are given by $\omega_1 = e\phi_{12} + \mu_2$ and $\omega_2 = \mu_1$, whereas the limits of integration on φ are

$$\varphi_i = \begin{cases} \pi/2, & x_i > 1 \\ \sin^{-1}(x_i), & -1 < x_i < 1 \\ -\pi/2, & x_i < -1 \end{cases}, \quad x_{1,2} = \frac{2\mu_{1,2} \pm e\phi_{12}}{\Delta_\theta}. \tag{4.20}$$

In obtaining Eq.(4.19), I parametrized $\boldsymbol{k}$-space using coordinates $k_x = k_r \sin\varphi/2$ and $k_y = \sqrt{k_r^2 - q^2}\cos\varphi/2$, with $\boldsymbol{q}$ conveniently aligned in the x-direction. The integration over k_r absorbs the first delta function, setting $k_r = e\phi_{12}/\hbar v_{\mathrm{F}}$. Integration over ω absorbs the second delta function, fixing the limits of integration $\varphi_{1,2}$ in Eq.(4.20). Importantly, because $\phi_{12} > \Delta_\theta$, the two delta functions in Eq.(4.19) can only be non-zero simultaneously when $s = -$ and $s' = +$ (i.e. holes of layer 1 tunnel into electronic states of layer 2, see Fig.4-3). Using $\mu_{1,2} = 0$ and $V_{12} = \phi_{12}$, Eqs.(4.19) and (4.20) result in Eq.(4.17).

When $e\phi_{12} = \Delta_\theta$, it is necessary to restore the finite linewidth to the Lorentzian spectral function $A_{i,s}(\mathbf{k},\omega) = 2\gamma/\left[(\omega - s\hbar v_{\mathrm{F}}|\mathbf{k}|)^2 + \gamma^2\right]$. In this case, the integral for the tunneling current yields

$$\begin{aligned}\sum_{ss'}\int \frac{d\boldsymbol{k}}{(2\pi)^2}\int_{\phi_{12}+\mu_2}^{\mu_1}\frac{d\omega}{2\pi}A_{1,s}(\boldsymbol{k},\omega)A_{2,s'}(\boldsymbol{k}+\boldsymbol{q},\omega) = \\ = \frac{2}{(\hbar v_{\mathrm{F}})^2\sqrt{\gamma\Delta_\theta}}\left[\int_{\mu_2}^{\Delta_\theta+\mu_1} d\omega\,|\omega(\omega-\Delta_\theta)|^{1/2} + \mathcal{O}(\gamma/\Delta_\theta)\right].\end{aligned} \tag{4.21}$$

In obtaining Eq.(4.21), I transformed the integral of the spectral functions into a

dimensionless integral of the form $I_{\rm res}(\epsilon) = \int d^2\boldsymbol{x}\{[f(\boldsymbol{x})^2+\epsilon][g(\boldsymbol{x})^2+\epsilon]\}^{-1}$. The functions f and g satisfy $f(0)=g(0)=0$ and have a null Jacobian $\det[\partial_{\boldsymbol{x}} f, \partial_{\boldsymbol{x}} g](0) = 0$ (here $\epsilon = \gamma/\Delta_\theta$). It can be shown that $I_{\rm res} \propto \epsilon^{-1/2}$, when $\epsilon \ll 1$. An expansion to leading order in powers of ϵ gives Eq.(4.21). Setting $\mu_{1,2}=0$ in Eq.(4.21), the peak current $I_{12}^{(\rm pk)}$ in Eq.(4.18) is obtained.

The geometric control of Z, an appealing aspect of our system, can be understood from the Bardeen Transfer Hamiltonian Theory [80,81]. In this theory, the interlayer coupling $t_\perp$ is calculated from the overlap of the wavefunctions of layers i and j in the barrier region, $t_\perp = (\hbar^2/2m_e^*)\int d\boldsymbol{S}\cdot(\psi_i^*\nabla\psi_j - \psi_j\nabla\psi_i^*)$, where $d\boldsymbol{S}$ is a surface area element. Considering electrons tunneling across a square potential barrier of height much larger than the electron kinetic energy, a tunneling matrix element of the form $t_\perp \propto \exp(-d_{ij}/\ell_{\rm wkb})$ is obtained, where $\ell_{\rm wkb}$ is the WKB decay length defined above. The expression of Z in Eq.(4.2) results from assuming barriers between layers 1-2 and 2-3 to be of the same material, in combination with Eq.(7.6).

4.6 Quantum capacitance effects

Although electrostatic doping of the graphene layers is not essential for the physics that I described in Sec.4.5, it is a convenient feature of bistability. In particular, for a fixed external bias potential, each bistable state exhibits different carrier concentrations. Thus, any in-plane measurement, such as conductance or magneto-transport, will be able to distinguish two distinct bistable states. Indeed, from the inset of Fig.4-1(c) we see that the interlayer bias potential for each bistable state differs by an amount $\delta V_{12} \sim \Delta_\theta/e$. Taking into account the capacitance of the layers, then the induced carrier difference between both states is approximately $\delta n \sim \epsilon_{\rm r}\Delta_\theta/4\pi e^2 d_{12}$ (here the quantum capacitance is not included). Using $\theta = 2^\circ$ between the two layers, $\epsilon_{\rm r} = 1$ and $d_{12} = 1\,{\rm nm}$, I obtain a carrier density difference $\delta n \sim 10^{12}\,{\rm cm}^{-2}$ between stable states. These large carrier density differentials can be used as a smoking gun for detecting intrinsic bistability.

A more refined model of the I-V response includes a bias dependence of the Fermi

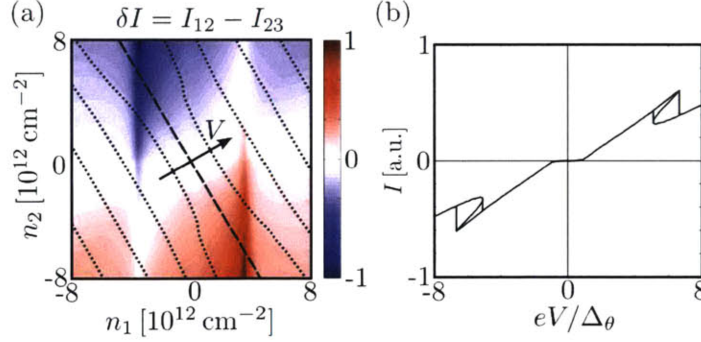

Figure 4-4: Self-consistent bistable solutions including quantum capacitance effects. For fixed V, I find n_1 and n_2 such that $\delta I = I_{12} - I_{23} = 0$ [see Eqs.(4.10)–(4.11)]. The bias isolines from Eq.(4.11) are marked with large dashed ($V = 0$) and small dotted (finite V) lines, with an arrow pointing towards increasing V. The self-consistent I-V curve, obtained from the intersection of $\delta I = 0$ and the V-isolines in (a), is plotted in panel (b).

energy. I numerically solve Eqs.(4.6)-(4.11), assuming a thin device separated by dielectric barriers of thickness $d_{12} = d_{23} = 1.4\,\mathrm{nm}$ (e.g. 4 layers of hBN) and dielectric constant $\epsilon_\mathrm{r} = 5$. The procedure to solve self-consistently the I-V response is shown in Fig.4-4(a), where n_1 and n_2 are taken as independent variables [n_3 is obtained from Eq.(4.10)], and $\delta I = I_{12} - I_{23}$ in Eq.(4.6) is numerically calculated (color map). For fixed V, indicated with dotted isolines in Fig.4-4a, the self-consistent solutions to the equilibrium equations are given by the pair (n_1,n_2) such that $\delta I = 0$.

The resulting I-V response is shown in Fig.4-4(b). Importantly, the I-V characteristics are qualitatively similar to those obtained by neglecting quantum capacitance effects. Furthermore, by inspection of the n_1 and n_2 axes in Fig.4-4(a), we see that the difference in carrier concentration δn between each bistable state is on the order of $\delta n \sim 10^{11}$-$10^{12}\,\mathrm{cm}^{-2}$. These carrier concentration differences can easily be detected by lateral transport measurements and may act as clear fingerprints of intrinsic bistability.

4.7 Other graphene-based bistable systems

Although I considered here for simplicity a two-step sequential tunneling structure where only one pair of layers can be resonant, similar ideas apply to more complex structures. Interesting examples include a two-step resonant-resonant structure,

opening the possibility for tristability, or multi-step 'cascade' devices. I also expect bistable I-V characteristics to be possible in twisted graphene trilayers in the absence of any dielectric material. Indeed, incommensurability between graphene lattices already suppresses interlayer hybridization, regardless of being spatially separated by a fraction of a nanometer, thus enabling the sequential tunneling regime [77]. Furthermore, the massless Dirac spectrum, and thus Eq.(4.3) and the subsequent transport model, remain valid but with a modified Fermi velocity [76]. I stress, however, that stacked dielectric materials have two important advantages: (i) they enable tuning the interlayer coupling and (ii) they facilitate the interlayer potential build-up in order to achieve a resonant behavior.

4.8 Chapter summary

In summary, graphene-based van der Waals heterostructures afford a new platform to realize devices with tunable I-V characteristics, in particular those with intrinsically bistable and hysteretic behavior. System parameters required to realize the bistable behavior are readily accessible in current experiments. The atomic scale interlayer distances can result in a fast response and in large packing-densities, making these heterostructures appealing for a variety of applications.

Chapter 5

Thermionic emission and negative dI/dV in photoactive graphene heterostructures

Graphene, because of its unique characteristics, is of keen interest for optoelectronics research in areas such as photodetection, solar cells and light-emitting devices [82–85]. Transport in photoactive graphene heterostructures, originating from the dynamics of photogenerated hot carriers, is governed by the processes of thermionic emission, electron-lattice thermal imbalance and cooling. These processes give rise to interesting photoresponse effects. In this chapter[1] I predict that interlayer transport in graphene heterostructures operating in the hot-carrier regime leads to an unusual type of photoresponse, namely, a negative differential resistance (NDR).

The mechanism for NDR relies on the interplay of two effects. First, the phase space available for phonon scattering rapidly increases with doping, enhancing the electron-lattice cooling and thereby altering the number of hot carriers in the system. Second, the large capacitance of the atomically thin device renders the carrier density in graphene layers sensitive to the interlayer potential difference. These two effects

[1]Reproduced with permission from J. F. Rodriguez-Nieva, M. S. Dresselhaus, L. S. Levitov, Thermionic Emission and Negative dI/dV in Photoactive Graphene Heterostructures, *Nano Letters* **15**, 1451 Copyright 2015 by the American Chemical Society.

combined together result in a reduction of the electronic temperature and a suppression of thermionic current upon an increase of the bias potential V_b. The NDR effect arises when this suppression overwhelms the increase in the field-effect transport under bias. Such an NDR mechanism manifests itself as an enhanced photo-current peaked at a bias potential well below the onset of the conventional field-emission regime. This peak, combined with a gate-controlled closed-circuit current that is present at zero bias voltage, serve as signatures of hot-carrier dominated transport.

Photoactive NDR architectures are a class of their own, and are well suited for optoelectronic applications. In particular, the fast response and in situ tunability of graphene devices make them ideal as photo-active switches or light-detectors with high gain. The NDR effect in photo-active devices, analyzed below, is distinct from the one in traditional NDR devices, such as Gunn diodes [86] or resonant tunneling diodes [72, 87] which rely on non-linearities under the application of large electric fields in the absence of light.

5.1 Thermionic transport

While in general both electrons and holes can contribute to thermionic transport, in practice transport is often dominated by a single carrier type. In the case of hBN, the barrier heights are $\Phi_{\rm el} \sim 3.5\,{\rm eV}$ for electron transport and $\Phi_{\rm h} \sim 1.3\,{\rm eV}$ for hole transport [88]. We can therefore treat the interlayer transport in an hBN-based system as dominated by a single carrier type (holes).

Below I focus on the behavior in wide-barrier structures, where thermionic emission of thermally activated carriers dominates over direct tunneling. This is the case for hBN thicknesses exceeding 4-5 monolayers ($d \sim 1\,{\rm nm}$) [16] at sufficiently high temperatures. Thermionic currents are described by a particularly simple model when

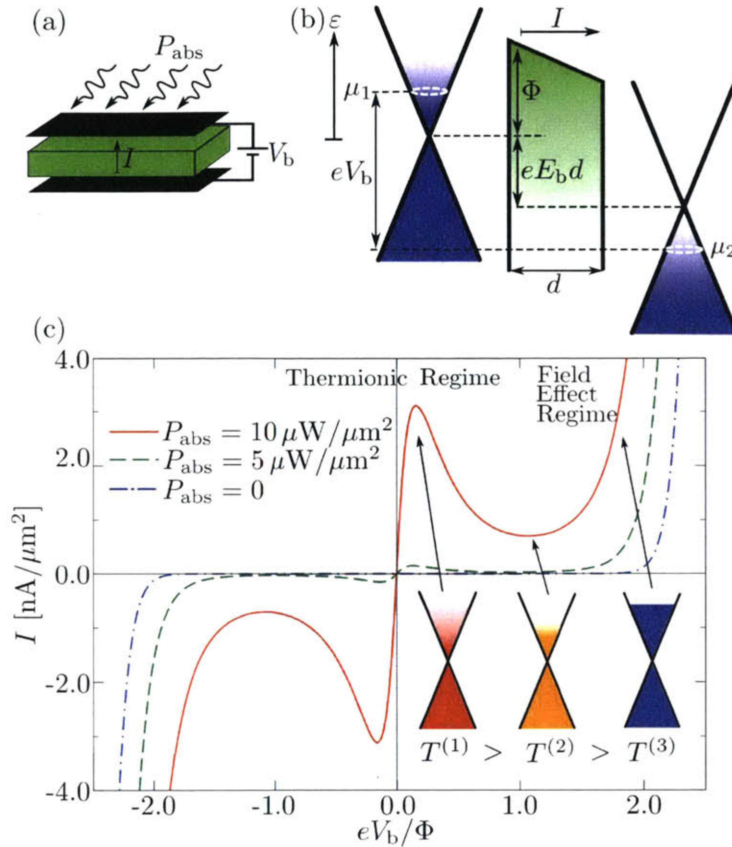

Figure 5-1: The Negative Differential Resistance (NDR) effect in a photoactive heterostructure operated in the thermionic emission regime. Shown are (a) device schematics, (b) electronic band structure with the quantities discussed in the text marked, and (c) the I-V dependence under optical pumping obtained from Eqs. (5.4)–(5.7). The bias voltage V_b controls the electron cooling through electrostatic doping of graphene layers. An enhancement in the cooling power upon increased V_b triggers the carrier temperature dropping [marked $T^{(1,2,3)}$ in (c)]; see also simulation results in Fig.5-4(a). The resulting suppression of the thermionic current leads to *negative* dI/dV (in the grey region). For larger bias values, transport is dominated by field emission, yielding *positive* dI/dV outside the grey region. Shown here are results for both graphene layers undoped at $V_b = 0$. Results for nonzero doping are presented in Figs.5-2 and 5-3.

both graphene layers are at neutrality at $V_\mathrm{b} = 0$:[2]

$$I(V_\mathrm{b}, T) = (g_0 k_\mathrm{B} T/e) e^{-\Phi/k_\mathrm{B}T} \sinh(eV_\mathrm{b}/2k_\mathrm{B}T), \tag{5.1}$$

where I is the current density per unit area and the g_0 value is estimated in Eq.(5.8). This expression in Eq.(5.1) follows from a general microscopic model at not too high bias V_b, such that the effect of anti-symmetric doping induced by $V_\mathrm{b} \neq 0$ is stronger than the corresponding change in the barrier skewness [see derivation and discussion in the paragraph before Eq.(5.17)]. For larger bias values, field corrections to the barrier potential become important and must be accounted for; this is done in a microscopic model developed below. I also note that the electronic distribution is typically non-exponential when relaxation is slow. Slow relaxation would make the distribution tails more pronounced, ultimately enhancing the thermionic effects.

5.2 Negative differential resistance (NDR)

The steep dependence of I on T and V_b in Eq.(5.1) leads to NDR by the following mechanism. For electrons in thermal equilibrium with the lattice, Eq. (5.1) predicts a monotonic I-V dependence. A very different behavior, which is key for NDR, arises under pumping. As pictured schematically in Fig.5-1(c) for three values $T^{(1)} > T^{(2)} > T^{(3)}$, in the hot-carrier regime the electron temperature T becomes highly sensitive to V_b. The temperature-bias coupling arises because of the large interlayer capacitance producing bias-dependent doping in the graphene layers. An increase in carrier density leads to a faster electron-lattice cooling, which reduces thermal imbalance $\delta T = T - T_0$, with T_0 the lattice temperature. The dependence in Eq.(5.1) then predicts suppression of thermionic emission. If strong enough, this suppression can lead to negative dI/dV. The NDR effect takes place in the grey region marked

[2]The expression for thermionic current density in Eq.(5.1) features a dependence on the external bias and a power-law temperature dependence distinct from that known for the 3D case, where $I_\mathrm{th} \propto T^2 e^{-\Phi/k_\mathrm{B}T}$. This reflects the difference in the transport processes at the interface. Conventional thermionic emission (3D) is described as the flux of free particles with energies $\varepsilon > \Phi$ in the direction normal to the surface. In contrast, in our case transport depends on elastic scattering mechanisms at the graphene/hBN interface generating an out-of-plane current, as described in the text.

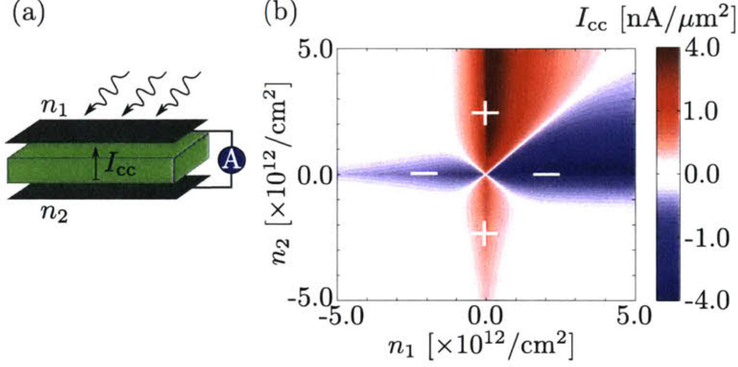

Figure 5-2: The closed-circuit current I_{cc} induced by optical pumping. In the transport regime dominated by hot carriers, the value and polarity of I_{cc} are sensitive to the carrier densities n_1, n_2 in the graphene layers. Shown are (a) experimental schematics, and (b) the dependence I_{cc} *vs.* n_1 and n_2 for $P_{abs} = 10\,\mu\text{W}/\mu\text{m}^2$ and $V_b = 0$. The four-fold pattern with multiple changes of the current polarity arises due to the strong cooling power dependence on carrier concentration (a non-linear color scale is used to amplify the features of interest).

in Fig.5-1(c).

The sensitivity of the electron-lattice cooling to carrier concentration provides a smoking gun for the regime dominated by hot carriers, helping distinguish it from the conventional resonant tunneling NDR mechanisms, such as those discussed in Refs. [17, 18]. In that regard, I mention that for the more general case of unequal carrier densities ($n_1 \neq n_2$ at $V_b = 0$), this analysis predicts that the interlayer thermionic transport persists even at zero bias. As illustrated in Fig.5-2, this produces a closed-circuit current at $V_b = 0$ with a characteristic density dependence: a four-fold pattern with multiple polarity changes. Such a pattern provides a characteristic signature of hot-carrier dominated transport.

The strength of the hot-carrier effects, reflected in the response of T to V_b [see Fig.5-4(a)], can be characterized by the dimensionless quantity

$$\alpha_{hc} = -\frac{\Phi}{T}\frac{dT}{d(eV_b)}. \tag{5.2}$$

The value α_{hc} depends mainly on the power P_{abs} pumped into the electronic system and on the thickness d of the barrier via the capacitance effect. As we will see, α_{hc} governs the non-monotonic I-V dependence: the condition for NDR can be stated as

$\alpha_{\rm hc} > 1/2$. I will argue that values as large as $\alpha_{\rm hc} \sim 25$ can be reached under realistic conditions.

5.3 Thermionic transport model

For thermionic transport over the barrier, as well as for tunneling through it, I adopt a quasi-elastic but momentum non-conserving approximation. Indeed, a number of momentum scattering mechanisms at the interface are possible, such as scattering by defects, intrinsic phonons, substrate phonons, *etc.* Typical energy exchange in these processes is small on the barrier height scale Φ. With this in mind, I use the (quasi-elastic) WKB model for the interlayer transition matrix element:

$$t_\perp(\varepsilon) = t_0 e^{-\frac{1}{\hbar}\int_0^{x_*} p(x)dx}, \quad \frac{p^2(x)}{2m_e^*} = \Phi - eE_{\rm b}x - \varepsilon, \tag{5.3}$$

for $\varepsilon < \Phi$, and $t(\varepsilon) = t_0$ for $\varepsilon > \Phi$, where t_0 is an energy-independent prefactor which depends on the barrier material properties. In Eq. (5.3), $E_{\rm b}$ is the electric field within the barrier due to interlayer bias, see Eq.(5.7), m_e^* is the electron effective mass in the dielectric, and x_* is the classical turning point for the skewed barrier potential, $x_* = \min[d, (\Phi - \varepsilon)/eE_{\rm b}]$, see Fig. 5-1(b). Here, for the sake of simplicity, I ignore the effect of attraction to image charges, described by a $-1/|x| - 1/|x-d|$ potential. For a large barrier width, this gives rise to the barrier height Schottky dependence on the square root of $E_{\rm b}$. The effect is less dramatic for the not-so-large barrier widths analyzed below.

Assuming an elastic but momentum non-conserving interlayer transport, the vertical current $I(V_{\rm b})$ can be expressed through barrier transmission and carrier distribution [81]:

$$I(V_{\rm b}) = e\sum_{\varepsilon, ij} \frac{2\pi}{\hbar}|t_{ij}(\varepsilon)|^2 D_1(\varepsilon)D_2(\tilde\varepsilon)[f_1(\varepsilon) - f_2(\tilde\varepsilon)], \tag{5.4}$$

where, due to the built-in field between layers, the energy for the quantities in layer 2 is offset by $\tilde\varepsilon = \varepsilon + eE_{\rm b}d$ [see Fig.5-1(b)]. Here I is the current per unit area and $f_1(\varepsilon) = [e^{(\varepsilon-\mu_1)/k_{\rm B}T_1} + 1]^{-1}$, $f_2(\varepsilon) = [e^{(\varepsilon-\mu_2)/k_{\rm B}T_2} + 1]^{-1}$ are the Fermi distribution

functions, the sum in Eq.(5.4) denotes integration over ε and summation over spins and valleys. I use $t_{ij}(\varepsilon) = \delta_{ij}t(\varepsilon)$ defined in Eq.(5.3), and the density of states per spin/valley $D_{1,2}(\varepsilon) = |\varepsilon|/2\pi(\hbar v_{\rm F})^2$. The temperatures established under pumping in unequally doped layers are generally distinct, $T_1 \neq T_2$, reflecting the cooling rates density dependence. Also, importantly, the electrostatic potential between layers, $E_{\rm b}d$, is distinct from the bias voltage $V_{\rm b}$. This is so because the quantum capacitance effects, prominent at small carrier densities, [62] make the quantites μ_1 and μ_2 bias-dependent. These effects are investigated below.

5.4 Electrostatic coupling model

A feature of our system which is key for NDR is the large mutual capacitance of graphene layers, which couples $V_{\rm b}$ with the carrier density and makes the hot-carrier properties of each layer tunable. This coupling acts as a knob producing big changes in the hot-carrier photoresponse through modest changes of carrier concentration on the order $\delta n \sim 10^{12}\,{\rm cm}^{-2}$.[3] Such bias-induced doping changes are routine in graphene/hBN systems [15].

The bias-induced changes in the carrier densities of graphene layers, as well as in the electric field $E_{\rm b}$ between the layers, can be described by a simple electrostatic model. I consider a dual-gated device with fixed charge densities $n_{\rm T}$, $n_{\rm B}$ in the top and bottom gates, respectively. The neutrality condition relates the charge densities in the different regions of the device as

$$n_{\rm T} + n_1 + n_2 + n_{\rm B} = 0, \tag{5.5}$$

where n_1, n_2 are carrier densities on the graphene layers. The field $E_{\rm b}$ is related to

[3] Such carrier densities are sufficient to trigger the NDR regime. Indeed, I assume, for concreteness, that electron-lattice cooling is dominated by the disorder-assisted mechanism. Taking a typical pump power value $P_{\rm abs} \sim 10\,\mu{\rm W}/\mu{\rm m}^2$, equating it to $P_{\rm dis}$, and using values $k_{\rm F}\ell_{\rm d} \sim 100$ and $T = 2T_0 \sim 600\,{\rm K}$, then Eq. (5.13) yields typical carrier densities on the order of $n \sim 10^{12}{\rm cm}^{-2}$. Similar values are obtained for the acoustic phonon mechanism in the absence of disorder. The hot-carrier transport regime is therefore realized when the carrier density is $n \lesssim 10^{12}\,{\rm cm}^{-2}$, whereas field emission dominates for $n \gtrsim 10^{12}\,{\rm cm}^{-2}$.

these quantities through Gauss' law:

$$\epsilon_{\mathrm{r}} E_{\mathrm{b}} = 2\pi e \left(n_{\mathrm{T}} + n_1 - n_2 - n_{\mathrm{B}}\right), \tag{5.6}$$

where ϵ_{r} is the dielectric constant of the barrier. A bias voltage V_{b} applied between the graphene layers results in

$$eV_{\mathrm{b}} = \mu_1 - \mu_2 + eE_{\mathrm{b}}d, \tag{5.7}$$

where μ_1 and μ_2 are the Fermi levels for layers 1 and 2. With doping-dependent $\mu_{1,2}$, Eq.(5.7) accounts for the quantum capacitance effects. Here I will use the $T = 0$ expression $\mu_i = \mathrm{sign}(n_i)\hbar v_{\mathrm{F}}\sqrt{\pi|n_i|}$, which provides a good model over most of the relevant carrier density range.

The three unknown variables n_1, n_2 and E_{b} can now be found by solving the three equations (5.5)-(5.7), once the external variables n_{T}, n_{B} and V_{b} are fixed. Throughout this work I focus on the symmetric case when $n_{\mathrm{T}} = n_{\mathrm{B}} = -n_0$ with no interlayer bias applied (which corresponds to both graphene layers at neutrality when the gates are uncharged). In this case, Eqs. (5.5),(5.6) can be restated as $n_1 = n_0 + \delta n$, $n_2 = n_0 - \delta n$, and $\epsilon_{\mathrm{r}} E_{\mathrm{b}} = 4\pi e \delta n$. Then, plugging these values into Eq. (5.7), the density imbalance δn can be obtained. The built-in field E_{b} matters in two different ways: the electrostatic potential value $eE_{\mathrm{b}}d$ enters the WKB model, Eq. (5.3), as well as in the offset between $D_1(\varepsilon)$ and $D_2(\varepsilon)$ in Eq. (5.4).

5.5 Current-bias characteristics

The I-V dependence for the case $n_0 = 0$ is shown in Fig.5-1; for finite values $n_{\mathrm{T}} = n_{\mathrm{B}} = -n_0$ it is shown in Fig.5-3. In the simulation, I first determine $\mu_{1,2}$ from Eqs.(5.5)-(5.7) as a function of V_{b} and n_0. Using the $\mu_{1,2}$ values, the electronic temperatures $T_{1,2}$ are determined from energy balance considerations, see Eq.(5.9) below. Finally, using the calculated values $\mu_{1,2}$, $T_{1,2}$, and E_{b}, the current is obtained from Eq.(5.4). I use hBN barrier parameters for numerical estimates, with a (hole)

barrier height $\Phi \sim 1.3\,\mathrm{eV}$ [88], dielectric constant $\epsilon_{\mathrm{r}} \sim 5$, thickness $d = 6\,\mathrm{nm}$ (~ 20 monolayers). Room temperature is assumed, $T_0 = 300\,\mathrm{K}$, unless stated otherwise.

The prefactor value Γ in Eq.(5.3) can be related to the measured conductance. Physically, Γ accounts for the processes in which tunneling couples to phonons or defects. The rates for these processes, which typically vary from interface to interface, can be estimated from transport measurements. Linearizing Eq.(5.4) in eV_{b} for $k_{\mathrm{B}}T \ll \Phi$, and accounting for the thermionic contribution due to $\varepsilon \approx \Phi$, the zero-bias conductance per unit area is

$$G = \frac{g_0}{2} e^{-\Phi/k_{\mathrm{B}}T}, \quad g_0 = 4\pi N D_1(\Phi) D_2(\Phi) |\Gamma|^2 \frac{e^2}{\hbar}, \tag{5.8}$$

where I take $T_1 = T_2$. Here $N = 4$ is the spin/valley degeneracy, and g_0 is a prefactor in Eq. (5.1). The activation T dependence is consistent with that measured for dark current [59]. Comparison with values $G \sim 10^{-7}\,\Omega^{-1}\mu\mathrm{m}^{-2}$ measured at room temperature, and $\Phi \sim 0.4\,\mathrm{eV}$ [59], yields values $g_0 \sim 1\,\Omega^{-1}\mu\mathrm{m}^{-2}$ and $\Gamma \sim 0.5\,\mathrm{eV\AA}$.

5.6 Hot carrier effects

Next I discuss how hot-carrier effects result in a coupling between the electronic temperature and the chemical potential for each graphene layer. In the continuous wave regime, the power P_{abs} pumped into the electronic system is distributed among the electron and lattice degrees of freedom. For simplicity, I use a two-temperature model, describing electrons by a temperature distinct from the lattice temperature, $T > T_0$, valid when the carrier-carrier scattering rate is faster than the electron-lattice relaxation rate. Assuming spatially uniform in-plane temperatures and chemical potentials, the total cooling power obeys the energy balance condition

$$P_{\mathrm{abs}} = P_{\mathrm{ac}}(\mu_i, T_i) + P_{\mathrm{opt}}(\mu_i, T_i) + P_{\mathrm{dis}}(\mu_i, T_i), \tag{5.9}$$

written separately for each layer $i = 1, 2$. Here I ignored effects such as direct interlayer energy transfer as well as the heat drained through the contacts. Equation (5.9)

accounts for three cooling pathways intrinsic to graphene, mediated by acoustic and optical phonons ($P_{\rm ac}$, $P_{\rm opt}$) [47,48], and the disorder-assisted acoustic phonon mechanism ($P_{\rm dis}$) [52]. The cooling rates in Eq.(5.9) also depend on the lattice temperature T_0, however it suffices to treat T_0 as a fixed parameter, since the heat capacity of the lattice greatly exceeds that of the electron system.

The intralayer Joule heating is small and thus need not be included in Eq. (5.9). Indeed, typical vertical current values obtained in devices of active area $\sim 1\,\mu{\rm m}^2$ and under a bias $V_{\rm b} \sim 1\,{\rm V}$ do not exceed a few nA [15,16,59]. This yields Joule heating sources which are at least three orders of magnitude smaller than the powers pumped optically. The interlayer energy transfer as well as the heat drained through contacts can be ignored in the energy balance in Eq. (5.9) for similar reasons.

The cooling power is a strong function of doping for the acoustic-phonon contributions $P_{\rm ac}$ and $P_{\rm dis}$. This is so because acoustic phonon scattering is dominated by quasi-elastic scattering processes at the Fermi surface, and also because of the strong dependence of the electron-phonon coupling on the phonon energy. The resulting dependence on the chemical potential takes the form [47,52]

$$P_{\rm ac} \propto \mu^4 (T - T_0), \quad P_{\rm dis} \propto \mu^2 (T^3 - T_0^3)/k_{\rm F}\ell_{\rm d} \tag{5.10}$$

in the degenerate limit $k_{\rm B}T \ll \mu$. The factor $1/k_{\rm F}\ell_{\rm d}$, where $\ell_{\rm d}$ is the disorder mean free path, describes the dependence of $P_{\rm dis}$ on disorder strength. In contrast, the contribution $P_{\rm opt}$ is essentially μ-independent. Since the optical phonon energy in graphene is quite large, $\hbar\omega_0 \sim 0.2\,{\rm eV}$, the value $P_{\rm opt}$ is quite small, behaving as $P_{\rm opt} \propto \exp(-\hbar\omega_0/k_{\rm B}T)$ for $k_{\rm B}T, \mu \lesssim \hbar\omega_0$. The ratio $P_{\rm ac}/P_{\rm opt}$ is therefore small near charge neutrality but can be order-one for strongly doped graphene with typical doping $n \sim 10^{13}\,{\rm cm}^{-2}$ [47]. The cooling power strong dependence on μ can trigger the temperature dropping upon an increase in μ, i.e. $dT/d\mu < 0$, see Fig.5-4(a).

Explicitly, the contribution to cooling power due to acoustic phonons, obtained

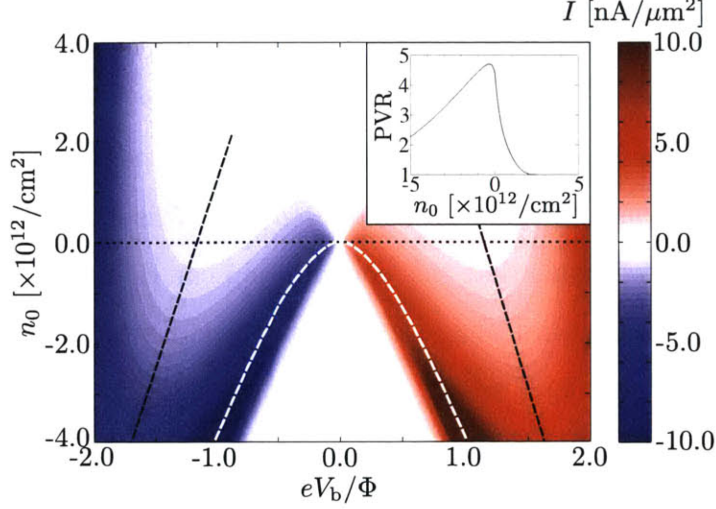

Figure 5-3: Map of the open-circuit current I induced by optical pumping. Plotted is I as a function of eV_b/Φ and zero-bias doping n_0 (equal for both layers), for $P_{abs} = 10\,\mu W/\mu m^2$. The current peak positions track the V_b values where the emitter is at neutrality (white dashed line). Local minima of I *vs.* V_b are marked with black dashed lines. The $n_0 = 0$ slice, plotted in Fig.5-1(c), is marked with a dotted line. The peak-to-valley ratio (PVR) *vs.* n_0 is shown in the inset.

for pristine graphene, is given by [47]

$$P_{ac} = 4\gamma_{ac}(T - T_0)\int_0^\infty d\varepsilon\ \varepsilon^3\left[f(\varepsilon) + 1 - f(-\varepsilon)\right], \quad \gamma_{ac} = \frac{\hbar U_D^2 k_B}{8\pi\rho(\hbar v_F)^6}, \tag{5.11}$$

where $f(\epsilon) = [e^{\beta(\epsilon-\mu)} + 1]^{-1}$ is the Fermi distribution function, U_D is the deformation potential, and ρ is the mass density of the graphene monolayer. In the degenerate limit, $\mu/k_B T \gg 1$, the integral in Eq. (5.11) yields

$$P_{ac} = \gamma_{ac}\mu^4(T - T_0). \tag{5.12}$$

This contribution to cooling, due to its strong dependence on μ, becomes very small near the Dirac point.

Disorder-assisted acoustic phonon cooling originates from electron-phonon scattering in the presence of disorder, such that part of phonon momentum is absorbed by disorder. Evaluated for a short-range disorder model, this mechanism yields cooling

power [52]

$$P_{\rm dis} = \gamma_{\rm dis}\mu^2(T^3 - T_0^3), \quad \gamma_{\rm dis} = \frac{2U_D^2 k_{\rm B}^3}{\rho c_{\rm s}^2 \hbar (\hbar v_{\rm F})^4 k_{\rm F}\ell_{\rm d}}, \tag{5.13}$$

where $k_{\rm F}\ell_{\rm d}$ is the dimensionless disorder mean free path parameter, $c_{\rm s}$ is the speed of sound in graphene, and the degenerate limit $\mu \gg k_{\rm B}T$ is assumed. The quadratic dependence of $P_{\rm dis}$ on μ means that this contribution can dominate over $P_{\rm ac}$ near the Dirac point. For both $P_{\rm ac}$ and $P_{\rm dis}$, I use values of $U_D \approx 20\,{\rm eV}$, $c_{\rm s} \approx 2 \cdot 10^4\,{\rm m/s}$, $\rho \approx 7.6 \cdot 10^{-11}\,{\rm kg/cm^2}$ and $k_{\rm F}\ell_{\rm d} = 100$.

Finally, the optical phonon cooling power is [47]

$$P_{\rm opt} = \frac{\hbar(\hbar\omega_0)^3}{4\pi\rho a_0^4(\hbar v)^2}\left[f_{\rm B}(\hbar\omega_0/k_{\rm B}T) - f_{\rm B}(\hbar\omega_0/k_{\rm B}T_0)\right]\mathcal{F}(T,\mu), \tag{5.14}$$

where a flat optical phonon dispersion $\hbar\omega_0 = 0.2$ eV is assumed. The quantity $f_{\rm B}(x)$ denotes the Bose-Einstein distribution $[e^x - 1]^{-1}$. The quantity $\mathcal{F}(T,\mu)$ is a dimensionless integral

$$\mathcal{F}(T,\mu) = \int_{-\infty}^{\infty} dx |x(x-1)| \left[f(\hbar\omega_0(x-1)) - f(\hbar\omega_0 x)\right]. \tag{5.15}$$

For weak doping, $\mu \ll \hbar\omega_0$, and $k_{\rm B}T \ll \hbar\omega_0$, I can approximate $f(\varepsilon)$ by a step function $\theta(-\varepsilon)$. Integration in Eq. (5.15) then yields $\mathcal{F}(T,\mu) \approx 1/6$, giving

$$P_{\rm opt} = \gamma_{\rm opt}\left[f_{\rm B}(\hbar\omega_0/k_{\rm B}T) - f_{\rm B}(\hbar\omega_0/k_{\rm B}T_0)\right], \quad \gamma_{\rm opt} = \frac{\hbar(\hbar\omega_0)^3}{24\pi\rho a_0^4(\hbar v_{\rm F})^2}. \tag{5.16}$$

At temperatures T, $T_0 \ll \hbar\omega_0$ this gives a simple exponential dependence in Eq.(2.30). The exponential temperature dependence in $P_{\rm opt}$ makes this contribution small at low temperatures[4].

The transition between the hot-carrier dominated regime, and the conventional field emission regime can be controlled by the power pumped into the electronic system. In the simulation I used the values for $P_{\rm abs}$ typical of laboratory lasers below saturation [89] (a few mW per a μm-wide spot). I take $P_{\rm abs}$ to represent the power

[4] Although small, $P_{\rm opt}$ can still dominate over the other cooling mechanisms, particularly near the Dirac point where $P_{\rm ac} \propto \mu^4$ and $P_{\rm dis} \propto \mu^2$.

absorbed in each graphene layer (2.3% of incident power [85]). The $P_{\rm abs}$ values used are quoted in Figs.5-1 and 5-4 panels and in the captions of Figs.5-2 and 5-3. As shown in Fig.5-1(c), a strictly monotonic I-V response obtained at $P_{\rm abs} = 0$, is transformed into an N-shaped NDR dependence upon growing pump power.

5.7 Zero bias doping effect

The impact of doping n_0 (taken to be equal to each other on for both layers at $V_{\rm b} = 0$) on the I-V dependence is illustrated in Fig.5-3. In this figure we see that the current peaks are shifted towards higher $V_{\rm b}$ values upon n_0 growing more negative [compare to Fig.5-1(c) which shows the $n_0 = 0$ slice]. The peaks track the $V_{\rm b}$ values at which the emitter layer is bias-doped to charge neutrality. This is to be expected since the electron-lattice imbalance is maximal at neutrality. A peak-to-valley ratio (PVR) as high as ~ 5 can be obtained (see Fig. 5-3 inset). For $n_0 > 0$, in contrast, the emitter layer is never at charge neutrality for any value of $V_{\rm b}$, resulting in the N-shaped dependence fading out.

The NDR effect is suppressed under a high bias potential when the field emission of carriers with energies below the barrier height overwhelms thermionic emission. As shown in Fig.5-1, the high bias region $eV_{\rm b}/\Phi > 1$ is characterized by I monotonically growing with increasing $V_{\rm b}$. This behavior arises because lowering the barrier height facilitates tunneling and also because the growing carrier density results in a faster cooling, thereby reducing the electron-lattice thermal imbalance [see Fig.5-1(c) inset].

5.8 Criterion for NDR

Next, I proceed to derive a simple criterion for NDR. I will focus on the fully-neutral case $n_0 = 0$ (both graphene layers are undoped at $V_{\rm b} = 0$) pictured in Fig.5-1. In this case, due to symmetry, we have $T_1 = T_2 = T$ and $n_1 = -n_2$ for any $eV_{\rm b}$. Further, assuming a small bias and/or a not-too-wide barrier, I can approximate the bias-induced chemical potentials as $\mu_{1,2} \approx \pm eV_{\rm b}/2$. This simple relation is valid for

$eV_\mathrm{b} \ll \epsilon_\mathrm{r}(\hbar v)^2/e^2 d$, corresponding to the last term in Eq.(5.7) much smaller than $\mu_1 - \mu_2$. Lastly, by accounting for the dominant role of thermionic emission, I model transmission as a step function, $|t(\varepsilon)|^2 \approx \Gamma^2\Theta(\varepsilon - \Phi)$. I then integrate in Eq. (5.4) over energies $\varepsilon \geq \Phi \gg \max[k_\mathrm{B}T,\ V_\mathrm{b}]$, approximating $D_{1,2}(\varepsilon)$ as a constant and the Fermi distribution tail as $e^{-(\varepsilon-\mu)/k_\mathrm{B}T}$. This yields Eq.(5.1) to leading order in V_b/Φ and $k_\mathrm{B}T/\Phi$ with the prefactor g_0 given in Eq.(5.8). While the validity of Eq.(5.1) is limited to d which are not too small and also not too large, I find that this equation predicts NDR to occur in the parameter range close to that found from the full microscopic model used to produce Fig.5-1 through Fig.5-4.

The criterion for NDR can be derived by taking the derivative dI/dV_b in Eq. (5.1) and setting it equal to zero, giving

$$\left(1 + \frac{k_\mathrm{B}T}{\Phi}\right)\tanh x - \frac{x}{\Phi/k_\mathrm{B}T} = \frac{1}{2\alpha_\mathrm{hc}}, \quad x = eV_\mathrm{b}/2k_\mathrm{B}T, \tag{5.17}$$

where α_hc is the quantity $-(\Phi/eT)dT/dV_\mathrm{b}$ introduced above, describing the carrier temperature dependence *vs.* V_b. The α_hc value controls the NDR effect. Maximizing the left-hand side of Eq.(5.17) in x I find the value $f(\lambda) = \lambda^{1/2} - (\lambda - 1)\tanh^{-1}\lambda^{-1/2}$ parameterized with $\lambda = 1 + (\Phi/k_\mathrm{B}T)^{-1}$, which is attained at $x_* = \sinh^{-1}\sqrt{\Phi/k_\mathrm{B}T}$. It is straightforward to check that $f(\lambda) \leq 1$ for all $\lambda \geq 1$. This gives the NDR condition $\alpha_\mathrm{hc} > 1/2$. Below I use this condition, derived for $n_0 = 0$, as an approximation for the more general case of $n_0 \neq 0$.

To estimate α_hc as a function of the model parameters, it is convenient to factorize α by applying the chain rule as $\alpha_\mathrm{hc} = \alpha_T \cdot \alpha_\mu$, giving

$$\alpha_T(P) = -\frac{\mu}{T}\frac{dT}{d\mu}, \quad \alpha_\mu(d) = \frac{\Phi}{e\mu}\frac{d\mu}{dV_\mathrm{b}}. \tag{5.18}$$

Here α_T depends *only* on the cooling pathways through Eq. (5.9), while α_μ depends *only* on the barrier properties through the quantum capacitance effect of Eq. (5.7). Below I use Eq.(5.18) to estimate α_hc and show that the NDR condition $\alpha_\mathrm{hc} > 1/2$ can be readily met.

To estimate α_T I analyze the degenerate regime $\mu \gg k_\mathrm{B}T$, where the doping-

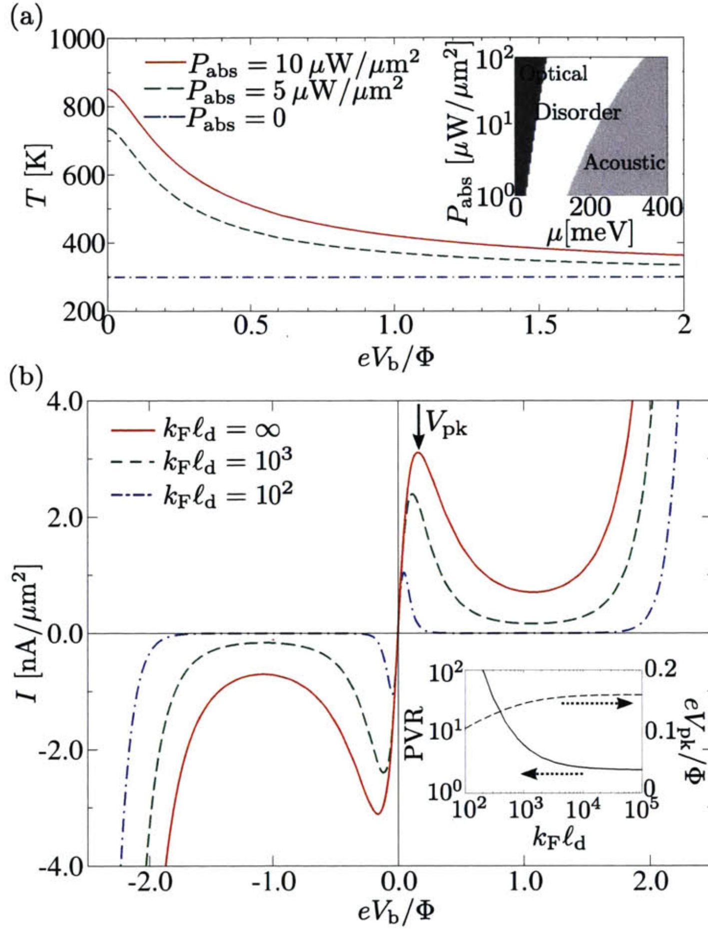

Figure 5-4: Photoresponse as a function of pump power and disorder. (a) The electronic temperature T is plotted as a function of bias V_b for different pump power values P_{abs}. The inset shows the dominant cooling pathways for different chemical potential and pump power values [for $T_0 = 0\,\text{K}$, $k_F\ell_d = 100$]. (b) Current I *vs.* V_b for different $k_F\ell_d$ values, and $P_{abs} = 10\,\mu\text{W}/\mu\text{m}^2$. The bias potential at which current peaks (V_{pk}) and the peak-to-valley ratio (PVR) are sensitive to the amounts of disorder (see inset). Results shown in this figure (except the inset of panel a) are obtained for the system undoped at $V_b = 0$, as in Fig.5-1.

dependent contributions P_{ac} and P_{dis} dominate over the roughly doping-independent P_{opt} [see Fig.5-4(a) inset]. In this regime, the cooling power behaves as $P_i = \gamma_i \mu^a (T^b - T_0^b)$, with $a = 4$, $b = 1$ for acoustic phonon cooling, and $a = 2$, $b = 3$ for disorder-assisted cooling (here γ_i are constants that depend on the cooling pathways). I assume, for simplicity, that a single cooling pathway dominates over other pathways. Then Eq. (5.9) yields

$$\alpha_T = (a/b)[1 - (T_0/T)^b]. \tag{5.19}$$

This gives $0 < \alpha_T < a/b$ with the low and high values corresponding to $T \approx T_0$ and $T \gg T_0$, respectively. The crossover between these values occurs at a threshold pump power $P_* \sim 0.5\,\mu\text{W}/\mu\text{m}^2$ that marks the onset of the hot-carrier regime under typical experimental conditions. I define P_* as the value for P_{abs} at typical carrier densities $n \sim 10^{12}\,\text{cm}^{-2}$, $T_0 = 300\,\text{K}$, and $k_F \ell_d = 100$ such that $(T - T_0)/T_0 = 0.1$. This yields the above P_* value. Maximum α_T values found from Eq.(5.19) are 0.6 and 4 for the P_{dis} and P_{ac} pathways, respectively.

Next, I estimate α_μ as a function of the barrier width. From Eq. (5.7), specializing to the case $n_0 = 0$, I find

$$\alpha_\mu = \frac{\Phi/2\mu}{1 + (4e^2/\epsilon_r \hbar v_F) k_F d} \sim \frac{6.5}{1 + 0.3\,d[\text{nm}]}. \tag{5.20}$$

where $k_F = \mu/\hbar v_F$. Here I have used the hBN barrier value $\Phi \sim 1.3\,\text{eV}$ and $\mu \sim 0.1\,\text{eV}$ for typical bias-induced doping. This gives limiting values $\alpha_\mu(d \ll d_*) \approx 6.5$ and $\alpha_\mu(d \gg d_*) = 0$, with the crossover value $d_* \sim 20\,\text{nm}$. From the above we see that the quantity $\alpha_{hc} = \alpha_T \cdot \alpha_\mu$ can reach values as high as $\alpha_{hc} \sim 25$.

5.9 Additional comments

While the NDR criterion $\alpha_{hc} > 1/2$ is insensitive to the cooling mechanism (so long as it is a strong function of carrier density, as discussed above), the form of the I-V dependence may reflect the cooling mechanism specifics. This is illustrated in Fig.5-4(b) for the P_{dis} mechanism. In particular, I consider the bias V_{pk} where the current peaks.

From Eq. (5.17) I estimate $eV_{\rm pk} \approx x_* k_{\rm B} T$. When the $P_{\rm dis}$ mechanism dominates ($k_{\rm F}\ell_{\rm d} < 10^3$) and $T \gg T_0$, a power-law relation is obtained: $V_{\rm pk} \propto \left[k_{\rm F}\ell_{\rm d}\, P/\mu^2\right]^{1/3}$. Similar arguments lead to a disorder-controlled peak-to-valley ratio (PVR). This behavior is illustrated in Fig.5-4(b) inset.

I note that the NDR features may be somewhat smeared out by statistical fluctuations induced by disorder or inhomogeneities. However, I do not expect these effects to destroy NDR. Indeed, optical heating occurs in μm-wide areas and a typical carrier density is $10^{12}\,{\rm cm}^{-2}$. At the same time, charge inhomogeneity lengthscales in graphene/hBN are a few tens of nm, whereas typical density fluctuations are as low as $\sim 10^{11}\,{\rm cm}^{-2}$ [41, 90].

5.10 Chapter summary

To summarize, vertically-stacked graphene heterostructures afford a platform to realize and explore a range of interesting optoelectronic phenomena due to photogenerated hot carriers. One such phenomenon is the light-induced NDR effect discussed above, manifesting itself through the I-V dependence, acquiring an N-shaped character under optical pumping. Vertical heterostructures use the full graphene area as a photoactive region, and possess a large degree of tunability. These properties make the NDR effect potentially useful for designing new types of optical switches and photodetectors. Our estimates show that the NDR regime, facilitated by graphene's unique optical and thermal properties, can be readily accessed in wide-barrier heterostructures.

Chapter 6

Thermionic-dominated photoresponse in graphene Schottky junctions

Vertical heterostructures of van der Waals materials enable new pathways to tune charge and energy transport characteristics in nanoscale systems. In this chapter,[1] I show that graphene Schottky junctions can host a special kind of photoresponse which is characterized by strongly coupled heat and charge flows that run vertically out of the graphene plane. This regime is accessed when vertical energy transport mediated by thermionic emission of hot carriers overwhelms electron-lattice cooling as well as lateral diffusive energy transport. As such, the power pumped into the system is efficiently harvested across the entire graphene active area via thermionic emission of hot carriers into a semiconductor material. I will also discuss the main experimental signatures of this regime, which include a large and tunable internal responsivity $\mathcal{R}$ with a non-monotonic temperature dependence. In particular, $\mathcal{R}$ peaks at electronic temperatures on the order of the Schottky potential Φ and has a large upper limit $\mathcal{R} \leq e/\Phi$ ($e/\Phi = 10\,\mathrm{A/W}$ when $\Phi = 100\,\mathrm{meV}$). As such, this proposal unveils a completely new paradigm for sensitive photodetectors, surpassing

[1]Reproduced with permission from *Nano Letters*, submitted for publication. Unpublished work copyright 2016 by the American Chemical Society.

ideal internal responsivities of photodetectors based on conventional transport, e.g. the photovoltaic effect.

6.1 Electronic and optical properties of graphene Schottky junctions

Vertical heterostructures comprising layers of van der Waals (vdW) materials have recently emerged as a platform for designer electronic interfaces [53]. Of special interest are heterostructures which feature tunable interlayer transport characteristics, as exemplified by g/X Schottky junctions [15, 16, 54–60]; here 'g' denotes graphene, and X is a semiconductor material, such as Si, MoS_2 or WSe_2. These junctions are characterized by Schottky barriers Φ that span two orders of magnitude $\Phi \approx 0.01 - 1\,\mathrm{eV}$ [15, 54, 55, 59] and exhibit in situ control by using gate potentials. The relatively small Φ achievable across the g/X interface, combined with the unique graphene photoresponse mediated by long-lived hot carriers (elevated electronic temperatures, T, different from those of the lattice, T_0 [47, 48, 51, 52, 91, 92]), make graphene Schottky junctions a prime target for accessing novel vertical energy transport regimes.

Here I show that specially designed graphene Schottky junctions can host an enhanced thermionic-dominated photoresponse driven by strongly coupled charge and energy currents. Such a photoresponse proceeds, as illustrated in Fig. 6-1(a), via the thermionic emission of graphene hot carriers with energy larger than the Schottky barrier. At steady state, an equal number of cold carriers are injected at the Fermi surface through an ohmic contact, giving a net flow of heat I_Q out of the graphene electronic system balancing the energy pumped into the system.

Strikingly, thermionic emission yields strong heat transport running vertically out of the hot electron system, which dominates over more conventional electronic cooling channels, e.g. electron-lattice cooling. Indeed, I find that I_Q can be significant in graphene [(see Fig. 6-1(c)] when $k_{\mathrm{B}}T \approx \Phi/2$, and dominates over acoustic and optical

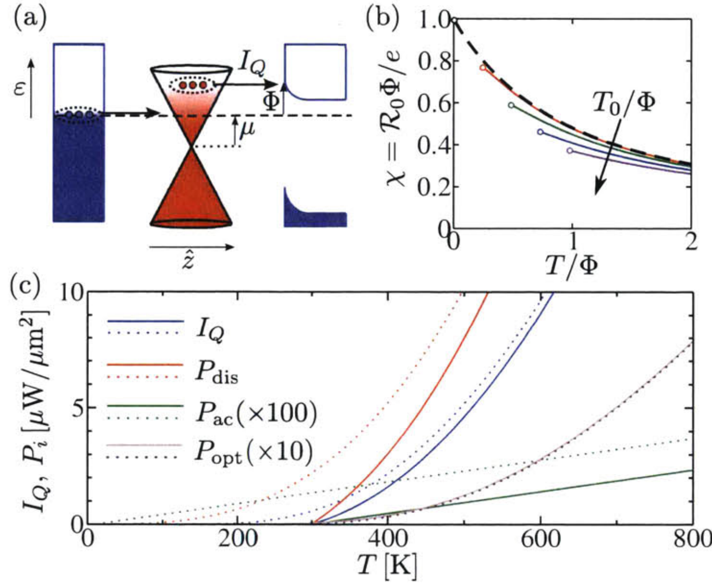

Figure 6-1: Thermionic-dominated heat transport in a graphene Schottky junction. (a) Schematic of the thermionic-dominated regime: hot carriers with energies ε close to the Schottky barrier height Φ are thermionically emitted into a semiconductor material in the out-of-plane direction $\hat{z}$, while cold carriers are injected through an Ohmic contact at the Fermi level, μ, generating a net vertical heat current I_Q. (b) Normalized ideal responsivity, $\chi = \mathcal{R}_0\Phi/e$, is shown as a function of normalized graphene electronic temperature, $k_{\text{B}}T/\Phi$, with e the electron charge [see Eq.(6.1)]. Curves are obtained for normalized ambient temperature $k_{\text{B}}T_0/\Phi = 0, 0.25, 0.5, 0.75, 1.0$, indicated with different colors for increasing T_0; characteristic $\mathcal{R}_0 \approx e/\Phi \sim 10\,\text{A/W}$ can be large (for $\Phi = 100\,\text{meV}$, see text). (c) Thermionic cooling channel, I_Q, compared with acoustic phonon cooling (clean case), P_{ac}, disorder-assisted cooling, P_{dis}, and optical phonon cooling P_{opt} [see text and Eq.(6.9)], shown for ambient temperature $T_0 = 300\,\text{K}$ (solid lines) and $T_0 = 0$ (dotted lines). Note that I_Q overwhelms P_{ac} and P_{opt}(clean case) and is competitive with P_{dis} (dirty case). Parameter values used: $\mu = \Phi = 100\,\text{meV}$, $k_{\text{F}}\ell_{\text{d}} = 50$, and $G_0 = 10\,\text{mS}/\mu\text{m}^2$, see Eqs. (6.5) and (6.9).

phonon cooling [47,48] in pristine graphene Schottky junctions; I_Q also overwhelms in-plane (lateral) diffusive energy transport. I find that the values of I_Q are competitive with disorder-assisted cooling [52, 91, 92] in more dirty devices.

Graphene is essential to the observation of these effects due to a unique combination of electronic characteristics. First, fast intraband Auger-type scattering [93, 94] allows the absorbed photon energy flux, P_{in}, to be efficiently captured as heat by ambient carriers in graphene; this process results in a thermalized hot carrier distribution [93, 94]. Second, graphene is characterized by slow electron-lattice cooling mechanisms [47, 48, 51, 52, 91, 92] which enables $T > T_0$ to drive a strong thermionic current. This is due to the large optical phonon energy in graphene [47, 48] as well as the weak electron-acoustic phonon coupling [for a detailed comparison between cooling rates, see Eq.(6.9) below]. Third, the gate-tunable work function allows an experimentally accessible way to optimize device operation, predicted to occur at $k_B T \approx \Phi/2$, for a range of technologically achievable temperatures and barrier materials. Indeed, whereas other Schottky junctions (e.g. Au/Si, Ag/Si) may also display vertical energy currents, their large Schottky barriers ($\Phi \approx 1\,\text{eV}$) and fast electron-lattice cooling render the thermionic-dominated regime impractical for these systems.

An important optoelectronic figure of merit is the conversion between the absorbed photon energy flux, P_{abs}, and the detected photocurrent, I_e, encoded in the (internal) responsivity $\mathcal{R} = I_e/P_{\text{abs}}$. Importantly, our model yields a large upper limit for $\mathcal{R}$. Indeed, energy Φ is transported per carrier extracted across the g/X junction [Fig. 6-1(a)] yielding a limiting internal responsivity $\mathcal{R}_0$, occurring in the thermionic-dominated regime (i.e., $I_Q = P_{\text{abs}}$) given by

$$\mathcal{R} \leq \mathcal{R}_0, \qquad \mathcal{R}_0 = \frac{e}{\Phi} \times \chi(\tilde{T}, \tilde{T}_0). \tag{6.1}$$

Here e is the electron charge, $\tilde{T}$ and $\tilde{T}_0$ are the dimensionless graphene and ambient temperatures (temperature of the lattice and semiconductor), respectively, and χ is a dimensionless function (see text below) plotted in Fig. 6-1(b). The function χ can take values close to unity, allowing $\mathcal{R}_0$ to be on the order of $e/\Phi = 10\,\text{A/W}$, for

$\Phi = 100\,\mathrm{meV}$. For a discussion of net values of $\mathcal{R}$ in Eq.(6.1), see Fig.6-2(c).

Since the incident photon energy $\hbar\omega$ (e.g. in the visible) can be many multiples of Φ, I anticipate that g/X Schottky photodetectors can provide significant gains in the internal responsivity compared to those in conventional (photovoltaic-based) photodetectors, which are limited by $\mathcal{R}^{\mathrm{PV}} \leq e/\hbar\omega$ [95]. In particular, the ultra-fast electron energy relaxation times in graphene yield *multiple* hot carriers per absorbed photon [93, 94], in stark contrast to photovoltaic-based schemes that yield a single electron-hole pair per absorbed photon. Naturally, the external responsivity of the device is also affected by the absorption coefficient of the photoactive material. Whereas the absorption coefficient of 2.3% per layer in graphene [85] is small compared, for instance, to typical values of 10-50% in Si [96], this small value can be increased using optical waveguides [56] and plasmon enhanced absoption [97]. These external enhancement mechanisms will not be discussed here.

In addition, g/X photodetectors also enable a boosted photoresponse compared to previous photothermoelectric-based schemes [51]. Indeed, the vertical structure allows researchers to circumvent lateral electronic heat diffusion, which drastically reduces the operating electronic temperatures and efficiencies in photothermoelectric-based schemes.

Another important feature of the g/X photoresponse is the possibility of using the temperature dependence of $\mathcal{R}$ as a diagnostic of thermionic-dominated photoresponse. After including losses to the lattice via disorder-assisted cooling, $\mathcal{R}$ is found to be non-monotonic, peaking at an optimal operating hot carrier temperature $k_{\mathrm{B}}T \approx \Phi/2$ [Fig. 6-2(c)]. Since T can be controlled by the incident light power and Φ via gate voltage, non-monotonic $\mathcal{R}$ as a function of T provides an easily accessible experimental signature of the strongly coupled charge and energy thermionic transport that is engineered across the g/X interface. Indeed, non-monotonic temperature behavior does not occur in typical photovoltaic-based devices, where responsivity is mainly independent of pump power or photon intensity.

6.2 Vertical photocurrent model

I begin by modeling vertical transport across the g/X device, as depicted in Fig. 6-1(a). Using the standard approach for modeling vertical graphene tunneling devices [98], wherein energy is conserved but in-plane momentum is not, I write the electron and heat current across the g/X Schottky junction as

$$\begin{bmatrix} I_e \\ I_Q \end{bmatrix} = \int_{-\infty}^{\infty} d\varepsilon \begin{bmatrix} e \\ \varepsilon \end{bmatrix} G(\varepsilon) \left[f\left(\varepsilon/k_{\mathrm{B}}T\right) - f\left(\varepsilon/k_{\mathrm{B}}T_0\right) \right], \tag{6.2}$$

where

$$G(\varepsilon) = \frac{2\pi e^2}{\hbar} D(\varepsilon) D_{\mathrm{c}}(\varepsilon) |\mathrm{T}(\varepsilon)|^2. \tag{6.3}$$

Here $G(\varepsilon)$ is a parameter with units of electrical conductance which characterizes the Schottky interface (see discussion below), D (D_{c}) is the density of states of graphene (the conduction band of the semiconductor), $f(x) = 1/(e^x + 1)$ is the Fermi distribution function, $\mathrm{T}(\varepsilon)$ is the energy-dependent tunneling transition matrix element between graphene and the semiconductor electronic states, and energies ε are referenced from the Fermi energy μ [see Fig. 6-1(a)]. The function $\mathrm{T}(\varepsilon)$ contains all the microscopic information about the relevant mechanisms that couple graphene with material X, such as phonons or hot-spots formed by defects.

Two important assumptions are present in Eq.(6.2). First, I neglected hole transport between graphene and the valence band of X assuming that the barrier height for hole transport is much larger than the corresponding one for electron transport. Secondly, I assume that the Fermi level and the temperature in graphene and in X are spatially fixed. In a more realistic scenario, the pumping power may cause the temperature and Fermi level to spatially vary in the out-of plane direction. In this case, both quantities need to be determined self-consistently by appropriate balance equations. However, these do not introduce any new qualitative features to our simplified model.

When light heats graphene electrons so that $T > T_0$, then Eq.(6.2) describes the short-circuit charge current (photocurrent) and the energy current flow, shown

schematically in Fig. 6-1(c). At steady state, T is determined by energy balance of the incident absorbed power in graphene, $P_{\rm in}$, and the energy being dissipated by the graphene electronic system that includes both the thermionic channel, I_Q, and other dissipative channels, $P_{\rm loss}$ (e.g. electron-lattice cooling, and diffusive heat transport, as discussed below). Explicitly, I have

$$P_{\rm abs} = I_Q(T, T_0) + P_{\rm loss}(T, T_0), \tag{6.4}$$

where I have fixed T_0 to the temperature of the ambient environment, i.e. there is no backflow of hot electrons into graphene. The latter assumption results from the large heat capacity and fast electron-lattice cooling in highly doped semiconductors such as Si [99]. In what follows, I shall analyze the energy/charge characteristics of g/X Schottky junctions as a function of T and T_0; naturally the T values displayed can be attained via a suitably chosen $P_{\rm in}$.

The depletion width, for example in g/Si interfaces [58], can be many times larger than the electron wavelength. As a result, only electrons with energies above the effective barrier Φ formed at the g/X interface contribute to the current; in this way, the photocurrent is thermally activated. Here I adopt a phenomenological approach to capture the essential physics independent of the microscopic details of the device. To this end, I approximate $G(\varepsilon) = G_0\Theta(\varepsilon - \Phi)$ in Eq.(6.2), with Θ the step-function, in order to aggregate the microscopics of the junction into a single variable that can be easily measured in experiment. I emphasize that this approximation does not affect the qualitative behavior of I_e, I_Q or χ for the range of temperatures of interest, $k_{\rm B}T \lesssim \Phi$; further, this approximation represents a conservative estimate of the particle current, since $G(\varepsilon)$ is typically a monotonically increasing function due to the larger density of states available for scattering at larger ε in graphene. As a side remark, I note that G_0 is *not* the zero-bias junction conductance; the latter is suppressed by a factor $e^{-\Phi/T}$, as discussed in the paragraph following Eq.(6.11).

Using a step-like transmission, heat and charge currents can then be expressed in

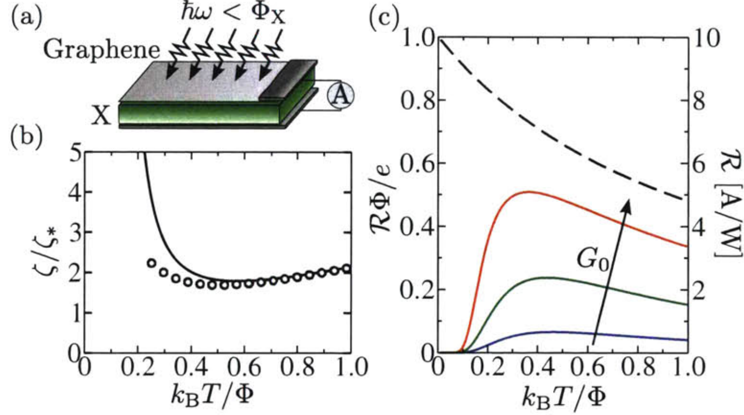

Figure 6-2: Graphene/X Schottky junction photoresponse. (a) Schematic of the hot carrier photodetector, where X respresents a semiconductor material with bandgap Δ_X. Here I consider graphene as the photoactive material for absorption, i.e. photon energy $\hbar\omega < \Delta_X$. (b) Ratio $\zeta = P_{\rm loss}/I_Q$ modeled via Eq.(6.11) as a function of T, with $T_0 = 0$ (solid line) and $T_0 = 300\,{\rm K}$ (empty circles). Note that the latter has a smaller range, $T \geq T_0$. (c) The responsivity $\mathcal{R}$ (solid lines) for the g/X junction exhibits a non-monotonic electronic temperature dependence peaking at $T \approx \Phi/2k_B$, shown for ζ modeled in Eq.(6.11) [panel (b)] with $\zeta_* = 5, 1, 0.2$ (blue, green, red, respectively); dimensionless $\mathcal{R}$ is shown on the left vertical axis. The dashed line indicates an ideal case $\mathcal{R} = \mathcal{R}_0$. Here I used values $G_0 = 2, 10, 50\,{\rm mS}/\mu{\rm m}^2$, $\mu = \Phi = 100\,{\rm meV}$ and $k_F\ell_d = 50$ yielding sizable $\mathcal{R}$ (right vertical axis).

terms of non-dimensional integrals by defining $x = \varepsilon/\Phi$ in Eq.(6.2), yielding

$$I_e = \frac{G_0\Phi}{e}\int_1^\infty dx\,\Delta f(x)\,, \quad I_Q = \frac{G_0\Phi^2}{e^2}\int_1^\infty dx\,x\,\Delta f(x), \tag{6.5}$$

where $\Delta f(x) = f(x/\tilde{T}) - f(x/\tilde{T}_0)$. It is straight-forward to show that the integrals on the right-hand side of Eq.(6.5) are related to the well-known complete Fermi integrals,

$$F_k(\xi) = \int_0^\infty dx\,\frac{x^k}{e^{x-\xi}+1}, \tag{6.6}$$

via $\int_1^\infty dx x^n f(x/\tilde{T}) = \sum_{k=0}^n \binom{n}{k}\tilde{T}^{k+1}F_k(-1/\tilde{T})$. In the low temperature regime, $\tilde{T} \ll 1$, the value of F_k behaves as $F_k(-1/\tilde{T}) \approx \Gamma(k+1)e^{-1/\tilde{T}}$, with Γ the Gamma function. In the high temperature regime, $\tilde{T} \gg 1$, F_k takes values $F_0(-1/\tilde{T}) \approx \ln(2)$ and $F_1(-1/\tilde{T}) \approx \pi^2/12$.

6.3 Photoresponse in the ideal limit

A key feature of thermionic-dominated [$P_{\rm loss} = 0$] transport is the strong charge-energy current coupling manifested in $\mathcal{R}_0$. Using Eq.(6.5) above, I obtain Eq.(6.1) with χ given by

$$\chi(\tilde{T}, \tilde{T}_0) = \frac{\int_1^\infty dx \Delta f(x)}{\int_1^\infty dx x \Delta f(x)}. \tag{6.7}$$

The general behavior of $\chi(\tilde{T}, \tilde{T}_0)$ can be most easily understood by first setting $T_0 = 0$. In this case, χ in Eq.(6.1) adopts the simple form

$$\chi_0(\tilde{T}) \equiv \chi(\tilde{T}, \tilde{T}_0 = 0) = \left[1 + \tilde{T}\frac{F_1(-1/\tilde{T})}{F_0(-1/\tilde{T})}\right]^{-1}. \tag{6.8}$$

Importantly, χ_0 is a decreasing function of temperature $\tilde{T}$, as shown in the black dashed curve of Fig. 6-1(b). In particular, for $\tilde{T} \ll 1$, χ_0 takes values $\chi_0 \sim (1 + \tilde{T})^{-1}$ of order unity, and for $\tilde{T} \gg 1$, χ_0 decreases with inverse temperature as $\chi_0 \approx 12\log(2)/(\pi^2\tilde{T})$ [see Fig. 6-1(b)]. This latter fact means that, although $\mathcal{R}_0$ is expressed in units of e/Φ in Eq.(6.1), $\mathcal{R}_0$ cannot grow indefinitely by making Φ smaller; $\mathcal{R}_0$ reaches a saturating value $\mathcal{R}_0 \approx 12\log(2)e/(\pi^2 k_{\rm B}T)$ for $k_{\rm B}T \gg \Phi$, as shown in Fig. 6-1(c).

For finite values of T_0, the qualitative behavior of χ does not depart significantly from that of χ_0. As shown in Fig. 6-1(b), where $\chi(\tilde{T}, \tilde{T}_0)$ is obtained by numerical integration of Eq.(6.7) for different values of $\tilde{T}_0$, the function χ largely follows the χ_0 curve and only shifts slightly from χ_0 with increasing $\tilde{T}_0$. Further, the range of operating hot electron temperatures is now smaller, $\tilde{T} \geq \tilde{T}_0$, as illustrated in Fig. 6-1(b) by curves that now start at $\tilde{T} = \tilde{T}_0$. Although χ is finite at $\tilde{T} = \tilde{T}_0$, there is no net current at equal temperatures [as indicated by the empty circles at the beginning of the curves in Fig. 6-1(b)]; a non-vanishing χ at $\tilde{T} = \tilde{T}_0$ arises from the differential ratio that characterizes the responsivity $\mathcal{R}$.

6.4 Photoresponse in real systems

Considering losses, Eq.(6.5) yields I_Q that can be sizable [see blue curves in Fig. 6-1(c)]. In plotting Fig. 6-1(c), I numerically integrated Eq.(6.5) and used $\Phi = 100\,\text{meV}$ and $G_0 = 10\,\text{mS}/\mu\text{m}^2$ (see below for G_0 estimates). Further, I_Q compares favorably with intrinsic electron-lattice cooling in graphene: (i) single-acoustic phonon cooling for pristine graphene P_{ac} (green curves), (ii) optical phonon cooling P_{opt} (magenta curves), and (iii) disorder-assisted cooling P_{dis} (red curves), where I consider the degenerate limit ($\mu \gg T$) for all cases [47, 48, 52]:

$$P_{\text{ac}} = P_{\text{ac}}(T - T_0), \quad P_{\text{dis}} = \gamma_{\text{dis}}(T^3 - T_0^3),$$
$$P_{\text{opt}} = \gamma_{\text{opt}}\left[f_{\text{B}}(\hbar\omega_0/k_{\text{B}}T) - f_{\text{B}}(\hbar\omega_0/k_{\text{B}}T_0)\right]. \tag{6.9}$$

The prefactors, which were defined in Sec. 2.4.2, are $\gamma_{\text{ac}} = \hbar U_D^2 \mu^4 k_{\text{B}}/8\pi\rho(\hbar v_{\text{F}})^6$, $\gamma_{\text{dis}} = 2U_D^2\mu^2 k_{\text{B}}^3/\rho c_{\text{s}}^2 \hbar(\hbar v_{\text{F}})^4 k_{\text{F}}\ell_{\text{d}}$ and $\gamma_{\text{opt}} = \hbar^2\omega_0^3/24\pi\rho a_0^4 v_{\text{F}}^2$, with U_D the deformation potential, ρ the graphene mass density, $k_{\text{F}}\ell_{\text{d}}$ the dimensionless disorder parameter, a_0 the carbon-carbon distance, ω_0 the optical phonon frequency, and $N(x)$ the Bose distribution. For the cooling mechanisms, I used $\mu = 100\,\text{meV}$, $U_D = 20\,\text{eV}$, $\rho = 7.6 \cdot 10^{-7}\,\text{kg/m}^2$, $k_{\text{F}}\ell_{\text{d}} = 50$, $a_0 = 1.4\,\text{Å}$ and $\hbar\omega_0 = 0.2\,\text{eV}$. Indeed, I_Q overwhelms both P_{ac} and P_{opt}, and is competitive with P_{dis}, as shown in Fig. 6-1(c).

The hot carrier thermionic cooling channel, I_Q, and the strong charge-energy current coupling it produces [Eq.(6.1)], can manifest itself in large and non-monotonic responsivities in g/X photodetectors [Fig. 6-2(a)]. Accounting for energy balance in Eq.(6.4) I find a net responsivity given by

$$\mathcal{R} = \frac{\mathcal{R}_0}{1+\zeta}, \quad \zeta = \frac{P_{\text{loss}}}{I_Q}, \tag{6.10}$$

where ζ quantifies losses. To estimate ζ for actual devices, I consider the disorder-assisted cooling power in graphene [52], $P_{\text{loss}} \approx P_{\text{dis}} = \gamma_{\text{dis}}(T^3 - T_0^3)$ as an illustrative

example, see Eq.(6.9). Adopting the same procedure as described above, then

$$\zeta(\tilde{T}, \tilde{T}_0) = \zeta_* \times \frac{\tilde{T}^3 - \tilde{T}_0^3}{\int_1^\infty dx x \Delta f}\ , \ \zeta_* = \frac{e^2 \gamma_{\rm dis} \Phi}{G_0}, \tag{6.11}$$

is obtained, where the characteristic ζ is set by $e^2\gamma_{\rm dis}\Phi/G_0$. As expected, increasing the prefactor $\gamma_{\rm dis}$, for $P_{\rm dis}$, increases the losses to phonon scattering embodied in ζ. Alternatively, increasing the conductance across the g/X interface enhances the thermionic channel.

In calculating $\mathcal{R}$ in Eq.(6.10), I use the same parameter values as in Fig. 6-1: $\mu = \Phi = 100\,\text{meV}$ and $k_{\rm F}\ell_{\rm d} = 50$. The value of G_0 can be estimated from conductance measured in the dark state, $G_{\rm D}$, obtained in actual g/X devices at equilibrium $T = T_0$ (for example g/Si Schottky junctions in Refs. [54, 55]). Indeed, under an infinitesimally small potential bias $\delta V_{\rm b}$, I can approximate Δf in Eq.(6.7) as $\Delta f(x) = [e^x/(e^x + 1)^2] \times e\delta V_{\rm b}/T_0$ due to the small chemical potential difference $e\delta V_{\rm b}$ between G and X. Integrating over x in Eq.(6.7), I obtain $G_{\rm D} = G_0/(1 + e^{\Phi/T_0})$. In a typical scenario $k_{\rm B}T_0 \ll \Phi$, the conductance in the dark state is exponentially suppressed with increasing temperature as $G_{\rm D} \approx G_0 \exp(-\Phi/k_{\rm B}T_0)$, in agreement with the qualitative behavior observed in Refs. [15,16,54–57,59]. To give an estimate of the range of conductances achievable in g/X devices, $G_{\rm D}$ in these experiments report $G_{\rm D} \sim 0.1 -$ several $\times\ \mu\text{S}/\mu\text{m}^2$ for $\Phi_{\rm Si} \sim 0.3\,\text{eV}$ with T_0 at room temperature. This gives G_0 in the $1 - 100\,\text{mS}/\mu\text{m}^2$ ballpark [for $\mathcal{R}$ in Fig. 6-2(c), I used $G_0 = 2, 10, 50\,\text{mS}/\mu\text{m}^2$, which correspond to $\zeta_* = 5, 1, 0.2$, see Eq.(6.11)].

As shown in Fig. 6-2(b), ζ exhibits a clear non-monotonic dependence on T characterized by two regimes: (i) small $\tilde{T} \ll 1$, I_Q is exponentially suppressed by the transport barrier Φ, and thus $P_{\rm dis}$ dominates, (ii) large $\tilde{T} \gg 1$, I find that I_Q scales as T^2, and rises less steeply than the T^3 power law of supercollision cooling. Hence, there is a "sweet spot" for observing a competitive thermionic channel I_Q. The optimal value occurs for temperatures $k_{\rm B}T/\Phi \approx 0.5$ [see Fig. 6-2(b)], with minimum $\zeta_{\rm min} \approx 1.85 \times \zeta_*$. This can be estimated from Eq.(6.11) in the limit $\tilde{T} \ll 1$ and $T_0 = 0$, where the above-mentioned optimal values are obtained from minimization

of the equation $\zeta/\zeta_* \approx \tilde{T}^2 e^{1/\tilde{T}}$ [Fig. 6-2(b)].

The responsivity $\mathcal{R}$ in Eq.(6.10) mirrors ζ to display a non-monotonic dependence on T, peaking at a temperature $k_B T \approx \Phi/2$, as shown in Fig. 6-2(c). Peak responsivities in the range $\mathcal{R} \approx 1 - 10\,\mathrm{A/W}$ are obtained within our model. Indeed, for large $G_0 = 50\,\mathrm{mS}/\mu\mathrm{m}^2$ (corresponding to $\zeta_* = 0.2$), $\mathcal{R}$ starts to approach the ideal case, $\mathcal{R} = \mathcal{R}_0$ (dashed black line). The non-monotonic dependence of $\mathcal{R}$ as a function of T provides a clear fingerprint of the competition between thermionic energy transport and conventional electron-phonon cooling. Since the Schottky barrier heights can be tuned by the applied gate voltage, the peak temperature $k_B T \approx \Phi/2$ is gate tunable. Further, the scaling of Φ and the device conductance G_0 also provides experimental knobs with which to adjust the responsivity of the device.

Naturally, there are other mechanisms for losses that affect the responsivity. For instance, lateral (in-plane) heat currents, $I_Q^{\parallel} = -\nabla \cdot (\kappa_{\parallel} \nabla T)$, can transport heat towards the contacts in small devices. To estimate this effect, I use the Wiedemann-Franz relation, $\kappa_{\parallel}(T) = (\pi^2/3e^2) \times k_B^2 T \sigma$, where σ is the in-plane electrical conductivity of graphene. For the relevant regime of moderate to high temperatures, $T \gtrsim \Phi$, I can approximate $I_Q \approx G_0 k_B^2 T^2/e^2 = \gamma(T) \times T$ [cf. Eq.(6.2)]. As a result, I find a cooling length $\xi_{\parallel} = \sqrt{\kappa(T)/\gamma(T)}$ coming from the thermionic channel that is independent of T. Using a uniform in-plane $\sigma \sim 1\,\mathrm{mS}$ [100] results in $\xi_{\parallel} \approx 0.6\,\mu\mathrm{m}$, so that vertical energy extraction dominates over in-plane thermal conduction for sufficiently large devices with size $L > \xi_{\parallel}$.

I note that interactions with the substrate can result in cooling via surface optical phonons. These losses will vary for different substrate (X) choices and are only significant when X is a polar material [101]. Importantly, I do not expect them to be relevant in non-polar materials, e.g. X = silicon.

6.5 Important features of g/X photodetectors

The optimal responsivity ocurring at $k_B T \approx \Phi/2$ is an important characteristic for the design of graphene photodetectors. Indeed, given that $T < 2000\,\mathrm{K}$ in realis-

tic situations, Schottky barriers in the 100 meV ballpark allow operation of the g/X photodetector near optimal responsivities (i.e. near minimum ζ). As a result, photodetector fabrication should be targeted at van der Waals materials with relatively small work function difference with respect to graphene, for instance WS_2 [59].

Although g/X photodetectors allow in situ control of Φ by electrostatic doping, it is important to note that several parameters of the model vary implicitly with Φ. On the one hand, changes in Φ also induce changes in graphene doping, thus modifying the electronic cooling power. Further, when Φ becomes smaller than the incoming photon energies, photo-emission of primary carriers over the barrier competes with thermalization by electron-electron interactions. In this case, a smaller amount of the incident power is captured in the hot-carrier distribution.

Lastly, it is interesting to note that g/X photodetectors can also operate at low photon energies, $\hbar\omega \leq 2\mu$. In this regime, conventional Drude absorption from ambient carriers directly captures incident radiation. This contrasts with conventional semiconductor photodetectors, that do not absorb light below the semiconductor bandgap. A tantalizing possibility is to use g/X Schottky junctions within the mid IR - THz bandwidth where presently-available technologies offer lackluster performance [102, 103].

6.6 Chapter summary

Graphene Schottky junctions host tunable interfaces across which energy transport can be engineered, exemplified by thermionic-dominated transport regime wherein energy and charge currents are strongly coupled. Fingerprints of the thermionic-dominated regime include high responsivities on the order of $\mathcal{R} \sim 1-10$ A/W, and a non-monotonic dependence of $\mathcal{R}$ on electron temperature (or pump power) in g/X photodetectors. The large degree of in situ tunability allows optimization of the g/X interface for different applications and irradiation conditions; vertical hot carrier convection opens up new vistas to efficiently harvest photon energies over a wide spectral range, utilizing the entire exposed graphene area as a photoactive region.

Part II

Electron-optics behavior in graphene quantum dots

Chapter 7

Graphene quantum dots

The design of high-finesse resonant cavities for electronic waves faces challenges due to short electron coherence lengths in solids. In this chapter, I present a novel approach inspired by the peculiar acoustic phenomena in whispering galleries to confine electronic states.[1] Taking advantage of graphene's gate-tunable light-like carriers, whispering-gallery mode (WGM) resonators are realized inside circular *pn* junctions. The theory of graphene quantum dots described in this chapter was experimentally demonstrated at NIST as a result of a collaborative work [104]. In their experimental setup, a circular cavity is obtained and probed by the action of a scanning tunneling microscope (STM) tip. This approach complements previous approaches to confine electronic waves by carefully positioned adatoms at clean metallic surfaces, i.e. quantum corrals [105]. Contrary to quantum corrals, graphene quantum dots enable in situ tunability of the resonator size and the carrier concentration under the probe in a back-gated graphene device over a wide range of sizes. The WGM-type confinement and associated resonances, which will be described in detail below, are a new addition to the quantum electron-optics toolbox.

[1]This chapter is reproduced in part from Y. Zhao, *et al.*, Creating and probing electron whispering-gallery modes in graphene, *Science* **348**, 672 Copyright 2015 by the American Association for the Advancement of Science (AAAS).

7.1 Whispering gallery modes in graphene

Charge carriers in graphene exhibit light-like dispersion resembling that of electromagnetic waves. Similar to photons, electrons in graphene nanostructures propagate ballistically over micrometer distances, with the ballistic regime persisting up to room temperatures [8]. This makes graphene an appealing platform for developing quantum electron optics, which aims at controlling electron waves in a fully coherent fashion. In particular, gate-tunable heterojunctions in graphene can be exploited to manipulate electron refraction and transmission in the same way that optical interfaces in mirrors and lenses are used to manipulate light [37]. These properties have stimulated ideas in optics-inspired graphene electronics. First came Fabry-Pérot interferometers [101], which have been fabricated in planar *npn* heterostructures in single-layer graphene [106] and subsequently in bilayer [107] and trilayer graphene [108]. The sharpness of the *pn* junctions achievable in graphene can enable precise focusing of electronic rays across the junction, allowing for electronic lensing and hyperlensing [39, 109, 110].

In this chapter, I consider electron whispering-gallery mode (WGM) resonators, an addition to the electron-optics toolbox. The WGM resonances are familiar for classical wave fields confined in an enclosed geometry — as happens, famously, in the whispering gallery of St. Paul's Cathedral in London. The WGM resonators for electromagnetic fields are widely used in a vast array of applications requiring high-finesse optical cavities [111–113]. Optical WGM resonators do not depend on movable mirrors and thus lend themselves well to designs with a high quality factor. This can render the WGM design advantageous over the Fabry-Pérot design, despite challenges in achieving tunability due to their monolithic (single-piece) character (see [111] for a mechanically tunable optical WGM resonator). The system under study is free from these limitations, representing a fully tunable WGM resonator in which the cavity radius can be varied over a wide range by adjusting gate potentials. In contrast, the best electronic resonators known to date — the nanometer-sized quantum corrals designed by carefully positioning adatoms atop a clean metallic surface [105] — are

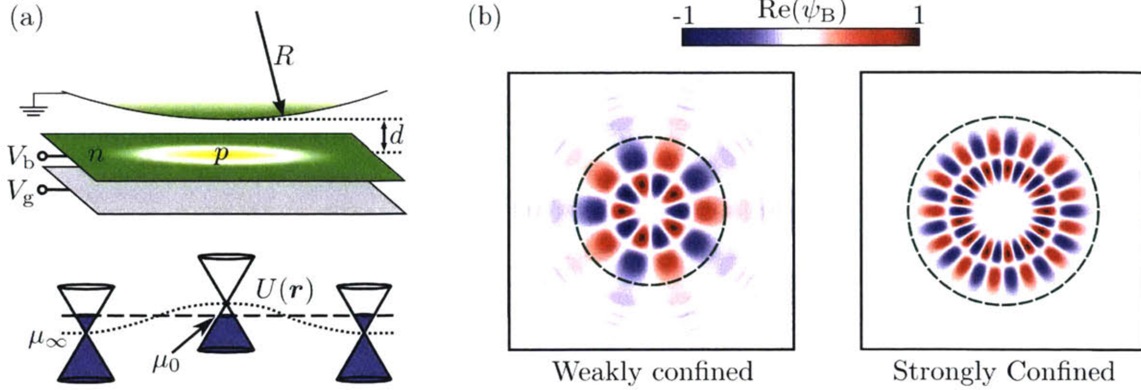

Figure 7-1: Confined electronic states in microscopic electron cavities defined by pn junction rings in graphene. (a) The rings are induced by the STM tip voltage bias (V_b) and back-gate voltage (V_g), adjusted so as to reverse the carrier polarity beneath the tip relative to the ambient polarity. The pn junction acts as a sharp boundary giving rise to Klein scattering of electronic waves, producing mode confinement via the whispering-gallery mechanism. The cavity radius and the local carrier density are independently tunable by the voltages V_b and V_g. Electron resonances are mapped out by the STM spectroscopy measurements (see Fig.7-2). Shown are the STM tip potential $U(\boldsymbol{r})$ and the quantities discussed in the text: the STM tip radius (R), its distance from graphene (d), and the local (μ_0) and ambient (μ_∞) Fermi levels with respect to the Dirac point. n and p label the electron and hole regions. (b) Spatial profile of WGM resonances. Confinement results from interference of the incident and reflected waves at the pn rings (dashed lines). The confinement is stronger for the larger angular momentum m values, corresponding to more oblique wave incidence angles. This is illustrated for $m = 9/2$ (weak confinement) and $m = 25/2$ (strong confinement). Plotted is the quantity $\mathrm{Re}(\psi_B)$, the real part of the second spinor component in Eq.(7.1).

not easily reconfigurable.

Further, although WGM resonators are ubiquitous in optics and acoustics [111–114], only a few realizations of such resonators were obtained in non-optical and non-acoustic systems. These include WGM for neutrons [115], as well as for electrons in organic molecules [116]. Here we explore a circular electron cavity created beneath a metallic tip, such as those in a scanning tunneling microscope, and we study the WGM-type confinement of electronic modes. The cavity is defined by a tip-induced circular pn junction ring, at which the reflection and refraction of electron waves are governed by Klein scattering (Fig.7-1). Klein scattering originates from the graphene linear energy dispersion relation and opposite group velocities for conduction and valence band carriers; Klein scattering at a pn junction features a strong angular dependence with a 100% probability for transmission at normal incidence, as well as

focusing properties resembling negative refractive index metamaterials [37, 39]. Although Klein scattering is characterized by perfect transmission and no reflection for normal incidence, it also gives rise to nearly perfect reflection for oblique incidence occurring in the WGM regime [37]. As illustrated in Fig.7-1(b), this yields excellent confinement and high-finesse WGM resonances for modes with high angular momentum m and a less perfect confinement for non-WGM modes with lower m values.

Electron optical effects in graphene have so far been explored using transport techniques, which lack spatial and angular resolution that would be indispensable for studying confined electronic states and/or electron lensing. The use of a scanning probe technique enables nanometer-scale spatial resolution. The STM probe has a dual purpose: (i) creating a local pn junction ring, which serves as a confining potential for electronic states, and (ii) probing the resonance states localized in this potential by electron tunneling. The planar back gate and the STM tip, acting as a circular micrometer-sized top gate, can change both the overall background carrier density and the local carrier density under the tip. As such, pn and np circular junctions centered under the probe tip [Fig.7-1(a)] can be tuned by means of the tip-sample bias $V_{\rm b}$ and the back-gate voltage $V_{\rm g}$. For the purpose of creating resonant electronic modes inside the junction, this configuration enables in situ, independent control over the carrier concentration beneath the STM tip and the pn ring radius. The tunneling spectral maps from such a device obtained at NIST, show a series of interference fringes as a function of the two knobs $(V_{\rm b}, V_{\rm g})$ (Fig.7-2). These fringes originate from resonant quasi-bound states inside the pn ring.

The measured spacing between fringes ($\Delta\varepsilon$) can be used to infer the cavity radius (r). Using the formula $\Delta\varepsilon = \pi\hbar v_{\rm F}/r$ and an estimate from Fig.7-2(a) ($\Delta\varepsilon \approx 40\,{\rm meV}$), we obtain $r \approx 50\,{\rm nm}$, a value considerably smaller than the STM tip radius ($R \approx 1\,\mu{\rm m}$). This behavior can be understood from a simple electrostatic model of a charged sphere proximal to the ground plane. When the sphere-to-plane distance d is small compared with the sphere radius R, the induced image charge density cloud $\rho(r)$ behaves as $\rho(r) \propto 1/(d + r^2/2R)$ predicting a length scale $\sqrt{2Rd} \ll R$. This crude estimate is upheld, within an order of magnitude, by a more refined electrostatic

modeling, which also gives a length scale much smaller than R (see below).

7.2 Description of the NIST experiment

The experimental results from NIST were obtained on a device consisting of a graphene layer on top of hexagonal boron nitride, stacked on SiO_2 with a doped Si back gate. Figure 7-2(a) shows a tunneling conductance map as a function of back-gate voltage (V_g) on the horizontal axis and a sample bias (V_b) on the vertical axis. A series of interference-like fringes forming a curved fan (labeled WGM′) can be seen in the upper right of Fig.7-2(a). The center of the fan defines the charge neutrality point. This point can be off $(0, 0)$ in the (V_g, V_b) plane due to impurity doping of graphene (shift along V_g) and the contact potential difference between the probe tip and graphene (shift in V_b). Another interesting feature in such conductance maps is a (somewhat less visible) second fan of fringes (labeled WGM″), which is crossing the primary WGM′ fan. The fringes in the WGM″ fan follow the typical graphene dispersion with respect to the Fermi energy, which varies with doping as $\propto \sqrt{|V_g|}$, coming from higher sample bias to lower as a function of V_g.

Figure 7-2(c) shows nine oscillations in a line cut across the WGM′ fan along the V_g axis. To understand the origin of these nine oscillations, two spectral line cuts along the V_b axis in Fig.7-2(d) are plotted. The first spectrum in Fig.7-2(d) at $V_g = 11\,\mathrm{V}$ (blue curve) contains a group of resonances (labeled 1″ to 3″) near the Fermi level ($V_b = 0$) with a spacing of $37.6 \pm 1.2\,\mathrm{mV}$. In the map in Fig.7-2(a), these resonances can be seen to move to lower energies approximately following the typical Dirac point dispersion $\propto \sqrt{|V_g|}$. Taking a vertical cut at a higher back-gate voltage of $V_g = 16\,\mathrm{V}$ (red curve) shows resonances 1″ and 2″ shifted down in energy in Fig.7-2(d). Focusing now at slightly higher energies, the WGM′ resonances appear at positive energies in Fig.7-2(d) and are labeled 1′ to 4′ for $V_g = 16\,\mathrm{V}$. The average spacing of these resonances is $116.9 \pm 7.5\,\mathrm{mV}$.

A close examination of Fig.7-2(a) indicates the one-to-one correspondence between the WGM″ resonances 1″, 2″,... and the WGM′ resonances 1′, 2′..., suggesting their

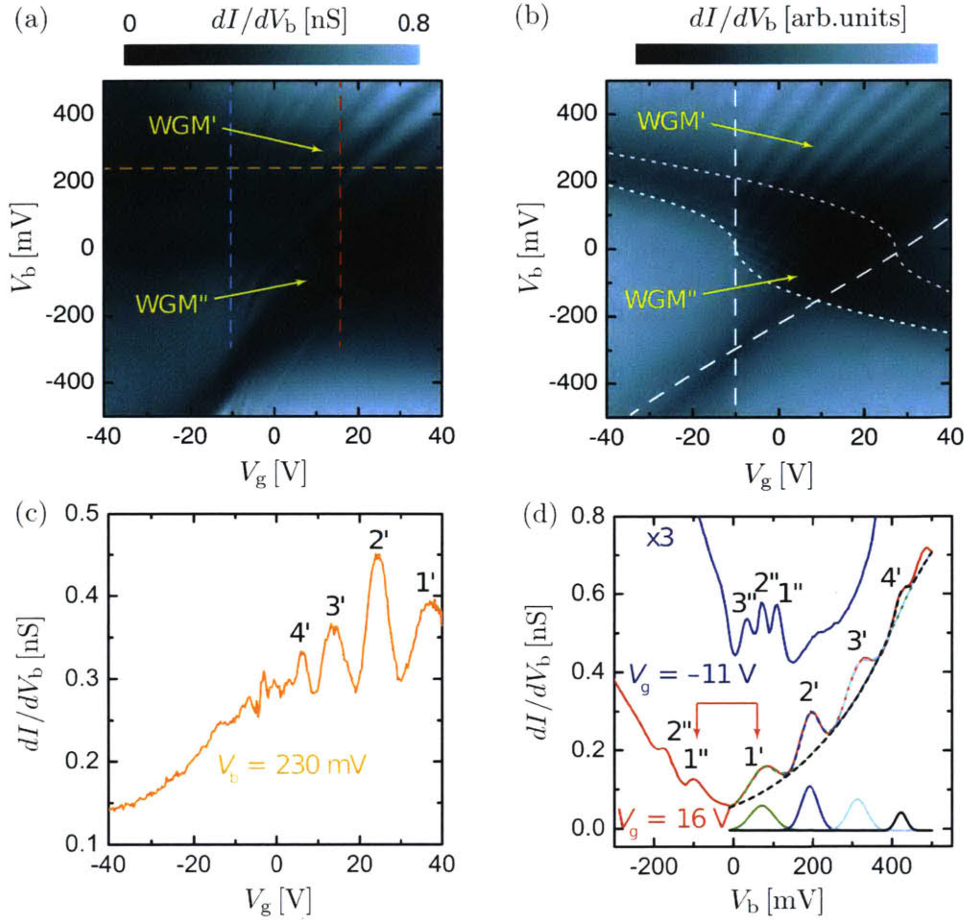

Figure 7-2: Confined electronic states probed by STM measurements from NIST. (a) Differential tunneling conductance ($dI/dV_{\rm b}$) for a single-layer graphene device, as a function of sample bias ($V_{\rm b}$) and back-gate voltage ($V_{\rm g}$). The two fans of interference features, marked WGM$'$ and WGM$''$, originate from WGM resonances in the DOS (see text). (b) Interference features in $dI/dV_{\rm b}$, calculated from the relativistic Dirac model. The features WGM$'$ and WGM$''$ in the $(V_{\rm g}, V_{\rm b})$ map originate, respectively, from the conditions $\varepsilon = \mu_0$ and $\varepsilon = \mu_0 + eV_{\rm b}$ (see text). The boundaries of the WGM$'$ (and WGM$''$) regions are marked by dashed (and dotted) white lines. (c) $dI/dV_{\rm b}$ spectra taken along the horizontal line in (a) at $V_{\rm b} = 230\,{\rm mV}$. (d) $dI/dV_{\rm b}$ spectra taken along the two vertical lines in the map in (a) at $V_{\rm g} = 16\,{\rm V}$ (red line) and $V_{\rm g} = 11\,{\rm V}$ (blue line, scaled $\times 3$ and offset for clarity) (see text for discussion).The four peaks at positive bias at $V_{\rm g} = 16\,{\rm V}$ are fit to Gaussian functions, with the fits shown in the lower right of the figure. The peaks labeled $1''$,$2''$,$3''$... correspond to WGM resonances probed at the energy $\varepsilon = \mu_0 + eV_{\rm b}$, whereas the peaks labeled $1'$,$2'$,$3'$..., are the same WGM resonances probed at the Fermi level $\varepsilon = \mu_0$, giving rise to the WGM$''$ and WGM$'$ fringes in the gate maps, respectively. The resonance spacing of order $40\,{\rm mV}$ translates into a cavity radius of $50\,{\rm nm}$, using the relation $\Delta\varepsilon = \pi\hbar v_{\rm F}/r$ (see text).

common origin. As will be discussed below, the WGM$''$ resonances correspond to tunneling into the pn junction modes at energy $\varepsilon = \mu_0 + eV_b$ [where μ_0 is the local Fermi level, see Fig.7-1(a)], whereas the WGM$'$ resonances reflect the action of the STM tip as a top gate, allowing tunneling into the same resonance mode at $\varepsilon = \mu_0$.

7.3 Model for graphene whispering gallery modes

To clarify the WGM character of the STM resonances, we analyze graphene's Dirac carriers in the presence of a potential induced by the STM tip described by the Hamiltonian $\mathcal{H} = \mathcal{H}_0 + U(\boldsymbol{r})$, where $\mathcal{H}_0$ is the kinetic energy term and $U(\boldsymbol{r})$ describes the STM tip potential seen by charge carriers. Because relevant length scales — the electron's Fermi wavelength and the pn ring radius — are much greater than the atomic spacing, we focus on the low-energy states. We linearize the graphene electron spectrum near the K and K$'$ points, bringing $\mathcal{H}_0$ to the massless Dirac form: $[v_F \boldsymbol{\sigma} \cdot \boldsymbol{p} + U(\boldsymbol{r})]\psi(\boldsymbol{r}) = \varepsilon\psi(\boldsymbol{r})$, where $\boldsymbol{p} = i\hbar\nabla_{\boldsymbol{r}}$ and $\boldsymbol{\sigma} = (\sigma_x, \sigma_y)$ are pseudospin Pauli matrices. We take the tip potential to be radially symmetric, reflecting the STM tip geometry. Furthermore, the distance from the tip to graphene (d) is considerably smaller than the electrons Fermi wavelength and the pn ring radius, both of which are smaller than the STM tip radius. We can therefore use a parabola to approximate the tip potential, $U(\boldsymbol{r}) = \kappa \boldsymbol{r}^2$ (where $\boldsymbol{r}$ is the off-center displacement). The potential curvature κ, which affects the energy spectrum of WGM resonances, can be tuned with the bias and gate potentials, as discussed below.

The WGM states can be described by the polar decomposition ansatz

$$\psi_m(r,\theta) = \frac{e^{im\theta}}{\sqrt{r}} \begin{pmatrix} u_A(r)e^{-i\theta/2} \\ u_B(r)e^{i\theta/2} \end{pmatrix}, \tag{7.1}$$

where m is a half-integer angular momentum quantum number, θ is the polar angle, and A, B label the two graphene sublattices. We nondimensionalize the Schrödinger equation using the characteristic length and energy scales ($r_* = \sqrt{Rd}$, $\varepsilon_* = \hbar v_F/\sqrt{Rd}$) to obtain the radial eigenvalue equation of the two-component spinor $u(r)$ with com-

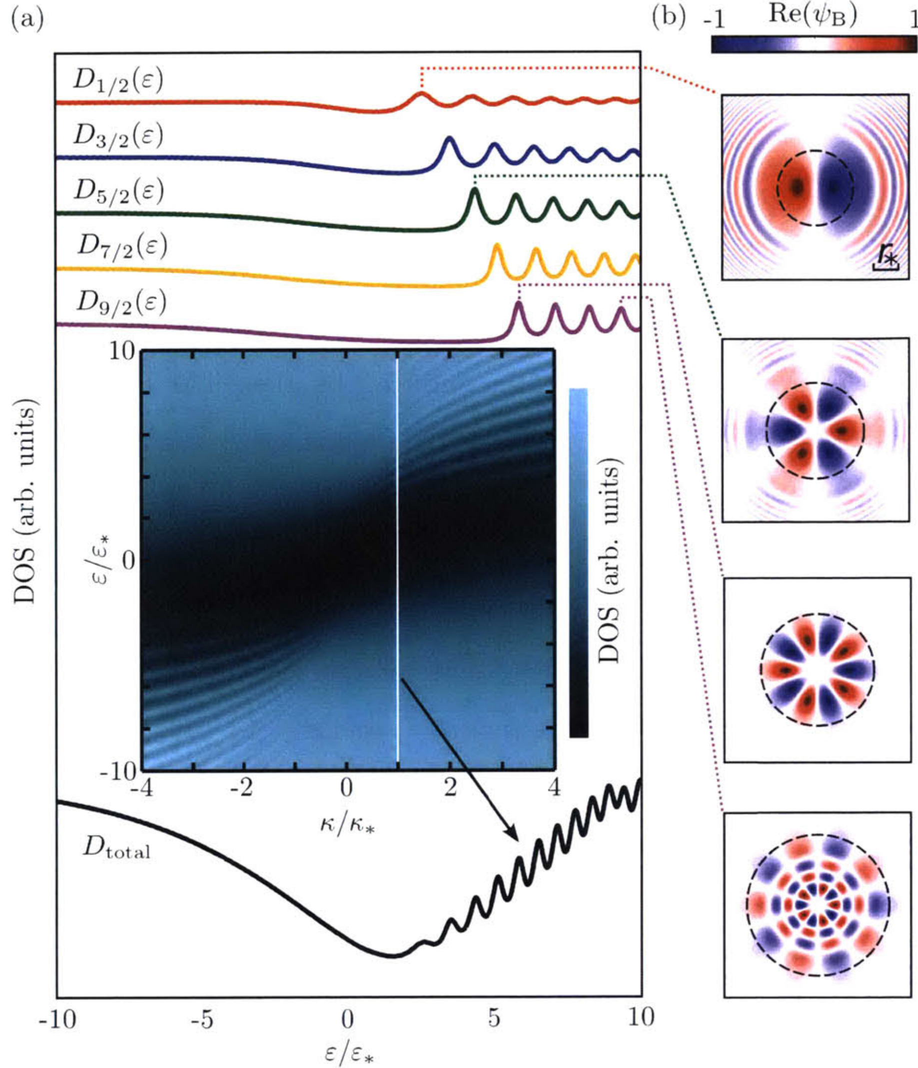

Figure 7-3: Contributions of the WGM resonances with different m to the DOS for the relativistic Dirac model. (a) Colored curves represent partial-m contributions from angular momentum values $m = 1/2, 3/2, 5/2, 7/2, 9/2$ [see Eq.(7.3)], evaluated for a confining potential $U(\boldsymbol{r}) = \kappa \boldsymbol{r}^2$ with curvature value $\kappa = \kappa_* = \varepsilon_*/Rd$. Different curves show the partial DOS contributions defined in Eq.(7.3), which are offset vertically for clarity. The inset shows the total DOS versus particle energy ε and the curvature κ (see text). The black curve shows the total DOS trace along the white line. (b) The Dirac wavefunction for different WGM states [see Eq.(7.1)]. Spatial structure is shown for several resonances in the partial DOS (black dashed circles mark the pn junction rings). The quantity plotted, $\mathrm{Re}(\psi_B)$, is the same as in Fig.7-1(b).The length scale $r_* = \sqrt{Rd}$ (the same in all panels) is marked. Note the confinement strength increasing with m.

ponents $u_A(r)$ and $u_B(r)$:

$$\left[-i\sigma_x\partial_r + (m/r)\sigma_y + \kappa r^2\right]u(r) = \varepsilon u(r). \tag{7.2}$$

Here r is in units of r_*, ε is in units of ε_*, and κ is in units of $\kappa_* = \varepsilon_*/r_*^2$. The tunneling current, expressed through the local density of states (DOS), is modeled as

$$I = \int_{\mu_0}^{\mu_0+eV_b} d\varepsilon \mathrm{T}(\varepsilon, V_b)\sum_m D_m(\varepsilon), \tag{7.3}$$

which is valid for modest V_b values [117]. Here μ_0 is the Fermi energy under the tip, which in general is different from ambient Fermi energy μ_∞ as a result of gating by the tip (see below). The transmission function $\mathrm{T}(\varepsilon, V_b)$, which depends on the tip geometry, work function and DOS, will be taken as energy-independent. The quantity $D(\varepsilon) = \sum_m D_m(\varepsilon)$ represents the sum of partial-m contributions to the total DOS beneath the tip.

To find the eigenstates of the Hamiltonian, Eq.(7.2), we use the finite difference method in the interval $0 < r < L$ with large enough L and with a large repulsive potential at $r = L$ in order to confine the eigentstates. We use a finite range $-M \leq m \leq M$ for the azimuthal quantum numbers with the value M chosen large enough to represent accurately the states in the energy range of interest. The local density of states beneath the tip, $D(\varepsilon) = \sum_m D_m(\varepsilon)$, used for modeling the conductance maps, Eq.(7.6), is calculated from the eigenvalues and eigenstates of the Hamiltonian, Eq.(7.2), as

$$D_m(\varepsilon) = \sum_{l=1}^{2N} \frac{\gamma}{\pi}\frac{\langle|u_l(r=0)|^2\rangle_\ell}{(\varepsilon-\varepsilon_l)^2+\gamma^2} \tag{7.4}$$

Here, the broadening parameter value γ is chosen to be a few times the level spacing, $\gamma \sim \hbar l/L$, l labels the radial eigenstates of Eq.(7.2), and the average $\langle\ldots\rangle_\ell$ denotes

$$\langle|u_l(r=0)|^2\rangle_\ell = \int_0^L dr'|u_l(r')|^2 \exp(-r'^2/2\ell^2) \tag{7.5}$$

The Gaussian in Eq.(7.5) accounts for the finite size of the tunneling area due to the

finite curvature radius of the STM tip and/or a residual asymmetry of the STM tip, both of which allow electrons to tunnel some distance off the tip center. Spurious states arising from the finite potential jumps at the boundaries, localized within a few lattice sites of $r = 0$ and $r = L$ and with energies roughly independent of κ, are excluded from the sum in Eq.(7.4).

The WGM resonances for different partial-m contributions D_m, which combine into the total DOS (Fig.7-3), reveal that individual WGM states exhibit very different behavior depending on the m value [see Figs.7-1(b) and 7-3(b)]. Klein scattering at the circular pn junction produces confinement creating the WGMs, and the confinement is stronger for the large-m modes and weaker for small-m modes. The Klein reflection probability R is strongly dependent on the angle of incidence θ at the pn interface, growing as $R(\theta) \sim 1 - \exp[-\xi \sin^2(\theta)]$, where ξ is a characteristic dimensionless parameter [36]. The value of θ grows with m as $\tan(\theta) \propto m$. As a result, larger values of m must translate into larger reflectivity and stronger confinement. This trend is clearly demonstrated in Figs.7-1(b) and 7-3(b). Also, as m increases, mode wavefunctions are being pushed away from the origin, becoming more localized near the pn ring, in full accord with the WGM physics.

7.3.1 Fringe duplicity in the STM spectral maps

To understand how one family of WGM resonances gives rise to two distinct fans of interference features seen in the data (Fig.7-2), we must account carefully for the gating effect of the STM tip. We start with recalling that conventional STM spectroscopy probes features at energies $\varepsilon_n = \mu_0 + eV_b$, where ε_n are the system energy levels. This corresponds to the family WGM$''$ in our measurements. However, as discussed above, the tip bias variation causes the Fermi level beneath the tip to move through system energy levels ε_n, producing an additional family of interference features (WGM$'$) described by $\varepsilon_n = \mu_0$ To model this effect, we evaluate the differential conductance $G = dI/dV_b$ from Eq.(7.3), taking into account the dependence μ_0 versus V_b . This gives

$$G \propto (1 - \zeta)D(\mu_0 + eV_b) + \zeta D(\mu_0) \tag{7.6}$$

with $\zeta = -\partial\mu_0/\partial(eV_b)$. The two contributions in Eq.(7.6) describe the WGM$'$ and WGM$''$ families. We note that the second family originates from the small electron compressibility in graphene, resulting in a finite ζ and would not show up in a system with a vanishingly small ζ (e.g., in a metal). We use Eq.(7.6) with a value $\zeta = 1/2$ to generate Fig.7-2(b). In doing so, we use electrostatic modeling described in the following section to relate the parameters (ε, κ) in the Hamiltonian, Eq.(7.2), and the experimental knobs (V_b, V_g).

7.3.2 Electrostatic modeling

We use the Thomas-Fermi (TF) model to relate the parameters (ε, κ) in the Hamiltonian, Eq.(7.2), to the experimental knobs (V_b, V_g). Since the graphene-tip distance d is much smaller than the tip radius R, $d \ll R$, the tip-induced carrier density in graphene $\delta n = \mathrm{sgn}(\mu)\mu^2/\pi(\hbar v_F)^2 n_\infty$ can be modeled as

$$\frac{\mathrm{sgn}(\mu)\mu^2}{\pi(\hbar v_F)^2} - n_\infty = -\frac{e(V_b - V_{cpd}) + \mu}{4\pi e^2(d + r^2/2R)}. \tag{7.7}$$

Here, μ is the position-dependent Fermi energy taken relative to the Dirac point, n_∞ is the carrier density far from the STM tip (controlled by the gate potential), and V_{cpd} is the contact potential difference between the tip and neutral graphene. The right-hand side of Eq.(7.7), is obtained from a parallel-plate capacitor model with slowly varying interplate-distance $d_t(r) \approx d + r^2/2R$, and neglecting the higher-order corrections due to the curvature of the field lines. This yields a screening length scale $\sqrt{2Rd} \ll R$, as described in the main text. The carrier density far from the tip is controlled by the gate potential as $n_\infty = \epsilon_r e(V_g - V_g^0)/4\pi e^2 d_g$, where ϵ_r and d_g are the dielectric constant and thickness of the dielectric substrate, respectively, and V_g^0 accounts for residual doping in graphene at $V_g = 0$.

For instance, Fig.7-4(a) illustrates the influence of the sample-tip bias acting as a local top gate; the potential profile sign reverses from local hole doping at large positive bias to electron doping at strong negative bias. Figure7-4(b), likewise, illustrates the impact of the back gate potential that is mainly to modify the tails of the local

potential induced by the tunneling tip. This procedure yields a very good agreement with the measured dI/dV_b [Fig.7-2(a) and (b)].

We analyze the nonlinear screening problem accounting for the fact that the spatially varying carrier density may change polarity near the STM tip. This is done with the help of the self-consistent Thomas Fermi (TF) model, Eq.(7.7), treated as an algebraic equation for μ. Parameters of interest for the microscopic model, μ_0 and κ, are obtained directly from Eq.(7.7). The value of $\mu_0 = \mu(r = 0)$ is given by

$$\mu_0(V_b, V_g) = \frac{\beta_1 - \sqrt{\beta_1^2 + 4|\beta_2(V_b, V_g)|}}{2\,\mathrm{sgn}\left[\beta_2(V_b, V_g)\right]}, \tag{7.8}$$

where β_1 and β_2 are

$$\beta_1 = \frac{(\hbar v_F)^2}{4e^2 d}, \quad \beta_2(V_b, V_g) = \beta_1 \left[e(V_b - V_{cpd}) - \frac{\epsilon_r d}{d_g} e(V_g - V_g^0) \right]. \tag{7.9}$$

The parameter κ in our parabolic approximation for $U(\boldsymbol{r})$ is calculated as $\kappa = -\mu''(0)/2$ and giving

$$\kappa(V_b, V_g) = -\frac{\beta_1}{2Rd} \frac{e(V_b - V_{cpd}) + \mu_0(V_b, V_g)}{\sqrt{\beta_1^2 + 4|\beta_2(V_b, V_g)|}} \tag{7.10}$$

Importantly, we note that the potential term in our model Hamiltonian, $U(\boldsymbol{r}) = \kappa \boldsymbol{r}^2$, is unbounded, whereas in reality it has a maximum value $U(|\boldsymbol{r}| \to \infty) = \mu_0 - \mu_\infty$ (see Fig.7-4). This constrains the regions in the (V_g, V_b) map where the WGMs are expected to occur. In particular, states with energy $|\varepsilon| > |\mu_0 - \mu_\infty|$ do not have a bipolar character (i.e., do not form a *pn* junction). In order to include the finite value for $U(|\boldsymbol{r}| \to \infty)$ in plotting Fig.7-2(b), we treat the value of κ as given by Eq.(7.10) when $|\varepsilon| \leq |\mu_0 - \mu_\infty|$, with $\mathrm{sgn}(\varepsilon) = \mathrm{sgn}(\mu_0 - \mu_\infty)$, and as $\kappa = 0$ otherwise.

7.3.3 Model parameters

In our calculations, we use a system of size $L/r_* = 20$. The interval $0 < r < L$ was discretized with $N = 1200$ points, yielding a 2400×2400 matrix for each value of κ

and m. The azimuthal quantum number maximum value $M = 17/2$ was used. In Eq.(7.4), we used the value of $\gamma/\varepsilon_* = 0.2$ for broadening and $\ell = r_*$ for the Gaussian width parameter. The latter corresponds to an effective tunneling region of size $\ell \sim r_* \sim 22\,\mathrm{nm}$, where r is obtained for typical STM tip parameter values (see details below). Such values for the tunneling region size, while they may seem to be a bit on the high side, are in fact not unreasonable: For instance, the off-center tunneling rate decays exponentially, governed by the WKB exponent $\sim \exp[-2d_t(r)\sqrt{2m_0\Phi}/\hbar]$, where d_t is the local tip-graphene distance, m_0 is the effective electron mass and Φ is the work function. The spread for electrons away from the tip center can be estimated from $d_t(r) \approx d(1 + r^2/2Rd)$, yielding an effective value of $(r_*/\ell)^2 = 2d\sqrt{2m_0\Phi}/\hbar \sim 5$ (here we used the electron mass $m_0 \sim 9.1 \cdot 10^{31}\,\mathrm{kg}$, $\Phi \sim 1\,\mathrm{eV}$, and $d \sim 0.5\,\mathrm{nm}$). We expect fabrication-induced tip asymmetries to be in the same ballpark.

For parameter values that we use for our TF model, we take $R \approx 1\,\mu\mathrm{m}$, $d \approx 0.5\,\mathrm{nm}$, and $V_{\mathrm{cpd}} \approx 0.3\,\mathrm{V}$. This yields characteristic length and energy scales $r_* \approx 22\,\mathrm{nm}$ and $\varepsilon_* \approx 30\,\mathrm{meV}$, respectively. The backgate in our device is separated from graphene by a dielectric of thickness $d_{\mathrm{g}} \approx 300\,\mathrm{nm}$ and a dielectric constant $\varepsilon \approx 5$. We also introduce a gate potential offset of $V_{\mathrm{g}}^0 = 10\,\mathrm{V}$ to match the residual doping observed in our experiments.

7.3.4 Other experimental features

In addition to explaining how the two sets of fringes, WGM′ and WGM″, originate from the same family of WGM resonances, our model accounts for other key features observed in the data. In particular, it explains the large difference in the WGM′ and WGM″ periodicities noted above. It also correctly predicts the regions where fringes occur [Fig.7-2(b)]. The bipolar regime in which *pn* junction rings and resonances in the DOS occur (see fig.7-4) takes place for the probed energies ε of the same sign as the potential curvature. In the case of a parabola $U(\boldsymbol{r}) = \kappa \boldsymbol{r}^2$, this gives the condition $\varepsilon\kappa > 0$, corresponding to the upper-right and lower-left quadrants in Fig.7-3(a), inset. However, under experimental conditions, the potential is bounded by $U(|\boldsymbol{r}| \to \infty) = \mu_0 - \mu_\infty$ [see Fig.7-1(a)], which constrains the regions in which WGMs

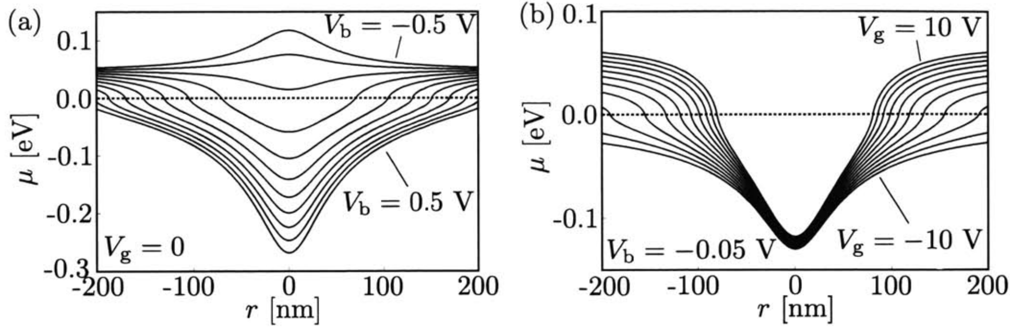

Figure 7-4: Radial Fermi energy profile obtained from the Thomas-Fermi model. (a) The profile is calculated from Eq.(7.7) as a function of bias voltage V_b varying from 500 mV to 500 mV in steps of 100 mV for a fixed gate voltage $V_g = 0$, and in (b) it was calculated as a function of gate voltage V_g varying from -10 V to 10 V in steps of 2 V for fixed bias voltage $V_b = 50$ mV. In both panels, we included the effect of residual doping in graphene by adding a gate potential offset of $V_g^0 = 10$ V, see text. The tip-induced circular *pn* and *np* junctions appear when the potential profile crosses 0 eV (dotted lines). The *pn* junction radius varies between 0 and 100 nm.

are actually observed. As discussed above, accounting for the finite value $U(|\boldsymbol{r}| \to \infty)$ yields the condition $|\varepsilon| \leq |\mu_0 - \mu_\infty|$, with $\mathrm{sgn}(\varepsilon) = \mathrm{sgn}(\kappa) = \mathrm{sgn}(\mu_0 - \mu_\infty)$. This gives the WGM$'$ and WGM$''$ regions in Fig.7-2(b) bounded by white dashed and white dotted lines, respectively, and matching accurately the WGM$'$ and WGM$''$ location in the measurements.

The range of m values that the NIST measurement can probe depends on the specifics of the tunneling region at the STM tip. We believe that a wide range of m values can be accessed; however, we are currently unable to distinguish different partial-m contributions, because the corresponding resonances are well aligned (Fig.7-3). Different m states may contribute if the tunneling center is not the same as the geometric center of the tip, which is highly likely. As shown in [105], higher m states can be accessed by going off center by as little as 1 nm, which is likely in our real experiment due to a residual asymmetry of the STM tip [we model this effect by a Gaussian factor in Eq.(7.3)]. We note in this regard that different angular momentum m values translate into different orbital magnetic moment values, opening an opportunity to probe states with different m by applying a magnetic field (see Chap.8).

7.4 Discussion

The explanation of the observed resonances in terms of the whispering-gallery effect in circular *pn* rings acting as tunable electronic WGM resonators has other notable ramifications. First, it can shed light on puzzling observations of resonances in previous STM measurements [118–120], which hitherto remained unaddressed. Second, a highly tunable setup in which the electron wavelength and cavity radius are each controlled independently lends itself well to directly probing other fundamental electron-optical phenomena, such as negative refractive index for electron waves, Veselago lensing [39], and Klein tunneling [37]. Further, we envision probing more exotic phenomena such as the development of caustics, where an incident plane wave is focused at a cusp [121–123], and special bound states for integrable classes of dynamics might be observed, where the electron path never approaches the confining boundary at perpendicular incidence [124]. These advances will be enabled by the distinct characteristics of graphene that allow for electronic states to be manipulated at the microscale with unprecedented precision and tunability, thus opening a wide vista of graphene-based quantum electron-optics.

Chapter 8

Berry phase and giant non-reciprocity in Dirac quantum dots

In this chapter I show that recently created Dirac quantum dots [104] grant access to exotic behavior not available in conventional quantum dots.[1] In particular, I predict giant non-reciprocity in the quantum dot resonance spectra induced by the Berry phase. Arising in weak magnetic fields, non-reciprocity is manifest in anomalously large splittings of quantum dot resonances which are degenerate at $B = 0$ due to time-reversal symmetry. The resonance splitting, which is governed by a field-induced jump in the Berry phase of confined electronic states, is strongest for gapless Dirac systems and becomes quenched with increasing bandgaps. In the small bandgap regime, the Berry phase splitting overwhelms the conventional orbital and spin-induced splitting. The predicted giant non-reciprocity, available in the large family of two-dimensional Dirac materials, is accessible via Faraday and Kerr optical rotation measurements and scanning tunneling spectroscopy.

[1] Reproduced from J. F. Rodriguez-Nieva, L. S. Levitov, Berry phase and giant non-reciprocity in Dirac quantum dots, submitted for publication in *Phys. Rev. Lett.* (arXiv:1508.06609).

8.1 Non-reciprocity in Dirac quantum dots

Recently, a new class of quantum dots embedded in two-dimensional Dirac materials has been introduced [104]. These Dirac quantum dots exploit nanoscale *pn*-junction rings induced by electrostatic potentials as a vehicle for confinement of electronic states [121, 124–128]. Confined states in these ring-shaped electron resonators, manifested through resonances appearing periodically in scanning tunneling spectroscopy maps [104], arise due to the constructive interference of electronic waves scattered at the *pn* junction [36, 37] and inward-reflected from the ring. In this Chapter, I show that the novel mechanism for electronic confinement can be exploited for accessing exotic and potentially useful behavior, which is not available in conventional quantum dots.

In particular, I predict that the Berry phase, a distinguishing topological feature of Dirac materials [33, 129–131], induces a strongly non-reciprocal spectrum of quantum dot resonances,

$$\varepsilon_{n,m} \neq \varepsilon_{n,-m}, \tag{8.1}$$

in the presence of a weak magnetic field B; here m and n denote the azimuthal and radial quantum numbers, respectively. As we will see, resonance splittings of the $\pm m$ states, which are degenerate at $B = 0$, grow precipitously with magnetic field, approaching values as large as half the quantum dot resonance period $\Delta\varepsilon$. In particular, for the weak magnetic fields B of interest, the effect dominates over conventional orbital and spin-induced splitting.

8.2 Non-reciprocity: semiclassical model

This anomalous behavior can be understood from a simple semiclassical picture describing confined electrons in a gapless two-band system. Considering a confining potential with circular symmetry, the resonance spectrum $\varepsilon_{n,m}$ of the quantum dot can be obtained from the WKB condition for $\varphi_{\text{orb}} = \oint_C d\boldsymbol{r} \cdot \boldsymbol{k}$, the usual orbital phase

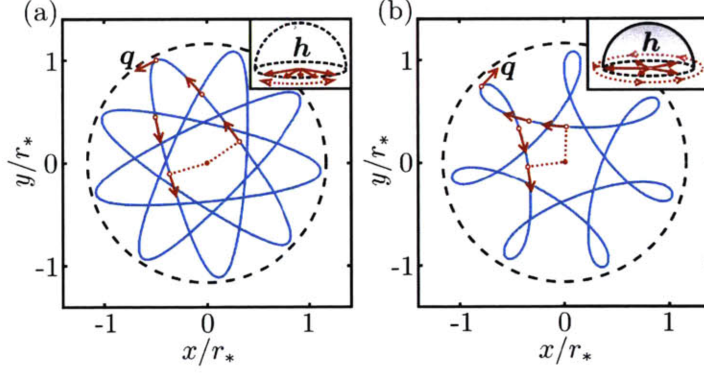

Figure 8-1: Manipulation of the Berry phase φ_{B} of confined Dirac electrons using magnetic fields. Shown are semiclassical orbits of massless particles exhibiting topologically distinct orbital behavior corresponding to (a) $B < B_{\mathrm{c}}$ and (b) $B > B_{\mathrm{c}}$ [see critical field B_{c} in Eq.(8.5)]. The Berry phase, determined by the solid angle subtended by $\boldsymbol{h} = (h_x, h_y, h_z)$ in Eq.(8.3), jumps from $\varphi_{\mathrm{B}} = 0$ to $\varphi_{\mathrm{B}} = \pi$ at $B = B_{\mathrm{c}}$, see insets [for gapless systems $h_{x,y} = v\, q_{x,y}$ and $h_z = 0$, with $q_{x,y}$ the kinetic momentum (red vectors) and v the Fermi velocity]. Here I used $m = 1/2$, energy $\varepsilon = 1.35\, \hbar v_{\mathrm{F}}/r_*$, with r_* defined in Eq.(8.9), $B/B_{\mathrm{c}} = 0.8$ for (a) and $B/B_{\mathrm{c}} = 1.6$ for (b).

accumulated along the classical path $\mathcal{C}$:

$$\varphi_{\mathrm{orb}}(\varepsilon, m) + \varphi_{\mathrm{B}}(\varepsilon, m) = 2\pi(n + \nu), \tag{8.2}$$

with ν a constant [33, 131, 132]. Crucially, direct band coupling in Dirac materials gives rise to a geometric gauge field which is manifested in Eq.(8.2) via the Berry phase,

$$\varphi_{\mathrm{B}} = \oint_{\mathcal{C}} d\boldsymbol{h} \cdot \langle \boldsymbol{h}_+ | i\nabla_{\boldsymbol{h}} | \boldsymbol{h}_+ \rangle = S(\mathcal{C})/2. \tag{8.3}$$

Here $S(\mathcal{C})$ denotes the solid angle subtended by the vector $\boldsymbol{h} = (h_x, h_y, h_z)$ along a closed path $\mathcal{C}$, with $\boldsymbol{h}$ defined in terms of the two-band Hamiltonian $\mathcal{H} = \boldsymbol{\sigma} \cdot \boldsymbol{h} + h_0$ [h_0 is a scalar function and $\boldsymbol{\sigma} = (\sigma_x, \sigma_y, \sigma_z)$ are Pauli matrices]. In Eq.(8.3), $|\boldsymbol{h}_+\rangle$ is the $\boldsymbol{h}$-dependent electron-like eigenstate, with $\mathcal{H}|\boldsymbol{h}_\pm\rangle = (\pm|\boldsymbol{h}| + h_0)|\boldsymbol{h}_\pm\rangle$. Importantly, the Berry phase in a gapless system ($h_z = 0$) can only take, in each semiclassical period along $\mathcal{C}$, values $\varphi_{\mathrm{B}} = 0$ or π. As shown in Fig.8-1, a small magnetic field can switch from one case to the other. In particular, for $B = 0$ we find $\varphi_{\mathrm{B}}(\varepsilon, \pm m) = 0$, whereas in weak magnetic fields we find $\varphi_{\mathrm{B}}(\varepsilon, m) = \pi$ and $\varphi_{\mathrm{B}}(\varepsilon, -m) = 0$. As a result, the WKB condition in Eq.(8.2) for the $\pm m$ states is shifted by half a period

and a large resonance splitting (Fig.8-2) emerges:

$$\varepsilon_{n,m} - \varepsilon_{n,-m} \approx \Delta\varepsilon/2. \quad \text{(gapless)} \tag{8.4}$$

While the same semiclassical picture applies to gapped Dirac systems ($h_z > 0$), there are important differences with respect to the gapless case. In particular, the solid angle subtended by the vector $\boldsymbol{h}$, which now points towards the upper hemisphere, is strictly smaller than 2π; non-reciprocity induced by the Berry phase which becomes quenched at increasing bandgaps, as will be shown with a more detailed quantum model in Fig.8-4. In the limit $|h_z| \gg |h_{x,y}|$, conventional orbital non-reciprocity dominates.

8.3 Features of the non-reciprocal effect

The jump in Berry phase corresponds to a transition from convex orbits to skipping orbits (Fig.8-1). This observation allows us to define the critical field B_c that induces giant non-reciprocity, i.e. the field necessary to reverse the electron velocity at the outer classical return point. Taking as an example massless Dirac electrons in a parabolic confining potential $U(\boldsymbol{r}) = \kappa \boldsymbol{r}^2$,

$$B_c = \frac{2\hbar c}{e}\frac{\kappa m}{\varepsilon}, \tag{8.5}$$

is obtained, where e is the electron charge and c is the speed of light. Using typical values obtained in recent experiments [104], $\kappa \approx 4 \cdot 10^{-6}\,\mathrm{eV/nm^2}$, $\varepsilon \approx 10\,\mathrm{meV}$ and $m = 1/2$, we find values for B_c on the order of $0.2\,\mathrm{T}$.

Besides the splitting arising at $B = B_c$, another key fingerprint of the non-reciprocal effect is the m-dependence of B_c shown in Eq.(8.5). This feature can be understood by noticing that, for larger m, a larger B is necessary to induce skipping orbits. As we will see, the m dependence of B_c gives rise to a peculiar branching pattern of the quantum dot resonances which can be probed in spectral measurements away from the quantum dot center, as shown in Fig.8-5.

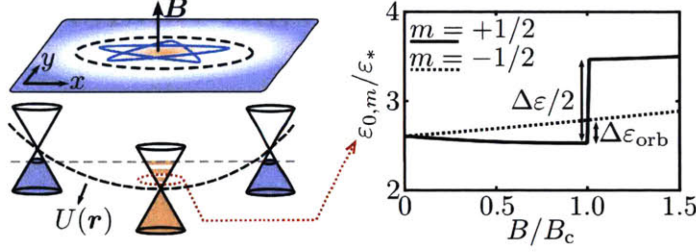

Figure 8-2: Magnetic response of quantum dot resonances in a gapless Dirac system. The quantum dot is defined by the circular pn ring (dashed lines) induced by a radial electrostatic potential $U(\boldsymbol{r})$. (b) The magnetic response is dominated by the Berry-phase splitting of magnitude $\Delta\varepsilon/2$, larger than the orbital splitting $\Delta\varepsilon_{\rm orb}$. The peak splitting is calculated from Eq.(8.2) for $n = 0$, $m = \pm 1/2$, and $\nu = 0.6$; B_c is calculated from Eq.(8.5) with $\varepsilon = \varepsilon_{0,\pm 1/2} \approx 2.6\,\varepsilon_*$ [see ε_* in Eq.(8.9)].

Importantly, the above semiclassical argument to explain the giant non-reciprocal effect relies on B being negligibly small so that it has hardly any significant effect on $\varphi_{\rm orb}$. This is particularly true for small m values, given that it is easier to deflect the orbital motion of charge carriers at the pn ring in a weak magnetic field. More quantitatively, I show in Fig.8-2 the solution of Eq.(8.2) for $n = 0$ and $m = \pm 1/2$. For typical model parameters, the $\Delta\varepsilon/2$ splitting induced by the Berry phase jump can be sizable and can dominate over the conventional orbital splitting $\Delta\varepsilon_{\rm orb}$. This effect becomes more dramatic at larger n and smaller m.[2]

Compared to previous mechansims for non-reciprocity in electronic systems, which are highly sought for in photonics and plasmonics, our realization is perhaps the first one which is inherent to Dirac materials. Indeed, Faraday and Kerr rotation, two notable examples of non-reciprocity which can be sizable in two dimensional materials such as graphene [44, 45], are also present in general semiconducting materials. The same applies to magnetoplasmonic effects, e.g. unidirectional low frequency edge modes [133–137], which are also present in generic two-dimensional structures [133].

[2] I note that the Zeeman splitting is negligibly small for the B fields of interest. The energy E_Z for Zeeman splitting due to the intrinsic spin of the electron, $\varepsilon_Z/\varepsilon_* = (\mu_B B_*/\varepsilon_*)\cdot(B/B_*) \approx 10^{-3}\cdot(B/B_*)$, is much smaller than the Berry phase splitting which is on the order of ε_* (here $\mu_B \approx 5.8\cdot 10^{-5}\,{\rm eV/T}$ is the Bohr magneton).

8.4 Non-reciprocity: quantum model

To contrast the simple semiclassical picture above with a more refined quantum model, I consider the Dirac equation describing confined electrons under the influence of a uniform magnetic field:

$$[v\boldsymbol{\sigma}\cdot\boldsymbol{q} + (\Delta_{\rm g}/2)\sigma_z + U(\boldsymbol{r})]\,\psi(\boldsymbol{r}) = \varepsilon\psi(\boldsymbol{r}). \tag{8.6}$$

Here v is the band velocity for electrons, $\Delta_{\rm g}$ the bandgap and $\boldsymbol{q}$ the kinematic momentum with components $q_{x,y} = p_{x,y} - eA_{x,y}/c$ and $q_z = 0$ ($A_{x,y}$ is the vector potential and $p_{x,y} = -i\hbar\partial_{x,y}$ is the momentum). Note that $\boldsymbol{h}$ in Eq.(8.3) corresponds to $\boldsymbol{h} = v\boldsymbol{q}$. Because we are interested in eigenstates confined inside the pn ring, with radius smaller than the characteristic length of the electrostatic potential, it is legitimate to use a parabolic potential model $U(\boldsymbol{r}) \approx \kappa\boldsymbol{r}^2$. By preserving rotational symmetry using the Coulomb gauge $A_x = -By/2$ and $A_y = Bx/2$, the eigenstates of Eq.(8.6) can be expressed using the polar decomposition ansatz,

$$\psi_m(r,\theta) = \frac{e^{im\theta}}{\sqrt{r}}\begin{pmatrix} u_1(r)e^{-i\theta/2} \\ iu_2(r)e^{i\theta/2}\end{pmatrix}, \tag{8.7}$$

with m a half-integer number. This decomposition allows us to rewrite Eq.(8.6) as

$$\begin{pmatrix} r^2 - \varepsilon + \Delta_{\rm g}/2 & \partial_r + m/r - Br/2 \\ -\partial_r + m/r - Br/2 & r^2 - \varepsilon - \Delta_{\rm g}/2 \end{pmatrix}\begin{pmatrix} u_1 \\ u_2 \end{pmatrix} = 0 \tag{8.8}$$

Here r and B are in units of r_* and B_*, respectively, whereas ε and $\Delta_{\rm g}$ are in units of ε_*, with

$$r_* = \sqrt[3]{\hbar v/\kappa} \sim 60\,\mathrm{nm}, \quad \varepsilon_* = \sqrt[3]{(\hbar v)^2\kappa} \sim 10\,\mathrm{meV},$$
$$B_* = (\hbar c/e)\cdot\sqrt[3]{(\kappa/\hbar v)^2} \sim 0.2\,\mathrm{T}. \tag{8.9}$$

In these estimates, I considered (gapped) graphene $v = v_{\rm F} \approx 10^6\,\mathrm{m/s}$ as a model system and used a typical value of $\kappa = 4\cdot 10^{-6}\,\mathrm{eV/nm^2}$, see estimates below.

A suitable diagnostics of non-reciprocity, allowing direct access to quantum dot resonances, is the local density of states $D(\varepsilon)$ inside the quantum dot. Naturally, $D(\varepsilon)$ can be obtained experimentally via the dI/dV in STS measurements as in Ref. [104]. The quantity $D(\varepsilon)$ at $r = r_0$ can be conveniently written as the sum of m-state contributions $D(\varepsilon) = \sum_m D_m(\varepsilon)$, with

$$D_m(\varepsilon) = \sum_l \langle |u_l(r = r_0)|^2 \rangle_\ell \delta(\varepsilon - \varepsilon_l). \tag{8.10}$$

Here l labels the radial eigenstates of Eq.(8.8) for fixed m, and $\langle |u_l(r = r_0)|^2 \rangle_\ell = \int_0^\infty dr' |u_l(r')|^2 e^{-(r'-r_0)^2/2\ell^2}$ represents a spatial average of the wavefunction centered at $r = r_0$. A gaussian weight is included in the density of states to account for the finite size of the tunneling region in real STS measurements [104].

8.4.1 Electrostatic potential modeling

Estimates for κ used in Eq.(8.6) can be obtained following the electrostatic model developed in Chapter 7 describing a biased metallic sphere proximal to the graphene plane [Fig.8-3(a)]. This portrays quite accurately a metallic STM tip on top of graphene. As before, I denote R the metallic sphere radius, and d the sphere-graphene distance. A potential bias differential δV_b between the sphere and graphene [see Fig.8-3(b)–(c)] results in a spatially varying image charge density profile given by

$$\delta n(r) \approx -\frac{e\delta V_\mathrm{b} + \mu(r)}{4\pi e^2 (d + r^2/2R)}. \tag{8.11}$$

Here $\delta n(r) = \mathrm{sgn}[\mu(r)]\mu(r)^2/\pi(\hbar v_\mathrm{F})^2 - n_\infty$ is the sphere-induced charge density variation on graphene, with $\mu(r)$ the Fermi energy and n_∞ the gate-induced carrier density far from the center. Equation (8.11) is obtained from a parallel-plate capacitor model with slowly varying interplate-distance $d_\mathrm{c}(r) \approx d + r^2/2R$. Higher order terms arising from the curvature of the electric field lines are neglected.

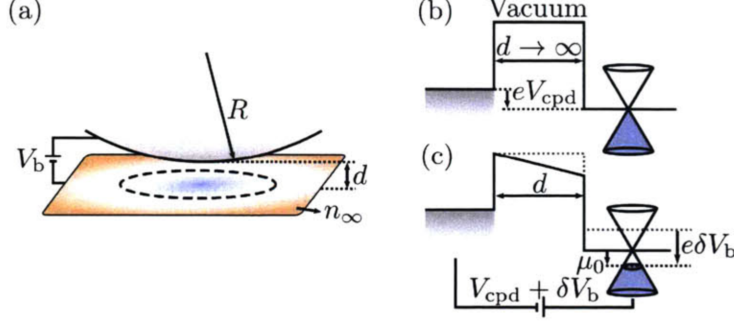

Figure 8-3: Modeling of the electrostatic potential. (a) Schematics of the electrostatic model, showing a metallic sphere of radius R separated by a distance d from the graphene plane. A potential bias V_b applied on the sphere induces a local variation of the carrier density, different from the carrier concentration density n_∞ far from the sphere. (b)-(c) Band structure schematics showing band alignment between the metallic sphere and graphene for (b) large separation and (c) close proximity. Here V_{cpd} is the contact potential difference between graphene and the metallic sphere, $\delta V_b = V_b - V_{cpd}$, and μ_0 is the Fermi energy under the sphere.

A straight-forward calculation yields a value of $\kappa = -\mu''(0)/2$ given by

$$\kappa = -\frac{e\delta V_b + \mu_0}{2Rd\sqrt{1+|\beta|}}. \tag{8.12}$$

The variable μ_0 is the Fermi level under the sphere, and β is a dimensionless number:

$$\begin{aligned} \mu_0 &= \frac{(\hbar v_F)^2}{8e^2 d}\frac{1-\sqrt{1+|\beta|}}{\mathrm{sgn}(\beta)}, \\ \beta &= \frac{16e^2 d}{(\hbar v_F)^2}\left[e\delta V_b - 4\pi e^2 d n_\infty\right]. \end{aligned} \tag{8.13}$$

Considering typical values of $R \sim 1\,\mu\text{m}$, $d \sim 5\,\text{nm}$, $\delta V_b \sim 0.1\,\text{V}$ and $n_\infty \sim 10^{11}\,\text{cm}^{-2}$, we obtain the value of $\kappa \sim 4 \cdot 10^{-6}\,\text{eV/nm}^2$.

8.4.2 Details of the numerical simulation

To solve Eq.(8.8), I use the finite difference method in the interval $0 < r < L$. The azimuthal quantum numbers are chosen in a finite range, $-M \leq m \leq M$, with M large enough to represent accurately the states in the energy range of interest. In the calculations, I used a system of size $L/r_* = 12$ discretized in $N = 1100$ lattice sites, with maximum azimuthal quantum number $M = 31/2$.

To calculate the density of states, Eq.(8.10), I approximate the delta-function $\delta(\varepsilon)$ by a Lorentzian $\delta(\varepsilon) \approx \gamma/\pi(\varepsilon^2+\gamma^2)$ and use a broadening $\gamma/\varepsilon_* = 0.25$, and set a Gaussian weight $\ell/r_* = 0.1$ in the spatial average $\langle \ldots \rangle_\ell$ of the wavefunctions.

8.4.3 Quantum model results

Figure 8-4 shows the resulting quantum dot spectrum as a function of B for gapless and gapped $[\Delta_{\rm g}/\varepsilon_* = 5]$ Dirac systems, exhibiting the B-induced splitting of quantum dot resonances [here I used $r_0 = 0$, $\ell/r_* = 0.1$ and plotted $\partial D/\partial\varepsilon$ in Eq.(8.10) in order to enhance the spectral features]. In agreement with the semiclassical interpretation, a half-period splitting is observed in the gapless spectral maps in Fig.8-4(a). The splitting of the resonances for gapped systems, however, is less prominent; in particular, the splitting for a gapped Dirac system is dominated by the orbital contribution.

Indeed, the peak splitting for the low-energy resonances in gapped Dirac systems ($\varepsilon \gtrsim \Delta_{\rm g}$) can be quantified using a simple non-relativistic model that is valid in the limit $\Delta_{\rm g} \gg \varepsilon_*$. In this case, expansion of the Dirac Equation in powers of $\Delta_{\rm g}$ results in a massive Schrödinger Equation for the first spinor component $\psi_1(\boldsymbol{r})$:

$$\left[\boldsymbol{q}^2/2\Delta_{\rm g} + U(\boldsymbol{r}) + \Delta - eB/2c\Delta\right]\psi_1 = \varepsilon_{n,m}\psi_1,$$
$$\varepsilon_{n,m} = \hbar\omega\left(2n + |m_-| + 1\right) - \mu_\Delta m_+ B. \tag{8.14}$$

Here $\varepsilon_{n,m}$ are the quantized eigenvalues, $\omega = \sqrt{2\kappa/\Delta + e^2B^2/4c^2\Delta^2}$, and $m_\pm = m \pm 1/2$. Importantly, the orbital magnetic moment $\mu_\Delta = e\hbar v^2/2c\Delta$, which is 3/2 times larger that the orbital magnetic moment of a free, massive Dirac particle at the Dirac point, induces the peak splitting observed in Fig.8-4(b).

Furthermore, because in Fig.8-4 the wavefunction is probed at the center of the quantum dot, $r_0 = 0$, only small m states ($m = \pm 1/2$) contribute to the spectral maps. It is important to stress that large m states, which can be probed in off-centered scanning tunneling spectroscopy measurements, are equally susceptible to the Berry phase splitting. Figure 8-5 shows such spectral maps, in which the wavefunctions are

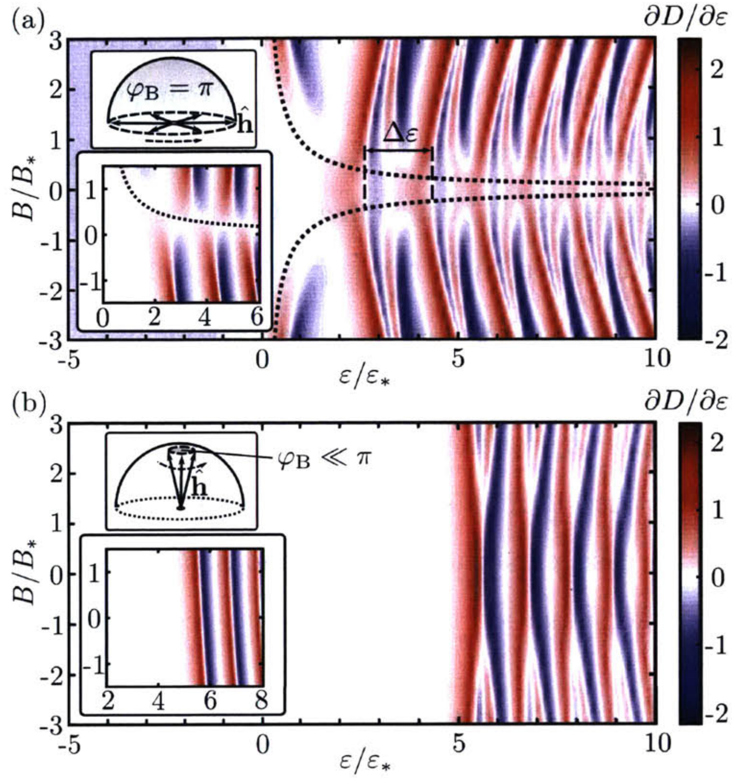

Figure 8-4: Spectral maps showing the splitting of periodic time-reversed resonances under weak magnetic fields in (a) gapless and (b) gapped Dirac quantum dots. Resonance splitting is shown to be dominated by (a) a half-period jump in gapless systems, and (b) orbital effects in gapped systems. The distinct behavior between (a) and (b) are also shown in the partial $m = 1/2$ contribution to the spectral maps (see insets). Characteristic units for the magnetic field, B_*, is defined in Eq.(8.9). Plotted with dotted lines in (a) is Eq.(8.5) for $m = \pm 1/2$. To enhance the spectral features, I plot in both panels the derivative of the local Density of States in Eq.(8.10) $[r_0 = 0]$.

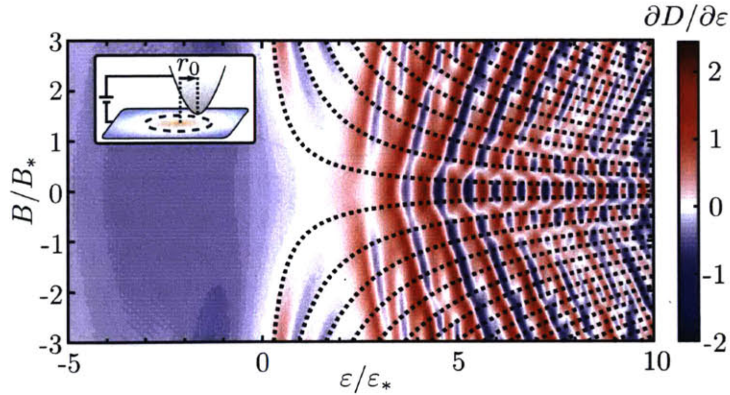

Figure 8-5: Off-centered spectral maps for a gapless Dirac quantum dot displaying large m splitting of resonances in weak magnetic fields. Plotted with dotted lines is Eq.(8.5) for half-integer m. The off-centered spectral map is qualitatively different from the centered case in Fig.8-4, given that the centered spectral map is sensitive primarily to $m = \pm 1/2$ states.

probed at $r_0 = r_*$. In this case, there is an overlap of the peak splitting at different values of B, highlighted with fans of B_c in Eq.(8.5) for varying m (dotted lines).

8.5 Semiclassical quantization

I now turn to discuss the details of the semiclassical analysis above which ellucidates several important aspects of the non-reciprocal effect. Here I focus on three aspects: the topological origin of the non-reciprocal effect, the semiclassical quantization of the quantum dot resonances and the derivation of the critical magnetic field B_c in Eq.(8.5). Firstly, to understand the topological origin of the non-reciprocal effect it is necessary to map the momentum $\boldsymbol{q}$ to the surface of a torus, see Fig.8-6. This is possible because, being circularly symmetric, the two-dimensional quantum dot is integrable: confined Dirac electrons perform quasiperiodic orbits with constants of motion ε and m.[3] For the semiclassically bound orbits, I obtain $\boldsymbol{q}$ as a function of

[3] At $B = 0$ bound quasiperiodic orbits exist if $\varepsilon/\varepsilon_* > \sqrt[3]{27m^2/4}$; electrons then move in the classically allowed region $r_1 \leq r \leq r_2$.

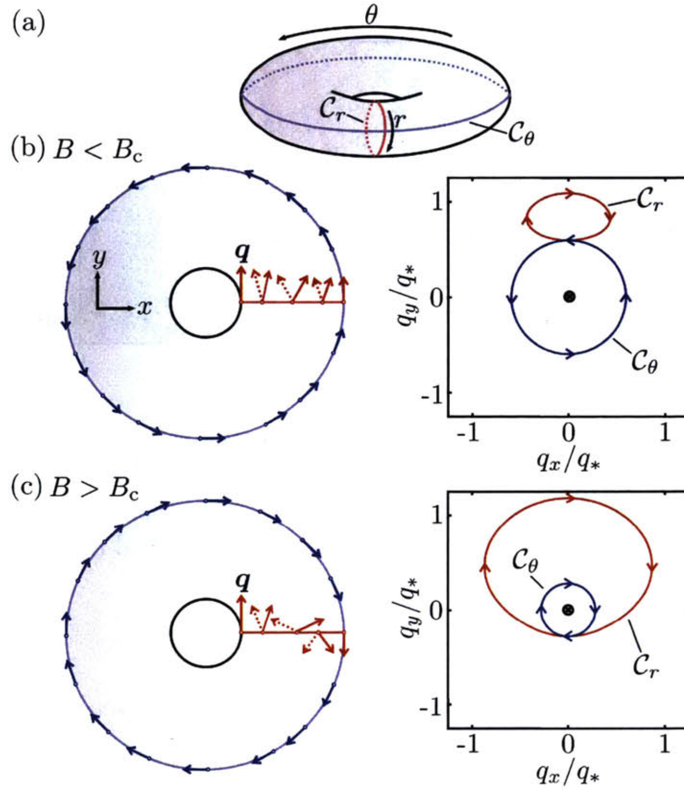

Figure 8-6: Topologically distinct mappings of q [Eq.(8.15)] to the surface of a torus (a), plotted for (b) $B < B_c$ and (c) $B > B_c$. Indicated with blue(red) arrows is q along the curves $\mathcal{C}_\theta(\mathcal{C}_r)$ shown in panel (a), where dotted lines/arrows indicate a curve/vector in the bottom surface of the torus. At $B = B_c$, there is a transition between trivial and non-trivial winding of q along $\mathcal{C}_r$. This results in a B-induced phase jump of the Berry phase. Here I define $q_* = \varepsilon_*/\hbar v$ and use the same parameter values as in Fig.8-1.

position given by

$$q_r = k_r = \pm\sqrt{[\varepsilon - U(r)]^2 - (m/r - Br/2)^2},$$
$$q_\theta = k_\theta - eA_\theta = m/r - Br/2. \tag{8.15}$$

The distinct topology between the cases $B > B_c$ and $B < B_c$ is shown in Fig.8-6, where q is plotted along two curves: $\mathcal{C}_\theta$ in the toroidal direction and $\mathcal{C}_r$ in the poloidal direction. For $B < B_c$, q always points towards the same toroidal direction. For $B > B_c$, however, q acquires a non-trivial winding along $\mathcal{C}_r$.

Secondly, the semiclassical quantization of quantum dot resonances in Eq.(8.2) can be readily obtained using q in Eq.(8.15) evaluated on both $\mathcal{C} = \mathcal{C}_\theta$ and $\mathcal{C} = \mathcal{C}_r$.[4] This

[4]This method of quantization on the surface of an invariant tori is known as Einstein-Brillouin-

yields two conditions which allows us to quantize both m and ε. For simplicity, here I consider $\Delta_{\rm g} = 0$. For $\mathcal{C} = \mathcal{C}_\theta$, Eq.(8.2) yields $m = n_\theta + \nu_\theta - \varphi_{\rm B}/2\pi$, where $\varphi_{\rm B} = -\pi$ independently of B [see blue curves in panels (b) and (c) of Fig.8-6]. Using $\nu_\theta = 0$, the anticipated quantization of angular momentum m=half–integer is obtained. For $\mathcal{C} = \mathcal{C}_r$, instead, I obtain $\int_{r_1}^{r_2} dr\, k_r = 2\pi(n_r + \nu_r - \varphi_{\rm B})$, where the limits of integration r_1 and r_2 are the classical return points. As shown with red curves in Fig.8-6(b)-(c), $\varphi_{\rm B} = 0$ for $B < B_{\rm c}$ and $\varphi_{\rm B} = -\pi$ for $B > B_{\rm c}$; as such, there is a discrete jump of the Berry phase term ocurring at $B = B_{\rm c}$ which leads to the half period shift in the quantization condition.[5]

Thirdly, the critical field $B_{\rm c}$ in Eq.(8.5) can be obtained by noticing that resonance splittings occur when q_θ changes sign at the outer classical return point. From Eq.(8.15), I obtain $q_\theta = m\hbar/r_2(\varepsilon) - eB_{\rm c}r_2(\varepsilon)/2c = 0$, with $r_2(\varepsilon) = \sqrt{\varepsilon/\kappa}$ corresponding to the outer return point [i.e. $q_r(r_2) = 0$]. This condition yields $B_{\rm c}$ in Eq.(8.5).

8.6 Semiclassical analysis of quantum dot resonances

As discussed above, several important features of the quantum model can be derived from semiclassical considerations. These include the half-period shift of the quantum dot resonances, Eq.(8.4), and the magnetic field $B_{\rm c}$ necessary to induce a π-jump in the Berry phase $\varphi_{\rm B}$, Eq.(8.5). Not shown above is the excellent agreement between the resonance dispersion obtained semiclassically and those obtained from the full quantum model. Here I show such agreement for the dispersion of the quantum dot

Keller (EBK) quantization rule. It differs from the usual way of quantizing carrier motion using closed orbits obtained from semiclassical equations of motion. The EBK method applies to completely integrable d-dimensional systems as well as chaotic systems. For more details, see Ref. [132].

[5] In gapped systems the π Berry flux, or Berry curvature, is non-zero over a finite region of momentum space. As a result, for $B > B_{\rm c}$, the path $\mathcal{C}_r$ does not cover the entire π Berry flux: the jump in $\varphi_{\rm B}$ is smooth and smaller in magnitude than in the $\Delta_{\rm g} = 0$ case.

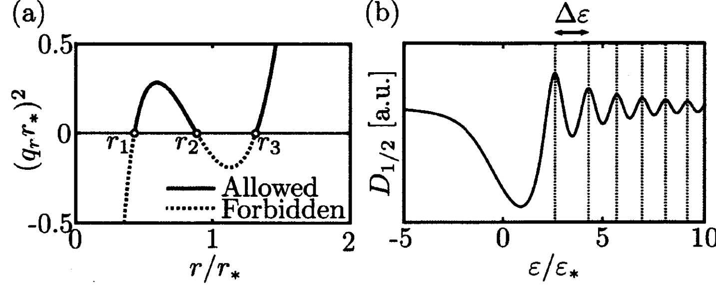

Figure 8-7: Comparison between semiclassical and quantum models. (a) Plot of the radial wavevector q_r in Eq.(8.15), showing the classically allowed and forbidden regions for $B = 0$ and $m = 1/2$. (b) Comparison between quantum dot resonances obtained from the WKB interference conditions and from the full quantum model. Shown with solid lines is the partial $m = 1/2$ contribution $D_{1/2}(\varepsilon)$ to the total density of states calculated from the quantum model. Solutions to Eq.(8.16), with $\nu = 0.6$, are shown with dotted lines. Resonances are here shown to be quasi-periodic in energy, with period $\approx \Delta\varepsilon$.

resonances at $B = 0$ obtained from the WKB condition:

$$\int_{r_1/r_*}^{r_2/r_*} dr' \sqrt{(\varepsilon/\varepsilon_* - r'^2)^2 - (m/r')^2} = \pi(n + \nu) - \varphi_{\mathrm{B}}. \qquad (8.16)$$

In Eq.(8.16), $r_{1,2}$ are the classical return points for confined orbits [see Fig.8-7(a)], m is the azimuthal quantum number, r_* and ε_* are defined in Eq.(8.9), ν was set to $\nu = 0.6$ and, as discussed above, $\varphi_{\mathrm{B}} = 0$ for $B = 0$. Resonances for quantum and semiclassical model are compared in Fig.8-7(b) and excellent agreement is obtained. Resonances are approximately equally spaced, with period $\Delta\varepsilon$; this results from the obrbital phase in Eq.(8.16) being an approximately linear function of ε over a wide range $\varepsilon/\varepsilon_* \lesssim 10$, where ε_* is given in Eq.(8.9).

8.7 Semiclassical equations of motion

The semiclassical orbits in Fig.8-1 were obtained using the semiclassical theory of Bloch electrons. This theory, which describes the motion of a narrow wavepacket, is obtained by superimposing Bloch states driven by perturbations that vary in real space. Considering a wavepacket parametrized in terms of the position $\boldsymbol{r}$ and mo-

mentum $\boldsymbol{k}$, the semiclassical equations of motion are

$$\begin{aligned} \dot{\boldsymbol{r}} &= \nabla_{\boldsymbol{k}}\tilde{\varepsilon}/\hbar - \dot{\boldsymbol{k}} \times \tilde{\boldsymbol{B}}_{\boldsymbol{k}}, \\ \hbar\dot{\boldsymbol{k}} &= -e\boldsymbol{E} - (e/c)\dot{\boldsymbol{r}} \times \boldsymbol{B}. \end{aligned} \tag{8.17}$$

Here $\tilde{\boldsymbol{B}}_{\boldsymbol{k},z} = \nabla_{\boldsymbol{k}} \times \tilde{\boldsymbol{A}}_{\boldsymbol{k}}$ denotes the Berry curvature and $\tilde{\varepsilon}_{\boldsymbol{k}} = \varepsilon_{\boldsymbol{k}} + \boldsymbol{m}_{\boldsymbol{k}} \cdot \boldsymbol{B}$ denotes a magnetically shifted energy. Both the Berry curvature and the orbital magnetic moment $\boldsymbol{m}_{\boldsymbol{k}}$ are intrinsic properties of the band since they do not depends on the shape and size of the wavefunction:

$$\tilde{\boldsymbol{B}}_{\boldsymbol{k},z} = \frac{2}{3}\frac{\Delta_{\mathrm{g}}/\hbar v_{\mathrm{F}}}{[(\Delta_{\mathrm{g}}/\hbar v_{\mathrm{F}})^2 + 4k^2/3]^{3/2}}, \quad \boldsymbol{m}_{\boldsymbol{k},z} = \frac{e\Delta_{\mathrm{g}}/3\hbar}{(\Delta_{\mathrm{g}}/\hbar v_{\mathrm{F}})^2 + 4k^2/3}, \tag{8.18}$$

where the $+(-)$ sign corresponds to the K(K′)-point. For the semiclassical theory to be valid, the perturbations have to be sufficiently weak such that transitions between different electron energy bands can be neglected. In the particular case of graphene, because $\Delta_{\mathrm{g}} = 0$, both $\tilde{\boldsymbol{B}}_{\boldsymbol{k},z}$ and $\boldsymbol{m}_{\boldsymbol{k},z}$ are concentrated at the Dirac point and are zero elsewhere.

8.8 Discussion

Given that our predictions only rely on direct band coupling, they can be tested in a wide range of Dirac materials and metamaterials. In particular, the strong dependence of resonance splitting on Δ_{g} can be explored using various material systems: graphene is the prototypical material to explore the case $\Delta_{\mathrm{g}} = 0$; graphene on top of closely-aligned hBN substrate allows us to explore the case $\Delta_{\mathrm{g}} \sim 50\,\mathrm{meV}$ [25, 26]; monolayers of transition metal dichalcogenides such as MoS_2 allows us to explore Δ_{g} on the eV ballpark [138–140]. Furthermore, the value of ε_* can also be tuned with the electrostatic potential shape, as demonstrated in Ref. [104].

Interestingly, the anomalous strength of the non-reciprocal effect allows us to envision a new class of optical devices, such as nanoscale isolators and circulators, which are driven by the Berry phase. In particular, I expect photonic effects in Dirac

quantum dots to be dramatic. Indeed, electrostatic doping can, via the Pauli blocking mechanism, induce a strong and tunable electron-photon coupling. This, combined with the in situ tunability of the resonance dispersion [104], can make Dirac quantum dots critical components for miniaturizing nanophotonic systems.

I also stress that the non-reciprocal effect resonates with other exotic predictions of the Berry phase manifestations in Dirac systems, such as Berry phase modification to exciton spectra [141, 142], optical gyrotropy induced by Berry's phase [143] and chiral plasmons in gapped Dirac systems [144, 145]. In realistic electronic systems, however, electron decoherence usually hinders observation of such subtle effects. As a result, I anticipate that readily available quantum dots states in Dirac materials enable a new and optimal setting for locally probing Berry phase physics.

8.9 Chapter summary

To summarize, I predict that quantum dots embedded in Dirac materials grant access to a novel non-reciprocity mechanism which is induced by the Berry phase. This mechanism, which is unique to Dirac materials, leads to stronger non-reciprocity than other known mechanisms. The anomalous strength of the effect and the in situ tunability of the quantum dot resonance dispersion make Dirac quantum dots an appealing platform for non-reciprocal nanophotonics. This, combined with the recent introduction of Dirac quantum dots in graphene, makes the predictions easily testable in on-going experiments.

Part III

Photophysics in disordered graphene systems

Chapter 9

Disorder-induced Raman spectroscopy

Raman spectroscopy is a powerful non-destructive characterization technique that provides invaluable information about graphitic samples, [146–148] such as phonon properties, [149–151] doping, [152,153] and the number of layers [154] for both few-layer graphenes and carbon nanotubes. In particular, the D and D′ bands ($\sim 1350\,\mathrm{cm}^{-1}$ and $\sim 1620\,\mathrm{cm}^{-1}$ for 2.4 eV laser excitation energy, E_L, respectively) originate from the presence of defects in the sample, such as grain boundaries [155–157] or point defects [158,159]. For this reason, these defect-induced Raman features, distinct from the defect-free G band ($\sim 1585\,\mathrm{cm}^{-1}$) and the G′ band ($\sim 2680\,\mathrm{cm}^{-1}$), have been widely used to assess the graphene materials' quality when used in graphene-based devices [150].

The origin of the interband D and intraband D′ bands has been previously discussed by several authors by using the characteristics of the so-called double resonant (DR) Raman scattering process [159–165]. This explanation has been successfully applied to qualitatively describe some of the important aspects of the D and D′ bands. Most notably, the dispersive behavior of the D-band Raman shift [166,167] as a function of E_L was successfully explained within the DR picture.

Despite the numerous theoretical and experimental works on the DR process, some of the most interesting and potentially useful questions about the characterization of

defects in graphene remain to be answered. For instance, the distinguishing signatures of the different types of defects regarding the Raman spectra remain an open problem. Do edges or grain boundaries have different fingerprints in the Raman spectra than those for point defects? Do all defects have the same laser energy dependence? Are the D and D′ bands affected differently by each type of point defect? Ultimately, the open question that needs to be addressed is whether Raman spectroscopy can be used as an accurate and non-destructive tool to, not only quantify, but also to distinguish and characterize specific defects from one another in sp^2 graphitic materials.

In this chapter, I present an analytical study of the double resonant Raman scattering process in graphene.[1] In particular, I derive analytical expressions for the D and D′ integrated Raman intensities that explicitly show the dependencies on laser energy, defect concentration, and electronic lifetime. Importantly, I find good agreement between the analytical results and experimental measurements on samples with increasing defect concentrations and at various laser excitation energies. In addition, I also address several of the above-mentioned questions. For instance, comparison between the models for the edge-induced and the disorder-induced D band intensity suggests that edges or grain boundaries can be distinguished from disorder by the different dependence of their Raman intensity on laser excitation energy. Similarly, the type of disorder can potentially be identified not only by the intensity ratio $I_{\mathrm{D}}/I'_{\mathrm{D}}$, but also by the laser energy dependence of the Raman feature. I also discuss in this chapter the use of Raman spectroscopy to identify the nature of defects

9.1 Current status of the double resonance theory

Several experimental results have already paved the way for progress in understanding the double resonance (DR) physics. For example, the laser energy E_{L} dependence of the frequently used $I_{\mathrm{D}}/I_{\mathrm{G}}$ ratio between the D-band and the G-band intensities has been measured by many groups on samples with various types of defects [168]

[1]Reproduced from J. F. Rodriguez-Nieva, E. B. Barros, R. Saito, M. S. Dresselhaus, Disorder-induced double resonant Raman process in graphene, *Phys. Rev. B* **90**, 235410 Copyright 2014 by the American Physical Society.

and at different concentrations, thereby providing a large body of information about defects. While some samples [158, 159] show an $I_{\mathrm{D}}/I_{\mathrm{G}} \propto E_{\mathrm{L}}^{-4}$ dependency [see Fig.9-1(a)], other measurements have shown a weaker power-law exponent [169, 170]. Furthermore, it was recently shown by Eckmann *et al.* [170] that, even within a single sample, the Raman intensities of the D and D′ bands can have different laser energy dependencies, as well as suggesting that the D and D′ intensity ratio can be different depending on the type of defect [171]. Since the D and D′ bands originate from, respectively, intervalley and intravalley elastic scattering of the photoexcited electron-hole pair, the scattering potential should play an important role in determining the Raman scattering amplitude.

In addition, several studies have focused on the dependence of the integrated D-band intensity as a function of defect concentration [172, 173]. In its simplest approximation, the integrated intensity depends linearly on the defect concentration. However, experimental measurements show that I_{D} reaches a peak value at a sufficiently large concentration of defects [see Fig. 9-1(b)], when the average distance L_{d} between defects is $\sim 3\,\mathrm{nm}$ [173].

Numerical calculations of the Raman cross section have previously been the dominant procedure used to model the features of the Raman spectra induced by several types of defects. In this way, several authors studied the problem of disorder, [174] edges, [175] grain boundaries, [176] and isotope impurities [177]. Given that the DR process is a fourth-order process involving interactions between electrons, phonons, photons, and defects, and requires knowledge of the phonon dispersion relations, electronic band structure, and electron lifetimes, numerical techniques provide a powerful and effective way to address the defect problem. However, the above-mentioned experimental observations are difficult to understand directly from calculations.

Alternatively, analytic calculations require a series of approximations which affect the predictive power of the resulting model, but allow for a more insightful analysis into the underlying physics involved. One notable step in this direction was taken by Basko [178–180]. There, the author obtained analytical expressions for the Raman intensity for the G′ band [178, 179] and for the edge-induced D band [180]. For

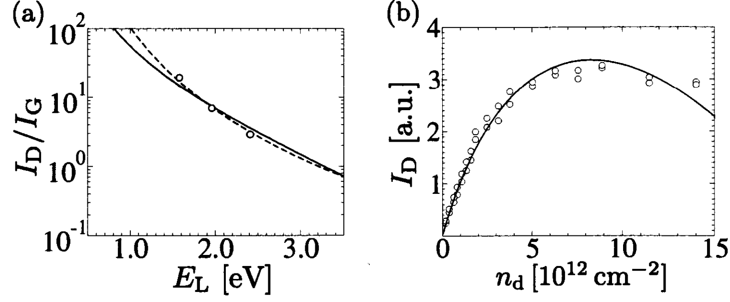

Figure 9-1: Dependence of the integrated Raman intensity on laser energy and impurity density. (a) Laser energy dependence of the integrated Raman intensity ratio I_D/I_G between the D and G bands obtained from Eq.(9.16) (solid line), and experimental points from Ref. [158]. For the I_G intensity, I use the standard textbook dependence of $I_G \propto E_L^4$ [178]. The dashed line indicates the frequently used $I_D/I_G \propto E_L^{-4}$ fit. (b) The integrated D-band intensity as a function of defect concentration n_d obtained from Eq.(9.16) (solid line), and experimental points of Ref. [172].

instance, power-law dependencies on the inverse electron lifetime γ of the integrated Raman intensity of the G′ band and its overtones were obtained, suggesting the use of the ratio of these Raman intensities to indirectly measure the pertinent electronic lifetimes [179].

Interestingly, both edges and disorder produce a D-band feature in the Raman spectra. However, the description of the intermediate states in the edge-induced Raman scattering case [180] already incorporates eigenstates in the presence of the edge (i.e. scattered states, instead of plane waves), while the DR picture used to describe the disorder-induced Raman scattering uses plane waves perturbed by an external potential. Therefore, the edge-induced Raman scattering is studied as a third-order process, [180] while the disorder-induced Raman scattering is studied as a fourth-order process [161,162]. Then, a comparison between the predictions for the D band induced by these two types of defects is necessary.

In this chapter, I perform a detailed analytical study of the DR theory which brings to light the role played by the different parameters of the model, such as the laser energy, scattering potential, and electronic lifetimes. For this purpose, I obtain analytic expressions for the disorder-induced Raman intensity within the DR theory using the effective Hamiltonian description. I then do a comparison between our model and recent experimental measurements, and discuss the main features of our

results in relation to the above-mentioned experimental observations. Furthermore, I compare the results with the analytical models obtained for the edge-induced D band [180]. This analysis yields, additionally, a quantitative discussion of phase interference effects [160, 174].

The outline of this chapter is as follows: In Sec.9.2 I briefly review the theory of the DR Raman process. In Sec.9.3 I make a detailed analysis of the DR Raman intensity, quantifying the contribution from each of several different scattering processes that are possible, and the main results are summarized in Sec.9.4.

9.2 Raman intensity calculation

The DR process is understood as an inelastic fourth-order process that involves interactions of photoexcited electron-hole pairs with phonons and defects. Referring to Fig.9-2 and neglecting finite-temperature effects, I here consider only Stokes scattering. The photoabsorption in its initial state is described by an incoming photon with momentum $\boldsymbol{Q}_{\rm i}$, energy $E_{\rm L}$, and polarization $\lambda_{\rm i}$, and the graphene system (electrons and phonons) is initially in its ground state. The possible final states are described by the production of a phonon with momentum $\boldsymbol{q}_{\rm ph}$, mode β, and frequency $\omega_{\boldsymbol{q}_{\rm ph},\beta}$, a photon with momentum $\boldsymbol{Q}_{\rm f}$ and polarization $\lambda_{\rm f}$, and the graphene electronic system is back to its ground state. Elastic scattering with a defect is necessary in order to guarantee momentum conservation in the DR process.

Here I compute the DR Raman scattering probability $\mathcal{I}_{\rm DR}$, defined as the total DR Raman probability of an incoming photon with momentum $\boldsymbol{Q}_{\rm i}$ and polarization $\lambda_{\rm i}$. The electromagnetic field is assumed to be confined in a box of volume $V = AL_z$, where A is the area of the graphene layer and L_z is the length of the box in the direction normal to the graphene plane. Then, $\mathcal{I}_{\rm DR}$ is calculated ($\hbar = 1$) as

$$\mathcal{I}_{\rm DR} = \frac{2\pi L_z}{c} \sum_{\substack{\boldsymbol{Q}_{\rm f},\lambda_{\rm f} \\ \boldsymbol{q}_{\rm ph},\beta}} |\mathcal{M}(\boldsymbol{q}_{\rm ph},\beta)|^2 \delta(E_{\rm L} - c|\boldsymbol{Q}_{\rm f}| - \omega_{\boldsymbol{q}_{\rm ph},\beta}), \tag{9.1}$$

where c is the speed of light, $E_{\rm L} = c|\boldsymbol{Q}_{\rm i}|$, and the matrix $\mathcal{M}(\boldsymbol{q}_{\rm ph},\beta) = \sum_p \mathcal{M}_p(\boldsymbol{q}_{\rm ph},\beta)$

describing the Raman scattering arises from consideration of all possible Feynman diagrams p for the interactions, shown in Fig.9-2. The Raman intensity $I_{\rm DR}$, which is the magnitude measured in experiments, is related to $\mathcal{I}_{\rm DR}$ by the simple relation $I_{\rm DR} = I_0 \times \mathcal{I}_{\rm DR}$, where I_0 is the intensity of incoming photons.

Following the notation introduced by Venezuela *et al*, [174] I label the aa processes as those in which either only electrons or only holes participate in the scattering (left column in Fig.9-2), while ab processes are those in which both electrons and holes participate in the scattering (right column in Fig.9-2). Furthermore, I indicate in Fig.9-2 the notation used individually for each process p.

I focus mostly on the calculation of the matrix $\mathcal{M}_p(\boldsymbol{q}_{\rm ph}, \beta)$ for the ee and eh processes throughout this paper, given that the extension to the remaining processes is straightforward. Explicitly, the matrices $\mathcal{M}_{ee}(\boldsymbol{q}_{\rm ph}, \beta)$ and $\mathcal{M}_{eh}(\boldsymbol{q}_{\rm ph}, \beta)$ for the diagrams ee and eh in Fig.9-2, respectively, are given by

$$\mathcal{M}_{ee}(\boldsymbol{q}_{\rm ph}, \beta) = \sum_{\boldsymbol{p}\in{\rm BZ}} \frac{\langle \psi_{\boldsymbol{p},-}|\hat{\mathcal{H}}_{\rm eR,f}|\psi_{\boldsymbol{p},+}\rangle \langle \psi_{\boldsymbol{p},+}|\hat{\mathcal{H}}_{\rm ep,\beta}|\psi_{\boldsymbol{p}+\boldsymbol{q}_{\rm ph},+}\rangle \langle \psi_{\boldsymbol{p}+\boldsymbol{q}_{\rm ph},+}|\hat{\mathcal{H}}_{\rm ed}|\psi_{\boldsymbol{p},+}\rangle}{(E_{\rm L} - \omega_{\boldsymbol{q}_{\rm ph},\beta} - \varepsilon_{\boldsymbol{p},+} + \varepsilon_{\boldsymbol{p},-} - i\gamma/2)(E_{\rm L} - \varepsilon_{\boldsymbol{p}+\boldsymbol{q}_{\rm ph},+} + \varepsilon_{\boldsymbol{p},-} - i\gamma/2)} \times \frac{\langle \psi_{\boldsymbol{p},+}|\hat{\mathcal{H}}_{\rm eR,d}|\psi_{\boldsymbol{p},-}\rangle}{(E_{\rm L} - \varepsilon_{\boldsymbol{p},+} + \varepsilon_{\boldsymbol{p},-} - i\gamma/2)}, \tag{9.2}$$

and

$$\mathcal{M}_{eh}(\boldsymbol{q}_{\rm ph}, \beta) = -\sum_{\boldsymbol{p}\in{\rm BZ}} \frac{\langle \psi_{\boldsymbol{p}+\boldsymbol{q}_{\rm ph},-}|\hat{\mathcal{H}}_{\rm eR,f}|\psi_{\boldsymbol{p}+\boldsymbol{q}_{\rm ph},+}\rangle \langle \psi_{\boldsymbol{p},-}|\hat{\mathcal{H}}_{\rm ep,\beta}|\psi_{\boldsymbol{p}+\boldsymbol{q}_{\rm ph},-}\rangle}{(E_{\rm L} - \omega_{\boldsymbol{q}_{\rm ph},\beta} - \varepsilon_{\boldsymbol{p}+\boldsymbol{q}_{\rm ph},+} + \varepsilon_{\boldsymbol{p}+\boldsymbol{q}_{\rm ph},-} - i\gamma/2)} \times \frac{\langle \psi_{\boldsymbol{p}+\boldsymbol{q}_{\rm ph},+}|\hat{\mathcal{H}}_{\rm ed}|\psi_{\boldsymbol{p},+}\rangle \langle \psi_{\boldsymbol{p},+}|\hat{\mathcal{H}}_{\rm eR,d}|\psi_{\boldsymbol{p},-}\rangle}{(E_{\rm L} - \varepsilon_{\boldsymbol{p}+\boldsymbol{q}_{\rm ph},+} + \varepsilon_{\boldsymbol{p},-} - i\gamma/2)(E_{\rm L} - \varepsilon_{\boldsymbol{p},+} + \varepsilon_{\boldsymbol{p},-} - i\gamma/2)} \tag{9.3}$$

where the summation over electronic momentum $\boldsymbol{p}$ is taken over the graphene hexagonal Brillouin zone (BZ), $\hat{\mathcal{H}}_{\rm eR}$, $\hat{\mathcal{H}}_{\rm ep}$, and $\hat{\mathcal{H}}_{\rm ed}$ denote the electron-radiation, electron-phonon, and electron-defect interactions, respectively, $-(+)$ denotes the hole (electron) band, $\varepsilon_{\boldsymbol{p},-}$ ($\varepsilon_{\boldsymbol{p},+}$) is the energy of a hole (electron) with wave vector $\boldsymbol{p}$, and γ is the electronic broadening. In particular, I assume that $\gamma = \gamma_{\rm ep} + \gamma_{\rm ed}$ has contributions from electron-phonon scattering ($\gamma_{\rm ep} \sim$ meV) or electron-defect scattering ($\gamma_{\rm ed} \sim$ meV), and that, in comparison, the contribution from electron-photon scattering

($\gamma_{\rm eR} \sim \mu$eV) can be neglected. At electronic energies comparable to those of photons in the visible range, a value of $\gamma_{\rm ep} \sim 15\,$meV is obtained [181]. The value of $\gamma_{\rm ed}$ can be calculated from Fermi's golden rule $\gamma_{\rm ed} = 2\pi \sum_{\boldsymbol{p}'} |\langle \psi_{\boldsymbol{p}',+}|\mathcal{H}_{\rm ed}|\psi_{\boldsymbol{p},+}\rangle|^2 \delta(\varepsilon_{\boldsymbol{p},+} - \varepsilon_{\boldsymbol{p}',+})$, where $\varepsilon_{\boldsymbol{p},+} \sim E_{\rm L}/2$ (see Sec.9.4.2 for details). Furthermore, I consider throughout this work that $\gamma(\sim 10\,\text{meV}) \ll \omega_{\boldsymbol{q}_{\rm ph},\beta}(\sim 0.2\,\text{eV}) \ll E_{\rm L}(\sim 2\,\text{eV})$, which is the typical situation in experiments.

The characteristic feature of the DR process is that two of the three denominators in Eqs.(9.2) and (9.3) can be simultaneously zero at specific points in phonon and electronic phase space, and thus has the name double resonance [161]. This is different than the G$'$ band case (two-phonon scattering around $2700\,\text{cm}^{-1}$), where a triple resonance is possible [179], but not discussed here.

Raman measurements yield the number of outgoing photons coming to a detector covering a solid angle $\Omega_{\rm f}$. In order to make direct comparison with experiments, I express $\mathcal{I}_{\rm DR}$ in Eq.(9.1) per unit solid angle $\Omega_{\rm f}$. The summation over outgoing photon momentum $\boldsymbol{Q}_{\rm f}$ can be written as an integral in spherical coordinates given by $\sum_{\boldsymbol{Q}_{\rm f}} = (V/8\pi^3) \int dQ_{\rm f} \int d\Omega_{\rm f} Q_{\rm f}^2$, where $d\Omega_{\rm f}$ is the differential solid angle covered by the outgoing photons. In Eq.(9.1), the matrix $\mathcal{M}$ only depends on the direction $\hat{\boldsymbol{Q}}_{\rm f}$ and polarization $\lambda_{\rm f}$ of the outgoing photon, but not on $|\boldsymbol{Q}_{\rm f}|$, given its small value. Then, energy conservation dictates $c|\boldsymbol{Q}_{\rm f}| = E_{\rm L} - \omega_{\boldsymbol{q}_{\rm ph},\beta}$, and the delta function in Eq.(9.1) is absorbed upon integration on $dQ_{\rm f}$. Therefore,

$$\frac{d\mathcal{I}_{\rm DR}}{d\Omega_{\rm f}} = \frac{V L_z E_{\rm L}^2}{4\pi^2 c^4} \sum_{\boldsymbol{q}_{\rm ph},\beta,\lambda_{\rm f}} |\sum_{p} \mathcal{M}_p(\boldsymbol{q}_{\rm ph},\beta)|^2, \tag{9.4}$$

is obtained, where I used $c|\boldsymbol{Q}_{\rm f}| \approx E_{\rm L}$. The values of $\mathcal{M}_p$ obtained from the diagrams in Fig.9-2 can be used as input for Eq.(9.4) to obtain $d\mathcal{I}_{\rm DR}/d\Omega_{\rm f}$. In the calculations below, I assume unpolarized and normally incident photons, and the detection of backscattered photons in all polarization directions. Furthermore, because the LO and A_1 Raman-active modes produce a Raman shift much larger than their respective linewidth, we can separate the contribution in Eq.(9.4) from each of these modes to the integrated Raman intensity.

9.2.1 Effective Hamiltonian description

To calculate the matrix elements in Eq.(9.4), the effective Hamiltonian developed in Chapter 2 is used. Importantly, because in this effective description the wavefunctions acquire a new pseudospin index s that labels the valley $s =$K, K$'$, then it is necessary to replace the summation sub-index in Eqs.(9.2) and (9.3) as $\sum_{\boldsymbol{p}\in \mathrm{BZ}} \to \sum_{\boldsymbol{k}s}$.

Similarly to the case of magnetic fields in Eq.(2.16), the electron-photon coupling can be obtained as a result of the Peierls substitution $\boldsymbol{p} \to \boldsymbol{p} - e\boldsymbol{A}/c$. More explicitly, the coupling between Dirac electrons and electromagnetic radiation can be described by the term

$$\mathcal{H}_{\mathrm{er}} = -\frac{ev_{\mathrm{F}}}{c}\int_S d\boldsymbol{r}\, \hat{\Psi}^{\dagger}_{\boldsymbol{r}} \begin{pmatrix} \boldsymbol{\sigma}\cdot\boldsymbol{A} & 0 \\ 0 & \bar{\boldsymbol{\sigma}}\cdot\boldsymbol{A} \end{pmatrix} \hat{\Psi}_{\boldsymbol{r}}. \tag{9.5}$$

In general, photon-induced transitions are momentum-conserving. This occurs because the photon wavevector $|\boldsymbol{Q}| = \omega/c$ for frequencies in the visible range or below is much smaller than the unit cell length scale $1/a_0$. For electromagnetic plane waves, $\boldsymbol{A}$ can be descibed as a superposition of photon states with wavevectors $\boldsymbol{Q}$ and polarization λ:

$$\boldsymbol{A} = \sum_{\boldsymbol{Q},\lambda} \sqrt{\frac{2\pi c}{V|\boldsymbol{Q}|}} \left(\hat{a}_{\boldsymbol{Q}\lambda}\boldsymbol{e}_{\boldsymbol{Q}\lambda} + \hat{a}^{\dagger}_{-\boldsymbol{Q}\lambda}\boldsymbol{e}^{*}_{-\boldsymbol{Q}\lambda}\right) e^{i\boldsymbol{Q}\cdot\boldsymbol{r}}. \tag{9.6}$$

Note that, because photons live in three-dimensions, $\boldsymbol{A}$ is normalized by the system volume V. Here $\boldsymbol{e}_{\boldsymbol{Q}\lambda}$ is the polarization vector of mode λ, normal to $\boldsymbol{Q}$, and $\hat{a}_{\boldsymbol{Q}\lambda}(\hat{a}^{\dagger}_{\boldsymbol{Q}\lambda})$ is the photon annihilation (creation) operator.

The electron-phonon interaction results from the change in the carbon-carbon distance induced by lattice vibrations; this distance variation modifies the hopping parameter t. The explicit form of the coupling Hamiltonian $\mathcal{H}_{\mathrm{ep}}$ depends specifically on the symmetry of the phonon mode. For instance, two phonon modes that will play an important role in Raman spectroscopy are the longitudinal optical (LO) phonon mode in the center of the Brillouin zone, i.e. $\boldsymbol{q}_{\mathrm{ph}} \approx 0$, and the A_1 phonon mode in the vicinity of the K-point $\boldsymbol{q}_{\mathrm{ph}} \approx \mathbf{K}$. From symmetry considerations, it has been shown

that the electron phonon coupling is given by [182, 183]

$$\mathcal{H}_{\mathrm{ep,LO}} = -iF_{\mathrm{LO}} \int_S d\boldsymbol{r} \hat{\Psi}^\dagger_{\boldsymbol{r}} \begin{pmatrix} \boldsymbol{\sigma} \times \boldsymbol{u}_{\boldsymbol{r}} & 0 \\ 0 & -\boldsymbol{\sigma}^* \times \boldsymbol{u}_{\boldsymbol{r}} \end{pmatrix} \hat{\Psi}_{\boldsymbol{r}}, \tag{9.7}$$

for the LO phonon mode, and

$$\mathcal{H}_{\mathrm{ep,A_1}} = iF_{\mathrm{A_1}} \int_S d\boldsymbol{r} \hat{\Psi}^\dagger_{\boldsymbol{r}} \begin{pmatrix} 0 & w^*_{\boldsymbol{r}} \sigma_y \\ w_{\boldsymbol{r}} \sigma_y & 0 \end{pmatrix} \hat{\Psi}_{\boldsymbol{r}} \tag{9.8}$$

for the $\mathrm{A_1}$ mode [184]. Here $\boldsymbol{u}_{\boldsymbol{r}}$ and $w_{\boldsymbol{r}}$ represent an atomic displacement field for each mode. The parameters $F_{\mathrm{A_1}}$ and F_{LO} ($F_{\mathrm{LO}} = F_{\mathrm{A_1}}/\sqrt{2}$) are the corresponding force constants for intervalley and intravalley scattering, respectively. In Eq.(9.7), the zone-center displacement field $\boldsymbol{u}_{\boldsymbol{r}}$ caused by the LO phonon mode is given by

$$\boldsymbol{u}_{\boldsymbol{r}} = \sum_{\boldsymbol{q}_{\mathrm{ph}}} \sqrt{\frac{1}{S\rho\,\omega_{\boldsymbol{q}_{\mathrm{ph}},\mathrm{LO}}}} \left(\hat{b}_{\boldsymbol{q}_{\mathrm{ph}},\mathrm{LO}} \boldsymbol{e}_{\boldsymbol{q}_{\mathrm{ph}}} + \hat{b}^\dagger_{-\boldsymbol{q}_{\mathrm{ph}},\mathrm{LO}} \boldsymbol{e}_{-\boldsymbol{q}_{\mathrm{ph}}} \right) e^{i\boldsymbol{q}_{\mathrm{ph}} \cdot \boldsymbol{r}}, \tag{9.9}$$

where ρ is the mass density of graphene, $\omega_{\mathbf{q},\mathrm{LO}}$ is the phonon mode frequency, and $\boldsymbol{e}_{\boldsymbol{q}_{\mathrm{ph}}} = (q_x, q_y)/|\boldsymbol{q}|$ is the LO polarization vector of the phonon amplitude. The zone-boundary distortion $w_{\boldsymbol{r}}$ in Eq.(9.8) induced by the $\mathrm{A_1}$ phonon mode is given by

$$w_{\boldsymbol{r}} = \sum_{\boldsymbol{q}_{\mathrm{ph}}} \sqrt{\frac{1}{S\rho\omega_{\boldsymbol{q}_{\mathrm{ph}},\mathrm{K}}}} \left(b_{\boldsymbol{q}_{\mathrm{ph}},\mathrm{K}} + b^\dagger_{-\boldsymbol{q}_{\mathrm{ph}},\mathrm{K}'} \right) e^{i\boldsymbol{q}_{\mathrm{ph}} \cdot \boldsymbol{r}}, \tag{9.10}$$

and couples eigenstates from valley K to eigenstates of valley K′ [184].

The electron-disorder coupling is sensitive to the type of defects present in graphene. In general, defects can be categorized into intrinsic and extrinsic. Intrisic sources of disorder in graphene include ripples and topological defects. Extrinsic disorder include adatoms, vacancies, charged defects and extended defects (edges). Furthermore, disorder can couple to electronic states in two different ways. The first is a local change in the single site energy. On-site disorder acts as a local chemical potential change which shifts the position of the Dirac point. Within the tight-binding description,

on-site disorder can be expressed as

$$\mathcal{H}_{\mathrm{d}} = \sum_i U_{i,A}\, c^\dagger_{i,A} c_{i,A} + U_{i,B}\, c^\dagger_{i,B} c_{i,B}, \tag{9.11}$$

where $U_{i,\alpha}$ is the strength of the disorder potential at position $\boldsymbol{r}_{i,\alpha}$. Note that the matrix elements are diagonal in the sublatttice indices. Within the effective Hamiltonian description, on-site disorder can be written as

$$\mathcal{H}_d = \int_S d\boldsymbol{r} \Psi^\dagger_{\boldsymbol{r}} \begin{pmatrix} U_{\boldsymbol{r},A} & 0 & \tilde{U}_{\boldsymbol{r},A} & 0 \\ 0 & U_{\boldsymbol{r},B} & 0 & \tilde{U}_{\boldsymbol{r},B} \\ \tilde{U}^*_{\boldsymbol{r},A} & 0 & U'_{\boldsymbol{r},A} & 0 \\ 0 & \tilde{U}^*_{\boldsymbol{r},B} & 0 & U'_{\boldsymbol{r},B} \end{pmatrix} \Psi_{\boldsymbol{r}}, \tag{9.12}$$

with intravalley components $U_{\boldsymbol{r},\alpha}$ at the K-point and $U'_{\boldsymbol{r},\alpha}$ at the K$'$ point, and intervalley components $\tilde{U}_{\boldsymbol{r},\alpha}$. Intervalley components are only relevant if the defect is short-ranged in the unit cell length scale; in this case, the defect can transfer a large momentum to the scattered electrons on the order of $1/a_0$.

A second type of disorder is one that changes the distance or angles between the p_z orbitals, thus affecting the hopping amplitude. These potentials are expressed via the off-diagonal elements in Eq.(9.12). Structural defects of the honeycomb lattice, such as pentagons, heptagons, or combinations of these defects (i.e. Stone-Wales defects [185]), induce long-range deformations which modify electron trajectories. In general, these defects can be accounted for by the introduction of a vector and scalar potential in the Dirac Hamiltonian.

9.3 Phase interference effects: phonon momentum selectivity and relevant diagrams

Although the D and D$'$ bands probe phonons with general $\boldsymbol{q} \neq 0$, and several diagrams need to be considered for the calculation of the matrix $\mathcal{M} = \sum_p \mathcal{M}_p$ in Eq.(9.1);

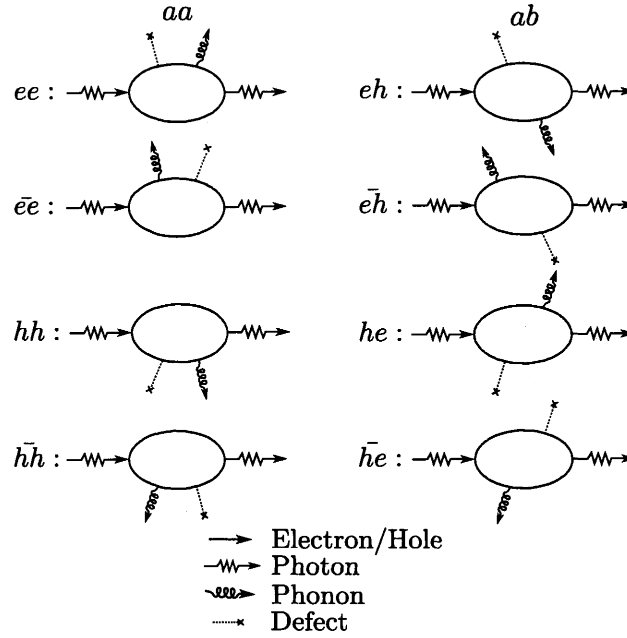

Figure 9-2: Feynman diagrams contributing to the double resonant Raman scattering process. The notation ab ($\bar{a}b$) indicates that the particle a ($a = e, h$) is scattered first by a defect (phonon), and particle b ($b = e, h$) is scattered next by a phonon (defect), and where e (h) stands for electron (hole).

only a very small region of phonon phase space and a small number of diagrams contribute dominantly to the Raman intensity. In particular, numerical calculations have previously shown that the Raman cross section is mostly due to a very small region in phonon phase space associated with the backscattering of the resonant photoexcited electron-hole pair [160] [see Fig.9-3(a)] and, additionally, dominated by the ab diagrams [174] in the right column of Fig.9-2 [see Fig.9-3(c)]. These two results were explained in terms of the so-called phase interference effects [160, 174]. In this section, I quantitatively analyze these interference effects, which will allow us to significantly simplify the analytical calculation of I_{DR} in Eq.(9.1).

The fact that back-scattering of the photoexcited electron-hole pair dominates the Raman cross-section is not straight-forward to obtain only by inspection of Eqs.(9.2) and (9.3). A simple phase-space argument allows us to anticipate that two regions of phonon phase space are relevant, namely, $|\boldsymbol{q}| \sim 0$, and $|\boldsymbol{q}| \sim E_{\rm L}/v_{\rm F}$ [see Fig.9-3(a)-(b)]. When $|\boldsymbol{q}| \sim 0$, then a large number of electronic states with wave vector $|\boldsymbol{k}| = E_{\rm L}/2v_{\rm F}$ in Eqs.(9.2) and (9.3) are doubly resonant, which may lead to a pro-

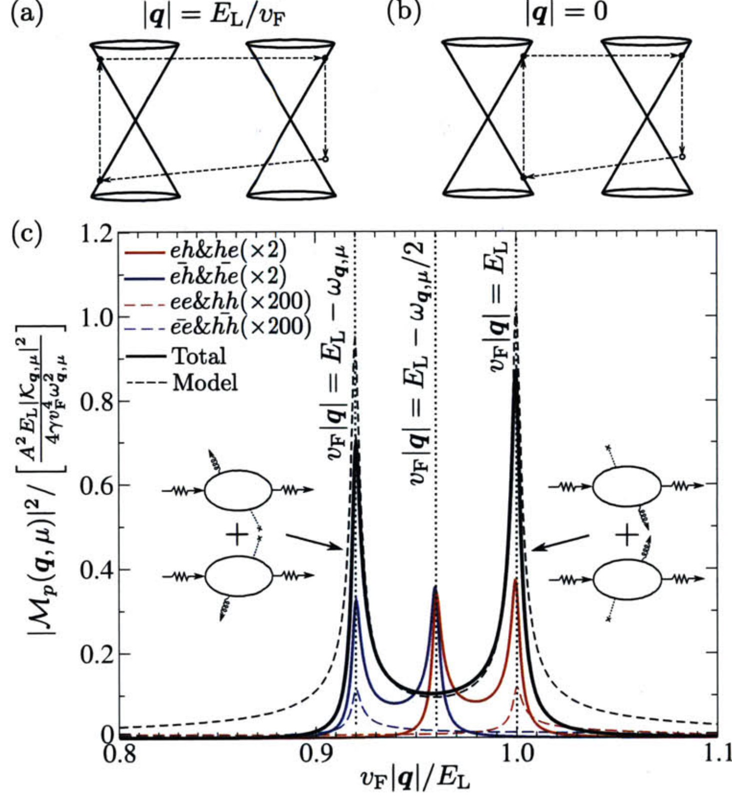

Figure 9-3: Dominant phonon modes contributing to the Raman peak. Because of phase interference effects, only a small region of phonon phase space and a small number of diagrams in Fig.9-2 contribute dominantly to the Raman probability. For instance, (a) back-scattering of the photoexcited electron-hole pair by a phonon with momentum $\boldsymbol{q}_{\rm ph} = \mathbf{K} + \boldsymbol{q}$, where $|\boldsymbol{q}| = E_{\rm L}/v_{\rm F}$, provides a significantly larger contribution to the D-band Raman intensity than (b) forward scattering with $|\boldsymbol{q}| = 0$. [160] (c) The contribution to the Raman matrix element $|\mathcal{M}|^2 = |\sum_p \mathcal{M}_p|^2$ (black lines) is mainly due to ab diagrams (colored solid lines) shown in the right column of Fig.9-2. [174] On the contrary, aa diagrams (colored dashed lines) have matrix elements $|\mathcal{M}_p|^2$ smaller than those of ab processes by a factor of $(\omega_{\boldsymbol{q},\beta}/2E_{\rm L})^2$. At $v_{\rm F}|\boldsymbol{q}| = E_{\rm L}$, for example, both the eh and he diagrams provide the dominant contribution and, thus, $|\sum_p \mathcal{M}_p|^2$ is approximately four times the value of $\mathcal{M}_{eh}$. Note also the cancellation of the peaks at $v_{\rm F}|\boldsymbol{q}| = E_{\rm L} - \omega_{\boldsymbol{q},\beta}/2$, where all four ab diagrams interfere destructively. The black dashed curve is obtained within our model from Eq.(9.13), valid only in the vicinity of each peak.

portionately large scattering amplitude. Alternatively, I note that the DR condition can only be met at some point in electronic $\boldsymbol{k}$ space when $|\boldsymbol{q}| \leq E_{\rm L}/v_{\rm F}$. Therefore, when $|\boldsymbol{q}| \sim E_{\rm L}/v_{\rm F}$, a singular behavior in the density of states between the photoexcited state and the back-scattered state is obtained. As shown in Sec.9.4.1, after performing the $\boldsymbol{k}$-variable integration in Eqs.(9.2) and (9.3), I obtain a significantly larger value of $|\mathcal{M}(|\boldsymbol{q}| \sim E_{\rm L}/v_{\rm F}, \beta)|^2$ compared to $|\mathcal{M}_p(\boldsymbol{q} \to 0, \beta)|^2$ by a factor of $\omega_{\boldsymbol{q},\beta}^2 \gamma / E_{\rm L}^3 \sim 10^{-5}$.

Similarly to the G$'$ band, *ab* diagrams play an important role in the Raman intensity of the D and D$'$ bands, as was first pointed out by Venezuela *et at.* [174]. In Sec.9.4.1, I find that the poles in Eq.(9.2) are differently distributed in the upper and lower complex planes from those of Eq.(9.3), resulting in a matrix element $\mathcal{M}_p$ for *ab* processes larger than those for *aa* processes by a factor $\sim \omega_{\boldsymbol{q},\beta}/2E_{\rm L}$, as shown in Fig.9-3. Thus, failure to include *ab* processes in the Raman calculations leads to a Raman intensity reduced by a factor $(\omega_{\boldsymbol{q},\beta}/2E_{\rm L})^2 \sim 10^{-3}$.

A final simplification in the Raman intensity calculation is possible. As shown in Fig.9-3(c), if I consider in detail the resonance conditions in the denominators of Eq.(9.3), I find that the matrix elements $\mathcal{M}_{eh}(\boldsymbol{q}, \beta)$ is peaked exactly at $v_{\rm F}|\boldsymbol{q}| = E_{\rm L}$ (so-called incident light-resonance) and at $v_{\rm F}|\boldsymbol{q}| = E_{\rm L} - \omega_{\boldsymbol{q},\beta}/2$ (here both the first and third intermediate states in Eq.(9.3) are at resonance with the photon). A similar conclusion holds for the *he* diagram. Alternatively, for $e\bar{h}$ and $\bar{h}e$, the peak in the matrix element occurs at $v_{\rm F}|\boldsymbol{q}| = E_{\rm L} - \omega_{\boldsymbol{q},\beta}/2$ and $v_{\rm F}|\boldsymbol{q}| = E_{\rm L}$ (scattered light resonance). Therefore, close to the wavevector $v_{\rm F}|\boldsymbol{q}| \approx E_{\rm L}$ ($v_{\rm F}|\boldsymbol{q}| \approx E_{\rm L} - \omega_{\boldsymbol{q},\beta}$), only the diagrams $\mathcal{M}_{eh} + \mathcal{M}_{he}$ ($\mathcal{M}_{e\bar{h}} + \mathcal{M}_{\bar{h}e}$) need to be calculated. In contrast, the large contribution produced by *each* of the four *ab* diagrams at $v_{\rm F}|\boldsymbol{q}| = E_{\rm L} - \omega_{\boldsymbol{q},\beta}/2$ interfere destructively, as shown in Fig.9-3 and discussed in Sec. 9.4.1.

9.4 Integrated Raman intensity

The two-peak shape of the Raman scattering matrix shown in Fig.9-3 and originating from the diagrams $eh + he$ at $v_{\rm F}|\boldsymbol{q}| = E_{\rm L}$, and from $e\bar{h} + \bar{h}e$ at $v_{\rm F}|\boldsymbol{q}| = E_{\rm L} - \omega_{\boldsymbol{q},\beta}$,

significantly simplifies the calculation of the integrated Raman intensity, since it is now only necessary to study $\mathcal{M}(\boldsymbol{q},\beta)$ in the close vicinity of these peaks. For this purpose, I calculate $\mathcal{M}_{eh}(\boldsymbol{q},\beta)+\mathcal{M}_{he}(\boldsymbol{q},\beta)$ for wavevectors $|\boldsymbol{q}| = E_{\rm L}/v_{\rm F}+\delta q$, with $|\delta q| \ll \omega_{\boldsymbol{q},\beta}/v_{\rm F}$. Calculation of $\mathcal{M}_{e\bar{h}}(\boldsymbol{q},\beta)+\mathcal{M}_{\bar{h}e}(\boldsymbol{q},\beta)$ can be done analogously. As shown in Sec. 9.4.1, we find that $\mathcal{M}_{eh}(\boldsymbol{q},\beta)$ is given by

$$\mathcal{M}_{eh}(\boldsymbol{q},\beta) = -\frac{iA\mathcal{K}_{\boldsymbol{q},\beta}}{8v_{\rm F}^2\omega_{\boldsymbol{q},\beta}}\sqrt{\frac{2E_{\rm L}}{(v_{\rm F}|\boldsymbol{q}|-E_{\rm L})+i\gamma/2}}, \tag{9.13}$$

where $\mathcal{K}_{\boldsymbol{q},\beta}$ is the product of the four matrix elements in the numerator of Eq.(9.3) with initial wave vector $\boldsymbol{k} = -\boldsymbol{q}/2$, so that the electron-phonon interaction couples electronic states with momentum $\boldsymbol{q}/2$ and $-\boldsymbol{q}/2$. Specifically, the value of $\mathcal{K}_{\boldsymbol{q},\beta}$ is given by

$$\mathcal{K}_{\boldsymbol{q},\beta} = \sum_{s,j}\frac{2\pi(ev_{\rm F})^2F_\beta\mathcal{U}^e_{\boldsymbol{q},\beta}[\boldsymbol{e}_{\boldsymbol{Q}_{\rm d}\lambda_{\rm i}}\times\hat{\boldsymbol{q}}]_z[\boldsymbol{e}^*_{\boldsymbol{Q}_{\rm f}\lambda_{\rm f}}\times\hat{\boldsymbol{q}}]_z e^{-i\boldsymbol{q}\cdot\boldsymbol{r}_j}}{VE_{\rm L}\sqrt{S^3\rho\omega_{\boldsymbol{q},\beta}}}, \tag{9.14}$$

where the term $\mathcal{U}^e_{\boldsymbol{q},\beta}$ is the short-hand notation for the matrix element

$$\mathcal{U}^e_{\boldsymbol{q},\Gamma} = \langle\psi_{\boldsymbol{q}/2,+}|U_{\boldsymbol{q}}e^{i\boldsymbol{q}\cdot\boldsymbol{r}}|\psi_{-\boldsymbol{q}/2,+}\rangle, \quad \mathcal{U}^e_{\boldsymbol{q},{\rm K}} = \langle\psi'_{\boldsymbol{q}/2,+}|\tilde{U}_{\boldsymbol{q}}e^{i\boldsymbol{q}\cdot\boldsymbol{r}}|\psi_{-\boldsymbol{q}/2,+}\rangle. \tag{9.15}$$

Importantly, in Eq.(9.14), both valleys contribute to $\mathcal{M}_{eh}(\boldsymbol{q},\Gamma)$ for intravalley scattering, whereas only one valley contributes to $\mathcal{M}_p(\boldsymbol{q},{\rm K})$ for intervalley scattering; the creation of a phonon at the K-point allows an electronic transition from the K′ to the K point to occur, but not vice versa. A similar analysis can be done for $\mathcal{M}_{he}(\boldsymbol{q},\beta)$, where hole scattering by the defects yields a matrix element $\mathcal{U}^h_{\boldsymbol{q},\beta}$, thereby resulting in a total defect scattering matrix element $\mathcal{U}_{\boldsymbol{q},\beta} = \mathcal{U}^e_{\boldsymbol{q},\beta}-\mathcal{U}^h_{\boldsymbol{q},\beta}$. Here the minus sign is due to an overall minus sign in the electron phonon matrix element, when hole scattering (as opposed to electron scattering) is considered.

In order to obtain the integrated Raman intensity, I sum $\mathcal{M}_{eh}(\boldsymbol{q},\beta)$ and $\mathcal{M}_{he}(\boldsymbol{q},\beta)$ and insert the sum in Eq.(9.4). In the regime of uncorrelated defects, it is valid to use $\sum_{j,j'}e^{i\boldsymbol{q}\cdot(\boldsymbol{r}_j-\boldsymbol{r}_{j'})}/A = n_{\rm d}$, where $n_{\rm d}$ is the defect concentration. Furthermore, because of the isotropic nature of the Dirac Hamiltonian, I can assume that $|\mathcal{U}_{\boldsymbol{q},\beta}|^2$ depends only on the modulus of the wave vector $\boldsymbol{q}$. Integration over all possible

phonon momenta and photon polarization directions, and considering detection of the backscattered photons, leads to the dimensionless Raman intensity

$$\frac{d\mathcal{I}^{\beta}_{\rm DR}}{d\Omega_{\rm f}} = \frac{g_\beta \alpha^2}{4}\frac{F_\beta^2}{\rho v_{\rm F}^2 \omega_{\boldsymbol{q},\beta}}\left(\frac{v_{\rm F}}{c}\frac{E_{\rm L}}{\omega_{\boldsymbol{q},\beta}}\right)^2 \frac{n_{\rm d}|\mathcal{U}_{\boldsymbol{q},\beta}|^2}{v_{\rm F}^2}\ln\left(\frac{\omega_{\boldsymbol{q},\beta}}{\gamma}\right), \tag{9.16}$$

for the D (β =K) and D′ ($\beta = \Gamma$) Raman processes, where $\alpha = e^2/c$ is the fine-structure constant, $|\boldsymbol{q}| = E_{\rm L}/v_{\rm F}$, and the prefactors $g_\Gamma = 2$ and $g_{\rm K} = 1$ appear due to the different electron and phonon valley indices that appear in the summations for intravalley and intervalley scattering processes, respectively (see details in Sec. 9.4.1).

9.4.1 Details of the Raman intensity calculations

Here I focus specifically on the calculation of the *ee* and *eh* diagrams in Fig.9-2. Extension to the remaining processes is straight-forward. First I consider the most relevant case of backscattering of the photoexcited electron-hole pair due to the production of a phonon with wavevector $\boldsymbol{q}_{\rm ph} = \boldsymbol{q}_\beta + \boldsymbol{q}$ ($\beta = \Gamma$, K), where $|\boldsymbol{q}| \approx E_{\rm L}/v_{\rm F}$, $\boldsymbol{q}_\Gamma = 0$ and $\boldsymbol{q}_{\rm K} = \mathbf{K}$. Afterwards, I show that forward-scattering of the photoexcited electron-hole pair (i.e., $|\boldsymbol{q}| = 0$) provides a negligible contribution to the total intensity (this is shown rigorously for nanotubes in Ref. [160]).

Backscattering: $v_{\rm F}|\boldsymbol{q}| = E_{\rm L}$

I evaluate first the matrix element $\mathcal{M}_p(\boldsymbol{q},\beta)$ for a value of $|\boldsymbol{q}| = E_{\rm L}/v_{\rm F} + \delta q$, where $|\delta q| \ll \omega_{\boldsymbol{q},\beta}/v_{\rm F}$. Given that trigonal warping effects are neglected, I can arbitrarily align the k_x direction in the integrals in Eqs.(9.2) and (9.3) with $\boldsymbol{q}$, as shown in Fig.9-4. Under the assumption $\gamma \ll \omega_{\boldsymbol{q},\beta} \ll E_{\rm L}$, which is the typical situation in experiments, most of the contribution to $\mathcal{M}_p(\boldsymbol{q},\beta)$ comes from the electronic phase-space region in the vicinity of the point $\boldsymbol{k} \approx -\boldsymbol{q}/2$ (shaded regions in Fig.9-4). Given the small region of phase space that needs to be considered, I: (a) expand to leading order in the vicinity of $\boldsymbol{k} = -\boldsymbol{q}/2$ the three functions in the denominators of Eqs.(9.2) and (9.3); (b) evaluate the matrix elements at $\boldsymbol{k} = -\boldsymbol{q}/2$; (c) perform the $\boldsymbol{k}$-space

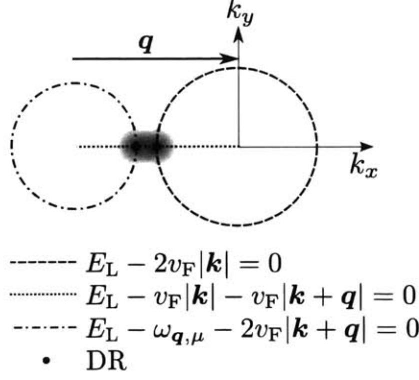

Figure 9-4: Momenta where the double resonance conditions are satisfied. Indicated are the resonance conditions for each of the terms in the denominator of Eq.(9.3), for the case $|\boldsymbol{q}| = E_{\mathrm{L}}/v_{\mathrm{F}}$. The shaded regions indicate the volume of electronic phase space $\boldsymbol{k}$ that mostly contributes to the scattering amplitude.

integration.

After carrying out the steps (a) and (b) above, and conveniently normalizing the integrals in Eqs.(9.2) and (9.3), one can then obtain

$$\mathcal{M}_p(\boldsymbol{q}, \beta) \approx \frac{A\mathcal{K}_{\boldsymbol{q},\beta}}{8\pi^2 v_{\mathrm{F}}^2 E_{\mathrm{L}}} \times \mathcal{I}_{\pm}\left(\frac{v_{\mathrm{F}}\delta q}{E_{\mathrm{L}}}\right), \tag{9.17}$$

where $\mathcal{I}_{\pm}(\xi)$ is given by

$$\begin{aligned}\mathcal{I}_{\pm}(\xi) = \; & \pm\int_{-\infty}^{\infty} dx \int_{-\infty}^{\infty} dy \frac{1}{(-\xi - \omega_{\boldsymbol{q},\beta}/E_{\mathrm{L}} \pm x - i\epsilon)} \\ & \times \frac{1}{(-\xi - 2y^2 - i\epsilon)(-\xi + x - i\epsilon)},\end{aligned} \tag{9.18}$$

and $\mathcal{K}_{\boldsymbol{q},\beta}$ is described in Eq.(9.14). The + (−) sign in Eq.(9.18) corresponds to the *ee* (*eh*) process, and $\epsilon = \gamma/2E_{\mathrm{L}} \ll 1$.

The positions of the poles in the x variable are distributed differently in the upper and lower-half planes for the $\mathcal{I}_{\pm}$ integrals, which results in $|\mathcal{I}_{+}| \ll |\mathcal{I}_{-}|$ (i.e., the dominant contribution comes from *eh* processes). In particular, calculation of $\mathcal{I}_{-}$ in Eq.(9.18) yields

$$\mathcal{I}_{-}(\xi) = -\frac{i\pi^2 E_{\mathrm{L}}}{\omega_{\boldsymbol{q},\beta}}\sqrt{\frac{2}{\xi + i\epsilon}}. \tag{9.19}$$

On the other hand, for the *ee* process, $\mathcal{I}_{+} = 0$ is obtained when using the approximations discussed above. However, the leading-order correction to $\mathcal{I}_{+}$ can be estimated

to be order $\mathcal{I}_+(0)/\mathcal{I}_-(0) \sim -i(\omega_{\boldsymbol{q},\beta}/2E_{\rm L})$, which is consistent with the numerical results in Fig.9-3. Therefore, the *aa* diagrams lead to a substantially smaller scattering amplitude $\sim (\omega_{\boldsymbol{q},\beta}/2E_{\rm L})^2$ when compared to the *ab* diagrams, and this feature was previously pointed out in the work by Venezuela *et al.* [174]. Inserting $\mathcal{I}_-$ into Eq.(9.17) yields Eq.(9.13).

At $v_{\rm F}|\boldsymbol{q}| = E_{\rm L}$, the *he* process also contributes strongly to the Raman intensity, while all remaining *ab* processes provide a small contribution ($e\bar{h} + \bar{h}e$ are peaked at $v_{\rm F}|\boldsymbol{q}| = E_{\rm L} - \omega_{\boldsymbol{q},\beta}$). In order to calculate the integrated Raman intensity, I insert $\mathcal{M}_{eh}(\boldsymbol{q},\beta) + \mathcal{M}_{he}(\boldsymbol{q},\beta)$ into Eq.(9.4) to obtain

$$\frac{d\mathcal{I}^{\beta}_{\rm DR}}{d\Omega_{\rm f}} = \frac{g_\beta \alpha^2}{16}\frac{F^2_\beta}{\rho v^2_{\rm F}\omega_{\boldsymbol{q},\beta}}\frac{v^2_{\rm F}}{c^2}\sum_{\boldsymbol{q},\lambda_{\rm f}}\frac{n_{\rm d}|\mathcal{U}_{\boldsymbol{q},\beta}|^2}{A\omega^2_{\boldsymbol{q},\beta}}\frac{E_{\rm L}|\boldsymbol{e}_{\boldsymbol{Q}_{\rm i}\lambda_{\rm i}} \times \hat{\boldsymbol{q}}|^2|\boldsymbol{e}^*_{\boldsymbol{Q}_{\rm f}\lambda_{\rm f}} \times \hat{\boldsymbol{q}}|^2}{\sqrt{(v_{\rm F}|\boldsymbol{q}| - E_{\rm L})^2 + (\gamma/2)^2}}. \tag{9.20}$$

Here, $\alpha = e^2/c$ is the fine-structure constant, $g_\Gamma = 2$, $g_{\rm K} = 1$, and where I used the assumption of uncorrelated defects with a concentration $n_{\rm d}$. Different prefactors g_β appear for intravalley and intervalley processes because, for zone-center phonons, both valleys contribute to $\mathcal{K}_{\boldsymbol{q},\beta}$, as discussed in the main text, while for zone-boundary phonons, only one valley contributes to *each* phonon mode in the vicinity of the K and K′ points.

Integration over momentum space $\boldsymbol{q}$ in Eq.(9.20) can be done in the vicinity of a ring of radius $E_{\rm L}/v_{\rm F}$ and angular direction $\varphi_{\boldsymbol{q}}$. Thus, I use polar coordinates $\sum_{\boldsymbol{q}} \approx (A/2\pi)\int d(\delta q)\int d\varphi_{\boldsymbol{q}}(E_{\rm L}/v_{\rm F})$. Furthermore, I assume normal and unpolarized incident photons, and detection in both polarization directions. Then, the angular integration of Eq.(9.20) yields

$$\sum_{\lambda_{\rm f}}\int\frac{d\varphi_{\boldsymbol{q}}}{2\pi}|\boldsymbol{e}_{\boldsymbol{Q}_{\rm i}\lambda_{\rm i}} \times \hat{\boldsymbol{q}}|^2|\boldsymbol{e}^*_{\boldsymbol{Q}_{\rm f}\lambda_{\rm f}} \times \hat{\boldsymbol{q}}|^2 = \frac{1+\cos^2\varphi_{\rm f}}{2}, \tag{9.21}$$

where $\varphi_{\rm f}$ is the angle of the outgoing photon with respect to the normal to the graphene sheet. Detection in the backscattering configuration (i.e., $\varphi_{\rm f} = \pi$) is assumed in this work. The radial integration of Eq.(9.20), using a cutoff in the phonon momentum of $\sim \omega_{\boldsymbol{q},\beta}/2v_{\rm F}$, which is the region of validity of Eq.(9.19) (see Fig.9-3),

yields half the value of the integrated Raman intensity of Eq.(9.16). The other half of the value of the integrated Raman intensity comes from considering the peak at $v_{\rm F}|\boldsymbol{q}| = E_{\rm L} - \omega_{\boldsymbol{q},\beta}$ from the $e\bar{h} + \bar{h}e$ diagrams.

I finally note that the peak at $v_{\rm F}|\boldsymbol{q}| = E_{\rm L} - \omega_{\boldsymbol{q},\beta}/2$ provides a negligible contribution to $\sum_p \mathcal{M}_p$, as shown in Fig.9-3. In this case, the large contribution of $\mathcal{M}_{eh}$ cancels that of $\mathcal{M}_{e\bar{h}}$ when each term is calculated separately as in Eqs.(9.17) and (9.18). Similarly, the contribution $\mathcal{M}_{he}$ cancels that of $\mathcal{M}_{\bar{h}\bar{e}}$, yielding a negligible value of $\mathcal{M} = \sum_p \mathcal{M}_p$.

Forward-Scattering: $\mathbf{q} = 0$

Forward-scattering [Fig.9-3(b)] provides a negligible contribution to the D and D′-band intensities because of the small scattering amplitude when compared to those associated with the backward scattering case, $v_{\rm F}|\boldsymbol{q}| = E_{\rm L}$. To show this point, I compute the matrix element $\mathcal{M}_{eh}(\boldsymbol{q} \to 0, \Gamma)$ for the zone-center phonon mode, which is given by

$$\mathcal{M}_{eh}(\boldsymbol{q} \to 0, \Gamma) = \int_0^\infty dk \int_0^{2\pi} d\varphi \frac{S(k/2\pi) \cdot \mathcal{K}_{\boldsymbol{q}\to 0,\Gamma}(\varphi_{\boldsymbol{k}})}{(E_{\rm L} - \omega_{\boldsymbol{q},\beta} - 2v_{\rm F}k - i\gamma/2)(E_{\rm L} - 2v_{\rm F}k - i\gamma/2)^2}, \tag{9.22}$$

and where $\mathcal{K}_{\boldsymbol{q}\to 0,\Gamma}(\varphi_{\boldsymbol{k}})$ is

$$\mathcal{K}_{\boldsymbol{q}\to 0,\Gamma}(\varphi_{\boldsymbol{k}}) = -\sum_{s,j} \frac{2\pi(ev_{\rm F})^2 F_\Gamma \, \mathcal{U}_{\boldsymbol{q}=0,\Gamma} \sin(\varphi_{\boldsymbol{k}}) \, [\boldsymbol{e}_{\boldsymbol{Q}_{\rm i}\lambda_{\rm i}} \times \hat{\boldsymbol{\varphi}}]_z [\boldsymbol{e}^*_{\boldsymbol{Q}_{\rm f}\lambda_{\rm f}} \times \hat{\boldsymbol{\varphi}}]_z e^{-i\boldsymbol{q}\cdot\boldsymbol{r}_j}}{V E_{\rm L} \sqrt{S^3 \rho \, \omega_{\boldsymbol{q},\beta}}}. \tag{9.23}$$

In Eqs.(9.22) and (9.23), $\varphi_{\boldsymbol{k}}$ was chosen to be the angle beween the $\boldsymbol{k}$-vector and the atomic displacement $\boldsymbol{u}$, and $\hat{\boldsymbol{\varphi}} = [\cos(\varphi_{\boldsymbol{k}}), \sin(\varphi_{\boldsymbol{k}})]$. Integration of the radial and angular components of Eq. (9.23) yields

$$\mathcal{M}_{eh}(\boldsymbol{q} \to 0, \Gamma) = \frac{S \langle \mathcal{K}_{\boldsymbol{q}\to 0,\Gamma} \rangle_\varphi \mathcal{L}_k}{4 E_{\rm L} v_{\rm F}^2}, \tag{9.24}$$

where $\langle \mathcal{K}_{\boldsymbol{q}\to 0,\Gamma}\rangle_{\varphi} = \int (d\varphi_{\boldsymbol{k}}/2\pi)\mathcal{K}_{\boldsymbol{q}\to 0,\Gamma}(\varphi_{\boldsymbol{k}})$, and $\mathcal{L}_k$ is

$$\mathcal{L}_k = \frac{E_{\rm L}}{\omega_{\boldsymbol{q},\beta}}\left[1 - \frac{E_{\rm L} - \omega_{\boldsymbol{q},\beta} - i\frac{\gamma}{2}}{\omega_{\boldsymbol{q},\beta}}\ln\left(\frac{E_{\rm L} - i\frac{\gamma}{2}}{E_{\rm L} - \omega_{\boldsymbol{q},\beta} - i\frac{\gamma}{2}}\right)\right]. \tag{9.25}$$

Considering the case $\gamma \ll \omega_{\boldsymbol{q},\beta} \ll E_{\rm L}$, then $\mathcal{L}_k \approx 1$. By comparing Eq.(9.24) with Eq.(9.19), I conclude that $|\mathcal{M}_{eh}(\boldsymbol{q} \to 0, \Gamma)|^2$ is a factor of order $\omega^2_{\boldsymbol{q},\beta}\gamma/E^3_{\rm L} \sim 10^{-5}$ smaller than $|\mathcal{M}_{eh}(|\boldsymbol{q}| = E_{\rm L}/v_{\rm F}, \Gamma)|^2$ at backscattering, for typical values $\gamma \sim 10\,\text{meV}$.

9.4.2 Comparison with experiments

Several experiments measured the Raman intensity ratio $I_{\rm D}/I_{\rm G}$ as a function of laser energy [158, 159, 169, 170]. The dependence of $\mathcal{I}_{\rm DR}$ on $E_{\rm L}$ in Eq.(9.16) is affected by several factors: (i) the resonant electronic and phonon phase space increases at larger values of photon energies; (ii) $\omega_{\boldsymbol{q},\beta}$ varies as the laser energy is changed because of the dispersive behavior of the D and D′ bands; (iii) the broadening γ depends on the energy of the resonant photoexcited electron hole pairs and, in the simplest case, γ behaves as $\gamma \propto E_{\rm L}$; [181] (iv) the Raman process selects specific Fourier components $|\mathcal{U}_{\boldsymbol{q},\beta}|^2$ of the scattering potential, with $|\boldsymbol{q}| = E_{\rm L}/v_{\rm F}$. Although (i) and (ii) are factors associated with the intrinsic properties of graphene, (iii) and (iv) are extrinsic and explain why different dependencies of the D-band intensity on laser energy are measured experimentally under different sample conditions.

Considering a linear dependence of the inverse electronic lifetime with laser energy, and the dispersion relation of the A_1 phonon mode close to the K point, I plot in Fig.9-1 the intensity ratio $I_{\rm D}/I_{\rm G}$ as a function of $E_{\rm L}$ for point-like defects (i.e., $|\mathcal{U}_{\boldsymbol{q},\beta}|^2$ is taken as independent of $\boldsymbol{q}$). The analytical results are compared with the experimental integrated Raman intensity from Ref. [158]. For the $I_{\rm G}$ Raman intensity, I use the standard textbook dependence $I_{\rm G} \propto E^4_{\rm L}$, [178] and typical values for the electronic broadening $\gamma \sim 0.03E_{\rm L}$. [181] Even within the simplifying assumptions made in the model, there is good agreement between theory and the experiments.

Furthermore, it is interesting to note that, from Eq.(9.16), the disorder-induced D and D′-band intensities do not necessarily have the same dependence on $E_{\rm L}$. In

fact, recent experimental measurements [170] have shown that the ratio $I_{D'}/I_D$ is a slowly increasing function of laser energy. If we consider point-like defects and taking into account that $\gamma \ll \omega_{\boldsymbol{q},\beta}$, then the ratio $I_{D'}/I_D$ obtained from Eq.(9.16) verifies $I_{D'}/I_D \propto (\omega_{\boldsymbol{q},K}/\omega_{\boldsymbol{q},\Gamma})^3$, where $|\boldsymbol{q}| = E_L/v_F$. Because the A_1 phonon mode near the K point is more dispersive than the LO phonon mode near the Γ point, then the ratio $I_{D'}/I_D$ obtained from theory is a slowly increasing function of laser energy, which is in agreement with the experiments.

I finally consider the dependence of the integrated Raman intensity on defect concentration n_d. Within the model in Eq.(9.16), two regimes exist: (i) when the defect concentration n_d is low enough such that the electron-phonon induced linewidth $\gamma_{ep} \sim 15\,\text{meV}$ [181] is larger than the defect induced linewidth γ_{ed}, then $I_D \propto n_d$; (ii) however, when n_d is sufficiently large such that $\gamma_{ed} > \gamma_{ep}$, then γ is sensitive to defect concentration n_d and a non-linear dependence of $\mathcal{I}_{DR}$ as a function of n_d is obtained. The threshold value of n_d separating both regimes can be estimated by calculating the defect-induced broadening of the electronic states at $\varepsilon_{\boldsymbol{k},+} \sim E_L/2$, assuming uncorrelated short-range defects with a potential strength $|\mathcal{U}_{\boldsymbol{q},\beta}| = U_0$. A straight-forward calculation yields $\gamma_{ed} = n_d|U_0|^2 E_L/2v_F^2$. Taking $U_0 \sim 1\,\text{eV}\cdot\text{nm}^2$ and $E_L \sim 2\,\text{eV}$, then the condition $\gamma_{ep} \sim \gamma_{ed}$ is met at defect concentrations of $n_d \sim 10^{12}\,\text{cm}^{-2}$.

In order to compare with experimental measurements, the dependence of I_D on n_d is plotted in Fig.9-1(b) together with the experimental data from Ref. [172]. Here I used $\gamma_{ep} \sim 15\,\text{meV}$ and $\gamma_{ed}[\text{meV}] \sim 10 \times n_d[10^{12}\text{cm}^{-2}]$. The theoretical model correctly captures the saturating behavior of the D-band intensity, as obtained in experiments. However, it is beyond the scope of this work to describe the highly defective limit, such as that measured in Refs. [158, 159]. In this limit, the electronic states are localized within small grains formed, for instance, after intense ion irradiation and thus, the electronic states can no longer be described as eigenstates of the translational invariant system.

9.5 Discussion

The defect scattering potential plays an important role in determining the DR Raman intensity, as shown in Eq.(9.16). However, most models to date typically assume constant elastic scattering matrix elements. First, this is equivalent to assuming that defects can scatter electrons or holes with equal strength throughout the BZ. Second, this assumption neglects electronic phase factors associated with the sublattice and valley pseudospin degrees of freedom. For instance, whether the on-site component of the defect potential provides a significantly different contribution to the Raman intensity than the hopping component have not been addressed in the literature. Thus, further work on the analysis of the term $|\mathcal{U}_{\boldsymbol{q},\beta}|^2$, which conveniently appears as a numerical prefactor in Eq. (9.16), is necessary.

Experimental measurements for different types of defects have shown $I_{\mathrm{D}} \gg I_{\mathrm{D}'}$ [171]. By taking the ratio of Eq.(9.16) for the D and D′ bands, I obtain

$$\frac{I_{\mathrm{D}}}{I_{\mathrm{D}'}} \approx \frac{g_{\mathrm{K}}}{g_{\Gamma}} \frac{F_{\mathrm{K}}^2}{F_{\Gamma}^2} \left(\frac{\omega_{\boldsymbol{q},\Gamma}}{\omega_{\boldsymbol{q},\mathrm{K}}}\right)^3 \frac{|\mathcal{U}_{\boldsymbol{q},\mathrm{K}}|^2}{|\mathcal{U}_{\boldsymbol{q},\Gamma}|^2} \approx 2.2 \times \frac{|\mathcal{U}_{\boldsymbol{q},\mathrm{K}}|^2}{|\mathcal{U}_{\boldsymbol{q},\Gamma}|^2}. \tag{9.26}$$

Although theoretical calculations show $F_{\Gamma} < F_{\mathrm{K}}$ (or more precisely, $F_{\Gamma}/F_{\mathrm{K}} \approx 1/\sqrt{2}$ [184, 186, 187]), this small difference cannot account for the large intensity ratio observed experimentally. Additionally, the phonon frequencies verify $\omega_{\boldsymbol{q},\Gamma}/\omega_{\boldsymbol{q},\mathrm{K}} \approx 1.3$. Then, Eq.(9.26) suggests that the origin of $I_{\mathrm{D}}/I_{\mathrm{D}'} \gg 1$ is primarily due to the scattering potential term.

The fact that short-wave-vector intravalley scattering typically dominates over long-wave-vector intervalley scattering suggests that there is a contradiction between Eq.(9.26) and the typically measured relation $I_{\mathrm{D}}/I_{\mathrm{D}'} \gg 1$. In particular, when the defect potential has a finite range, the short-wave-vector scattering components of the matrix $U_{\boldsymbol{q},\Gamma}$ are expected to be larger than the long-wave-vector scattering components in $U_{\boldsymbol{q},\mathrm{K}}$. However, this does not necessarily mean $|\mathcal{U}_{\boldsymbol{q},\mathrm{K}}| < |\mathcal{U}_{\boldsymbol{q},\Gamma}|$. Because graphene has internal pseudospin degrees of freedom, the internal phases of the photoexcited electron (or hole) and the backscattered electron (or hole) play an impor-

tant role. In particular, it is well-known from the behavior of the electronic transport of graphene that intravalley backscattering of Dirac electrons is strongly suppressed, [34, 35] thereby allowing $|\mathcal{U}_{\boldsymbol{q},\mathrm{K}}| > |\mathcal{U}_{\boldsymbol{q},\Gamma}|$ to be possible. Similar effects are expected to occur from the DR theory, where backscattering of the photoexcited electrons [see Fig.9-3(a)] makes the dominant contribution to the DR Raman intensity. Further theoretical work in this direction is necessary and should be the subject of future studies.

Using Raman spectroscopy to identify the nature of the defects may have attractive applications in the characterization of real graphene samples. For instance, it has been previously found [180] that the edge-induced D-band intensity scales with laser energy as $I_{\mathrm{D}} \propto E_{\mathrm{L}}\ln(\omega_{\boldsymbol{q},\mathrm{K}}/\gamma)$, which is significantly different from the dependence found in Eq.(9.16). Therefore, our result suggests a way to distinguish the edge-induced D band from the disorder-induced D band. Alternatively, defects with different ranges may be distinguished between each other by the different wave-vector dependence of the term $|\mathcal{U}_{\boldsymbol{q},\beta}|^2$. In practice, however, extracting such information may be difficult given that several parameters in Eq.(9.16) change simultaneously with laser energy, thus making detailed experimental analysis rather complicated. It is more likely, however, that use of the ratio $I_{\mathrm{D}}/I_{\mathrm{D'}}$ is a more promising direction to identify the nature of defects, as suggested by Eckmann *et al.* [171]

9.6 Chapter summary

A detailed analytical study of the disorder-induced double resonant (DR) Raman process in graphene was presented in this chapter, and analytical expressions for the Raman probability $\mathcal{I}_{\mathrm{DR}}$ for the D and D′ bands are derived and discussed. Given the large number of parameters required to describe the DR process, this study succeeds in explicitly showing how the Raman intensities depend on laser energy, defect concentration, and electronic lifetime, within a single equation [Eq.(9.16)]. Furthermore, I here discussed quantitatively the so-called phase interference effects, [160,174] which determine the most important phonon wave vectors and Feynman diagrams

in Fig.9-2 that contribute to the DR Raman intensity. It was also found that the disorder-induced D-band Raman intensity has a different laser energy dependence than the edge-induced D band, [180] which could potentially be used to distinguish carrier scattering by boundaries from scattering due to lattice disorder.

Good agreement between our analytical results and experimental measurements is obtained. As observed experimentally, it is shown in this chapter that the D- and D′-band intensities have a different laser energy dependence [170] and, additionally, that each of these dependencies can vary with the type of defect [158, 159, 169, 170]. The saturating behavior of the $I_{\rm D}$ intensity with increasing defect concentrations measured in experiments [172, 173] is also discussed, and occurs when the defect collision rate is faster than the electron-phonon collision rate. Further theoretical work is required to better understand the role of the different parameters describing the defect scattering potential, such as the range and the various components associated with the electronic pseudo-spin degrees of freedom, on determining the $I_{\rm D}/I_{\rm D'}$ ratio. The value of this ratio could potentially make progress towards identifying the characteristic nature of specific defect types in graphene [171].

Chapter 10

Conclusions

Over twelve years have passed since graphene was first isolated. Despite the astronomical number of graphene papers which have been published in such a brief period of time, graphene does not cease to surprise us and undoubtedly still remains at the forefront of science. Two fronts of graphene research remain vigorously pursued: many-body physics in graphene and graphene-based electronic metamaterials. In this thesis, I emphasized the latter front.

In particular, I explored two special pathways of achieving novel electronic behaviors in graphene nanostructures: vertically stacking monolayers of insulating materials (Chapters 3-6), and the creation of local electrostatic potentials (Chapters 7-9). While the former allows *band structure engineering of graphene nanostructures*, the latter allows *real space manipulation of electronic states* in Dirac systems. The tunability of electron characteristics which can be achieved using both methodologies opens new possibilities to further advance the already-intriguing properties of bare graphene, with implications both in basic research as well as applied research. Next, I summarize the main results of this thesis and discuss possible extensions in the future.

Band structure engineering of graphene nanostructures—Stacking graphene in-between other 2D crystals has expanded the graphene field dramatically, well beyond bare graphene. Here I showed how the large array of available two-dimensional insulating materials enables the fabrication of electronic systems with pre-designed

band structure characteristics. This feature, which enables control of different vertical transport properties, is manifested by several device parameters which can be tuned independently: the Schottky potential can be engineered at the interface of graphene and an insulating material; resonances in the tunneling density of states can be induced by a twist angle between two graphene layers; electronic temperature can be locally controlled by shining light on graphene; interlayer separation between graphene layers can be engineered with few Å precision. As a result of all these tunable parameters, graphene nanostructures can be exploited for a wide range of applications, such as memory devices, photodetectors, solar harvesters, just to name a few.

In particular, stacked graphene nanostructures exhibit great potential for photoactive electronics. Indeed, vertical photoactive graphene nanostructures have various advantages over lateral photoactive graphene nanostructures. In the vertical case, the entire exposed surface area of graphene is being used to absorb and extract photon energy; this differs from graphene *pn* photodetectors where only a small region, e.g. the *pn* interface, participates in photon energy absorption. Vertically-stacked devices are also susceptible to optimization for different device applications. Furthermore, given that the transport distances for photoexcited carrier extraction are much smaller for vertical nanostructures ($\sim 1\,\mathrm{nm}$) than in lateral structures ($\sim 1\,\mu\mathrm{m}$), losses in vertically stacked systems are significantly smaller than in the lateral case. As a result, device sensitivities and efficiencies can be orders of magnitude larger.

The phase space of device parameter which can be tuned is enormous. Indeed, there are hundreds, if not thousands, of materials that can be potentially exfoliated to form monolayers. Although it is unrealistic to think that all possible material combinations and stacking orderings can be explored experimentally, it is crucial to chart the basic properties of the various interfaces between graphene and other 2D materials. For instance, the interface conductance, which depends on the bonding of graphene with other 2D materials, is known for only a few systems. The same applies to the Schottky barrier height. Material interfaces also induce extrinsic excitations, such as surface phonons, which contribute to energy losses. Such losses need to be

quantified for optimal device design. As such, plenty of work remains to be done in characterizing, mainly electronically and optically, relevant device parameters that are specially sensitive to interfaces.

Interactions in graphene nanostructures can also lead to other interesting behaviors. For instance, while our focus was on resonant, i.e. momentum-conserving, tunneling, many important device parameters, such as the maximum-achivable peak-to-valley ratio is sensitive to second-order processes. Examples of such processes include inelastic phonon-assisted tunneling or disorder-assisted tunneling. Also interesting is to explore novel electronic phases arising in graphene nanostructures by creating interfaces of contrasting materials. Importantly, several bulk superconducting materials as well as magnetic materials can be either exfoliated or synthesized with nanometer thicknesses.

Real space manipulation of electronic states—Besides tuning bandstructure characteristics in reciprocal space, electronic states in graphene can also be locally manipulated in real space. Local gates enable a finer control of the electron wavelength than the typical global gates. Local gates were here exploited to fabricate graphene quantum dots. The formation of graphene quantum dots, which was counterintuitive because of Klein tunneling, is induced by oblique reflection of electron waves at the *pn* interface.

I also made the important observation that graphene quantum dots are distinct from conventional quantum dots. In particular, the pseudospin degrees of freedom add new dimensions to graphene quantum dots. Because the electronic states in two-dimensional Dirac materials are exposed, graphene quantum dots provide, in practice, an ideal testbed to locally probe and manipulate pseudospins. In this direction, I showed that the Berry phase in graphene, which arises from the sublattice pseudospin, has striking manifestations on the quantum dot spectra, namely, it induces a giant non-reciprocal effect.

In addition, graphene electrons have a valley pseudospin. Using localized electronic states in graphene quantum dots can be a convenient path for the coherent control of the valley degree of freedom. This differs from the recently achieved valley-

Hall effect in graphene where delocalized valley currents develop at the edges.

Because of the ballistic transport in graphene at the micrometer scale, combined with graphene's linear electron dispersion, graphene is an ideal system for achieving electron-optics behavior. It is now also possible to pattern quantum dots in any shape and strength, enabling new systems in which to mimick electron optic behavior. In addition to the famous example of electron focusing, other phenomena of interest include chaotic behavior in non-integrable systems and interactions in double quantum dot systems.

Local gates can also lead to new interacting regimes in graphene quantum dots. An interesting scenario is the possibility of a pseudospin Kondo effect in Dirac quantum dots or to observe the Coulomb blockade effect. The study of excitonic states confined inside the Dirac quantum dot, where the particle lifetime is dramatically enhanced by exciton localization, is another promising pathway to pursue.

Many of the ideas explored here can potentially be implemented in other materials, such as topological insulators, Weyl semimetals or transition metal dichalcogenides. There are areas, however, where graphene will most likely remain irreplaceable. One such example is electron-optics behavior, given the high purity of current graphene samples. Another example is graphene-based photonics because of the unique photoresponse of graphene. Naturally, there is still plenty of room for graphene research. Graphene has excited the scientific community for over a decade now and hopefully new phenomena remains to be uncovered.

Bibliography

[1] K. S. Novoselov, A. K. Geim, S. V. Morozov, D. Jiang, Y. Zhang, S. V. Dubonos, I. V. Grigorieva, and A. A. Firsov. Electric field effect in atomically thin carbon films. *Science* **306**, 666 (2004).

[2] P. R. Wallace. The band theory of graphite. *Phys. Rev.* **71**, 622 (1947).

[3] J. W. McClure. Diamagnetism of graphite. *Phys. Rev.* **104**, 666 (1956).

[4] J. C. Slonczewski and P. R. Weiss. Band structure of graphite. *Phys. Rev.* **109**, 272 (1958).

[5] G. W. Semenoff. Condensed-matter simulation of a three-dimensional anomaly. *Phys. Rev. Lett.* **53**, 2449 (1984).

[6] E. Fradkin. Critical behavior of disordered degenerate semiconductors. ii. spectrum and transport properties in mean-field theory. *Phys. Rev. B* **33**, 3263 (1986).

[7] F. D. M. Haldane. Model for a quantum hall effect without Landau levels: Condensed-matter realization of the 'parity anomaly'. *Phys. Rev. Lett.* **61**, 2015 (1988).

[8] A. S. Mayorov, R. V. Gorbachev, S. V. Morozov, L. Britnell, R. Jalil, L. A. Ponomarenko, P. Blake, K. S. Novoselov, K. Watanabe, T. Taniguchi, and A. K. Geim. Micrometer-scale ballistic transport in encapsulated graphene at room temperature. *Nano Letters* **11**, 2396 (2011).

[9] T. Taychatanapat, K. Watanabe, T. Taniguchi, and P. Jarillo-Herrero. Electrically tunable transverse magnetic focusing in graphene. *Nat Phys* **9**, 225

(2013).

[10] A. S. Mayorov, D. C. Elias, I. S. Mukhin, S. V. Morozov, L. A. Ponomarenko, K. S. Novoselov, A. K. Geim, and R. V. Gorbachev. How close can one approach the Dirac point in graphene experimentally? *Nano Letters* **12**, 4629 (2012).

[11] K. S. Novoselov, Z. Jiang, Y. Zhang, S. V. Morozov, H. L. Stormer, U. Zeitler, J. C. Maan, G. S. Boebinger, P. Kim, and A. K. Geim. Room-temperature quantum Hall effect in graphene. *Science* **315**, 1379 (2007).

[12] H. Zeng, J. Dai, W. Yao, D. Xiao, and X. Cui. Valley polarization in MoS_2 monolayers by optical pumping. *Nat Nano* **7**, 490 (2012).

[13] K. F. Mak, K. He, J. Shan, and T. F. Heinz. Control of valley polarization in monolayer MoS_2 by optical helicity. *Nat Nano* **7**, 494 (2012).

[14] C. R. Dean, A. F. Young, I. Meric, C. Lee, L. Wang, S. Sorgenfrei, K. Watanabe, T. Taniguchi, P. Kim, K. L. Shepard, and J. Hone. Boron nitride substrates for high-quality graphene electronics. *Nat Nano* **5**, 722 (2010).

[15] L. Britnell, R. V. Gorbachev, R. Jalil, B. D. Belle, F. Schedin, A. Mishchenko, T. Georgiou, M. I. Katsnelson, L. Eaves, S. V. Morozov, N. M. R. Peres, J. Leist, A. K. Geim, K. S. Novoselov, and L. A. Ponomarenko. Field-effect tunneling transistor based on vertical graphene heterostructures. *Science* **335**, 947 (2012).

[16] L. Britnell, R. V. Gorbachev, R. Jalil, B. D. Belle, F. Schedin, M. I. Katsnelson, L. Eaves, S. V. Morozov, A. S. Mayorov, N. M. R. Peres, A. H. Castro Neto, J. Leist, A. K. Geim, L. A. Ponomarenko, and K. S. Novoselov. Electron tunneling through ultrathin boron nitride crystalline barriers. *Nano Letters* **12**, 1707 (2012).

[17] L. Britnell, R. V. Gorbachev, A. K. Geim, L. A. Ponomarenko, A. Mishchenko, M. T. Greenaway, T. M. Fromhold, K. S. Novoselov, and L. Eaves. Resonant tunnelling and negative differential conductance in graphene transistors. *Nat Commun* **4**, 1794 (2013).

[18] A. Mishchenko, Tu J. S., Y. Cao, R. V. Gorbachev, J. R. Wallbank, M. T.

Greenaway, V. E. Morozov, S. V. Morozov, M. J. Zhu, S. L. Wong, F. Withers, C. R. Woods, Y.-J. Kim, K. Watanabe, T. Taniguchi, E. E. Vdovin, O. Makarovsky, T. M. Fromhold, V.I. Fal'ko, A. K. Geim, L. Eaves, and K. S. Novoselov. Twist-controlled resonant tunnelling in graphene/boron nitride/graphene heterostructures. *Nat Nano* **9**, 808 (2014).

[19] L. Britnell, R. M. Ribeiro, A. Eckmann, R. Jalil, B. D. Belle, A. Mishchenko, Y.-J. Kim, R. V. Gorbachev, T. Georgiou, S. V. Morozov, A. N. Grigorenko, A. K. Geim, C. Casiraghi, A. H. Castro Neto, and K. S. Novoselov. Strong light-matter interactions in heterostructures of atomically thin films. *Science* **340**, 1311 (2013).

[20] W. J. Yu, Y. Liu, H. Zhou, A. Yin, Z. Li, Y. Huang, and X. Duan. Highly efficient gate-tunable photocurrent generation in vertical heterostructures of layered materials. *Nat Nano* **8**, 952 (2013).

[21] R. V. Gorbachev, A. K. Geim, M. I. Katsnelson, K. S. Novoselov, T. Tudorovskiy, I. V. Grigorieva, A. H. MacDonald, S. V. Morozov, K. Watanabe, T. Taniguchi, and L. A. Ponomarenko. Strong coulomb drag and broken symmetry in double-layer graphene. *Nat Phys* **8**, 896 (2012).

[22] L. A. Ponomarenko, A. K. Geim, A. A. Zhukov, R. Jalil, S. V. Morozov, K. S. Novoselov, I. V. Grigorieva, E. H. Hill, V. V. Cheianov, V. I. Fal'ko, K. Watanabe, T. Taniguchi, and R. V. Gorbachev. Tunable metal-insulator transition in double-layer graphene heterostructures. *Nat Phys* **7**, 958 (2011).

[23] G. Li, A. Luican, J. M. B. Lopes dos Santos, A. H. Castro Neto, A. Reina, J. Kong, and E. Y. Andrei. Observation of van Hove singularities in twisted graphene layers. *Nat Phys* **6**, 109 (2010).

[24] A. Luican, G. Li, A. Reina, J. Kong, R. R. Nair, K. S. Novoselov, A. K. Geim, and E. Y. Andrei. Single-layer behavior and its breakdown in twisted graphene layers. *Phys. Rev. Lett.* **106**, 126802 (2011).

[25] B. Hunt, J. D. Sanchez-Yamagishi, A. F. Young, M. Yankowitz, B. J. LeRoy,

K. Watanabe, T. Taniguchi, P. Moon, M. Koshino, P. Jarillo-Herrero, and R. C. Ashoori. Massive Dirac fermions and Hofstadter butterfly in a van der Waals heterostructure. *Science* **340**, 1427 (2013).

[26] C. R. Woods, L. Britnell, A. Eckmann, R. S. Ma, J. C. Lu, H. M. Guo, X. Lin, G. L. Yu, Y. Cao, R. V. Gorbachev, A. V. Kretinin, J. Park, L. A. Ponomarenko, M. I. Katsnelson, Yu. N. Gornostyrev, K. Watanabe, T. Taniguchi, C. Casiraghi, H.-J. Gao, A. K. Geim, and K. S. Novoselov. Commensurate-incommensurate transition in graphene on hexagonal boron nitride. *Nat Phys* **10**, 451 (2014).

[27] Y. Wang, Dillon Wong, A. V. Shytov, V. W. Brar, S. Choi, Q. Wu, H.-Z. Tsai, W. Regan, A. Zettl, R. K. Kawakami, S. G. Louie, L. S. Levitov, and M. F. Crommie. Observing atomic collapse resonances in artificial nuclei on graphene. *Science* **340**, 734 (2013).

[28] V. M. Pereira, J. Nilsson, and A. H. Castro Neto. Coulomb impurity problem in graphene. *Phys. Rev. Lett.* **99**, 166802 (2007).

[29] A. V. Shytov, M. I. Katsnelson, and L. S. Levitov. Vacuum polarization and screening of supercritical impurities in graphene. *Phys. Rev. Lett.* **99**, 236801 (2007).

[30] A. V. Shytov, M. I. Katsnelson, and L. S. Levitov. Atomic collapse and quasi-Rydberg states in graphene. *Phys. Rev. Lett.* **99**, 246802 (2007).

[31] A. H. Castro Neto, F. Guinea, N. M. R. Peres, K. S. Novoselov, and A. K. Geim. The electronic properties of graphene. *Rev. Mod. Phys.* **81**, 109 (2009).

[32] C. W. J. Beenakker. *Colloquium* : Andreev reflection and Klein tunneling in graphene. *Rev. Mod. Phys.* **80**, 1337 (2008).

[33] D. Xiao, M.-C. Chang, and Q. Niu. Berry phase effects on electronic properties. *Rev. Mod. Phys.* **82**, 1959 (2010).

[34] T. Ando and T. Nakanishi. Impurity scattering in carbon nanotubes — absence of back scattering —. *Journal of the Physical Society of Japan* **67**, 1704 (1998).

[35] T. Ando, T. Nakanishi, and R. Saito. Berry's phase and absence of back scat-

tering in carbon nanotubes. *Journal of the Physical Society of Japan* **67**,2857 (1998).

[36] V. V. Cheianov and V. I. Fal'ko. Selective transmission of dirac electrons and ballistic magnetoresistance of n-p junctions in graphene. *Phys. Rev. B* **74**, 041403 (2006).

[37] M. I. Katsnelson, K. S. Novoselov, and A. K. Geim. Chiral tunnelling and the Klein paradox in graphene. *Nat Phys* **2**, 620 (2006).

[38] O. Klein. Die reflexion von elektronen an einem potentialsprung nach der relativistischen dynamik von Dirac. *Zeitschrift für Physik* **53**, 157 (1929).

[39] V. V. Cheianov, V. Fal'ko, and B. L. Altshuler. The focusing of electron flow and a veselago lens in graphene pn junctions. *Science* **315**, 1252 (2007).

[40] J. Martin, N. Akerman, G. Ulbricht, T. Lohmann, J. H. Smet, K. von Klitzing, and A. Yacoby. Observation of electron-hole puddles in graphene using a scanning single-electron transistor. *Nat Phys* **4**, 144 (2008).

[41] Y. Zhang, V. W. Brar, C. Girit, A. Zettl, and M. F. Crommie. Origin of spatial charge inhomogeneity in graphene. *Nat Phys* **5**, 722 (2009).

[42] M. V. Berry. Quantal phase factors accompanying adiabatic changes. *Proceedings of the Royal Society of London A: Mathematical, Physical and Engineering Sciences* **392**, 45 (1984).

[43] F. Wilczek and A. Zee. Appearance of gauge structure in simple dynamical systems. *Phys. Rev. Lett.* **52**, 2111 (1984).

[44] I. Crassee, J. Levallois, A. L. Walter, M. Ostler, A. Bostwick, E. Rotenberg, T. Seyller, D. van der Marel, and A. B. Kuzmenko. Giant Faraday rotation in single- and multilayer graphene. *Nat Phys* **7**, 48 (2011).

[45] R. Shimano, G. Yumoto, J. Y. Yoo, R. Matsunaga, S. Tanabe, H. Hibino, T. Morimoto, and H. Aoki. Quantum Faraday and Kerr rotations in graphene. *Nat Commun* **4**, 1841 (2013).

[46] A. N. Grigorenko, M. Polini, and K. S. Novoselov. Graphene plasmonics. *Nat Photon* **6**, 749 (2012).

[47] R. Bistritzer and A. H. MacDonald. Electronic cooling in graphene. *Phys. Rev. Lett.* **102**, 206410 (2009).

[48] W.-K. Tse and S. Das Sarma. Energy relaxation of hot Dirac fermions in graphene. *Phys. Rev. B* **79**, 235406 (2009).

[49] X. Xu, N. M. Gabor, J. S. Alden, A. M. van der Zande, and P. L. McEuen. Photo-thermoelectric effect at a graphene interface junction. *Nano Letters* **10**, 562 (2010).

[50] M. C. Lemme, F. H. L. Koppens, A. L. Falk, M. S. Rudner, H. Park, L. S. Levitov, and C. M. Marcus. Gate-activated photoresponse in a graphene pn junction. *Nano Letters* **11**, 4134 (2011).

[51] N. M. Gabor, J. C. W. Song, Q. Ma, N. L. Nair, T. Taychatanapat, K. Watanabe, T. Taniguchi, L. S. Levitov, and P. Jarillo-Herrero. Hot carrier–assisted intrinsic photoresponse in graphene. *Science* **334**, 648 (2011).

[52] J. C. W. Song, M. Y. Reizer, and L. S. Levitov. Disorder-assisted electron-phonon scattering and cooling pathways in graphene. *Phys. Rev. Lett.* **109**, 106602 (2012).

[53] A. K. Geim and I. V. Grigorieva. Van der Waals heterostructures. *Nature* **499**, 419 (2013).

[54] C.-C. Chen, M. Aykol, C.-C. Chang, A. F. J. Levi, and S. B. Cronin. Graphene-silicon Schottky diodes. *Nano Letters* **11**, 1863 (2011).

[55] H. Yang, J. Heo, S. Park, H. J. Song, D. H. Seo, K.-E. Byun, P. Kim, I. Yoo, H.-J. Chung, and K. Kim. Graphene barristor, a triode device with a gate-controlled schottky barrier. *Science* **336**, 1140 (2012).

[56] X. Wang, Z. Cheng, K. Xu, H. K. Tsang, and J.-B. Xu. High-responsivity graphene/silicon-heterostructure waveguide photodetectors. *Nat Photon* **7**, 888 (2013).

[57] X. Miao, S. Tongay, M. K. Petterson, K. Berke, A. G. Rinzler, B. R. Appleton, and A. F. Hebard. High efficiency graphene solar cells by chemical doping. *Nano Letters* **12**, 2745 (2012).

[58] X. Li, H. Zhu, K. Wang, A. Cao, J. Wei, C. Li, Y. Jia, Z. Li, X. Li, and D. Wu. Graphene-on-silicon Schottky junction solar cells. *Advanced Materials* **22**, 2743 (2010).

[59] T. Georgiou, R. Jalil, B. D. Belle, L. Britnell, R. V. Gorbachev, S. V. Morozov, Y.-J. Kim, A. Gholinia, S. J. Haigh, O. Makarovsky, L. Eaves, L. A. Ponomarenko, A. K. Geim, K. S. Novoselov, and A. Mishchenko. Vertical field-effect transistor based on graphene-WS_2 heterostructures for flexible and transparent electronics. *Nat Nano* **8**, 100 (2013).

[60] W. J. Yu, Z. Li, H. Zhou, Y. Chen, Y. Wang, Y. Huang, and X. Duan. Vertically stacked multi-heterostructures of layered materials for logic transistors and complementary inverters. *Nat Mater* **12**, 246 (2013).

[61] C. Herring and M. H. Nichols. Thermionic emission. *Rev. Mod. Phys.* **21**, 185 (1949).

[62] S. Luryi. Quantum capacitance devices. *Applied Physics Letters* **52**, 501 (1988).

[63] H.-S. P. Wong and S. Salahuddin. Memory leads the way to better computing. *Nat Nano* **10**, 191 (2015).

[64] A. J. Hong, E. B. Song, H. Suk Yu, M. J. Allen, J. Kim, J. D. Fowler, J. K. Wassei, Y. Park, Y. Wang, J. Zou, R. B. Kaner, B. H. Weiller, and K. L. Wang. Graphene flash memory. *ACS Nano* **5**, 7812 (2011).

[65] S. Bertolazzi, D. Krasnozhon, and A. Kis. Nonvolatile memory cells based on MoS_2/graphene heterostructures. *ACS Nano* **7**, 3246 (2013).

[66] X. Wang, W. Xie, J. Du, C. Wang, N. Zhao, and J.-B. Xu. Graphene/metal contacts: Bistable states and novel memory devices. *Advanced Materials* **24**, 2614 (2012).

[67] Y. J. Shin, J. H. Kwon, G. Kalon, K.-T. Lam, C. S. Bhatia, G. Liang, and

H. Yang. Ambipolar bistable switching effect of graphene. *Applied Physics Letters* **97**, 262105 (2010).

[68] Y. Zheng, G.-X. Ni, C.-T. Toh, M.-G. Zeng, S.-T. Chen, K. Yao, and B. zyilmaz. Gate-controlled nonvolatile graphene-ferroelectric memory. *Applied Physics Letters* **94**, 163505 (2009).

[69] D. B. Strukov, G. S. Snider, D. R. Stewart, and R. S. Williams. The missing memristor found. *Nature* **453**, 80 (2008).

[70] J. J. Yang, D. B. Strukov, and D. R. Stewart. Memristive devices for computing. *Nat Nano* **8**, 13 (2013).

[71] A. D. Kent and D. C. Worledge. A new spin on magnetic memories. *Nat Nano* **10**, 187 (2015).

[72] R. Tsu and L. Esaki. Tunneling in a finite superlattice. *Applied Physics Letters* **22**, 562 (1973).

[73] V. J. Goldman, D. C. Tsui, and J. E. Cunningham. Observation of intrinsic bistability in resonant tunneling structures. *Phys. Rev. Lett.* **58**, 1256 (1987).

[74] A. Zaslavsky, V. J. Goldman, D. C. Tsui, and J. E. Cunningham. Resonant tunneling and intrinsic bistability in asymmetric doublebarrier heterostructures. *Applied Physics Letters* **53**, 1408 (1988).

[75] P. A. George, J. Strait, J. Dawlaty, S. Shivaraman, M. Chandrashekhar, F. Rana, and M. G. Spencer. Ultrafast optical-pump terahertz-probe spectroscopy of the carrier relaxation and recombination dynamics in epitaxial graphene. *Nano Letters* **8**, 4248 (2008).

[76] J. M. B. Lopes dos Santos, N. M. R. Peres, and A. H. Castro Neto. Graphene bilayer with a twist: Electronic structure. *Phys. Rev. Lett.* **99**, 256802 (2007).

[77] R. Bistritzer and A. H. MacDonald. Transport between twisted graphene layers. *Phys. Rev. B* **81**, 245412 (2010).

[78] R. Bistritzer and A. H. MacDonald. Moiré bands in twisted double-layer

graphene. *Proceedings of the National Academy of Sciences* **108**, 12233 (2011).

[79] L. Brey. Coherent tunneling and negative differential conductivity in a graphene/h-bn/graphene heterostructure. *Phys. Rev. Applied* **2**, 014003 (2014).

[80] J. Bardeen. Tunnelling from a many-particle point of view. *Phys. Rev. Lett.* **6**, 57 (1961).

[81] E. L. Wolf. *Principles of Electron Tunneling Spectroscopy: Second Edition.* Oxford University Press, 2nd edition (2011).

[82] F. Bonaccorso, Z. Sun, T. Hasan, and A. C. Ferrari. Graphene photonics and optoelectronics. *Nat Photon* **4**, 611 (2010).

[83] Q. Bao and K. P. Loh. Graphene photonics, plasmonics, and broadband optoelectronic devices. *ACS Nano* **6**, 3677 (2012).

[84] F. Xia, T. Mueller, Y.-M. Lin, A. Valdes-Garcia, and P. Avouris. Ultrafast graphene photodetector. *Nat Nano* **4**, 839 (2009).

[85] R. R. Nair, P. Blake, A. N. Grigorenko, K. S. Novoselov, T. J. Booth, T. Stauber, N. M. R. Peres, and A. K. Geim. Fine structure constant defines visual transparency of graphene. *Science* **320**, 1308 (2008).

[86] P. N. Butcher. The Gunn effect. *Reports on Progress in Physics* **30**, 97 (1967).

[87] T. C. L. G. Sollner, W. D. Goodhue, P. E. Tannenwald, C. D. Parker, and D. D. Peck. Resonant tunneling through quantum wells at frequencies up to 2.5 Thz. *Applied Physics Letters* **43**, 588 (1983).

[88] N. Kharche and S. K. Nayak. Quasiparticle band gap engineering of graphene and graphone on hexagonal boron nitride substrate. *Nano Letters* **11**, 5274 (2011).

[89] Z. Sun, T. Hasan, F. Torrisi, D. Popa, G. Privitera, F. Wang, F. Bonaccorso, D. M. Basko, and A. C. Ferrari. Graphene mode-locked ultrafast laser. *ACS Nano* **4**, 803 (2010).

[90] J. Xue, J. Sanchez-Yamagishi, D. Bulmash, P. Jacquod, A. Deshpande,

K. Watanabe, T. Taniguchi, P. Jarillo-Herrero, and B. J. LeRoy. Scanning tunnelling microscopy and spectroscopy of ultra-flat graphene on hexagonal boron nitride. *Nat Mater* **10**, 282 (2011).

[91] M. W. Graham, S.-F. Shi, D. C. Ralph, J. Park, and P. L. McEuen. Photocurrent measurements of supercollision cooling in graphene. *Nat Phys* **9**, 103 (2013).

[92] A. C. Betz, S. H. Jhang, E. Pallecchi, R. Ferreira, G. Feve, J.-M. Berroir, and B. Placais. Supercollision cooling in undoped graphene. *Nat Phys* **9**, 109 (2013).

[93] K. J. Tielrooij, J. C. W. Song, S. A. Jensen, A. Centeno, A. Pesquera, A. Zurutuza Elorza, M. Bonn, L. S. Levitov, and F. H. L. Koppens. Photoexcitation cascade and multiple hot-carrier generation in graphene. *Nat Phys* **9**, 248 (2013).

[94] J. C. W. Song, K. J. Tielrooij, F. H. L. Koppens, and L. S. Levitov. Photoexcited carrier dynamics and impact-excitation cascade in graphene. *Phys. Rev. B* **87**, 155429 (2013).

[95] S. M. Sze. *The physics of semiconductor devices.* Wiley (2007).

[96] K. Rajkanan, R. Singh, and J. Shewchun. Absorption coefficient of silicon for solar cell calculations. *Solid-State Electronics* **22**, 793 (1979).

[97] H. Yan, T. Low, W. Zhu, Y. Wu, M. Freitag, X. Li, F. Guinea, P. Avouris, and F. Xia. Damping pathways of mid-infrared plasmons in graphene nanostructures. *Nat Photon* **7**, 394 (2013).

[98] J. F. Rodriguez-Nieva, M. S. Dresselhaus, and L. S. Levitov. Thermionic emission and negative di/dv in photoactive graphene heterostructures. *Nano Letters* **15**, 1451 (2015).

[99] J. R. Goldman and J. A. Prybyla. Ultrafast dynamics of laser-excited electron distributions in Silicon. *Phys. Rev. Lett.* **72**, 1364 (1994).

[100] K. S. Novoselov, A. K. Geim, S. V. Morozov, D. Jiang, M. I. Katsnelson, I. V. Grigorieva, S. V. Dubonos, and A. A. Firsov. Two-dimensional gas of massless dirac fermions in graphene. *Nature* **438**, 197 (2005).

[101] A. V. Shytov, M. S. Rudner, and L. S. Levitov. Klein backscattering and Fabry-Pérot interference in graphene heterojunctions. *Phys. Rev. Lett.* **101**, 156804 (2008).

[102] W. L. Chan, J. Deibel, and D. M. Mittleman. Imaging with terahertz radiation. *Reports on Progress in Physics* **70**, 1325 (2007).

[103] A. Rogalski. *Infrared Detectors.* CRC Press, 2 edition (2010).

[104] Y. Zhao, J. Wyrick, F. D. Natterer, J. F. Rodriguez-Nieva, C. Lewandowski, K. Watanabe, T. Taniguchi, L. S. Levitov, N. B. Zhitenev, and J. A. Stroscio. Creating and probing electron whispering-gallery modes in graphene. *Science* **348**, 672 (2015).

[105] M. F. Crommie, C. P. Lutz, and D. M. Eigler. Confinement of electrons to quantum corrals on a metal surface. *Science* **262**, 218 (1993).

[106] A. F. Young and P. Kim. Quantum interference and Klein tunnelling in graphene heterojunctions. *Nat Phys* **5**, 222 (2009).

[107] A. Varlet, M.-H. Liu, V. Krueckl, D. Bischoff, P. Simonet, K. Watanabe, T. Taniguchi, K. Richter, K. Ensslin, and T. Ihn. Fabry-Pérot interference in gapped bilayer graphene with broken anti-klein tunneling. *Phys. Rev. Lett.* **113**, 116601 (2014).

[108] L. C. Campos, A. F. Young, K. Surakitbovorn, K. Watanabe, T. Taniguchi, and P. Jarillo-Herrero. Quantum and classical confinement of resonant states in a trilayer graphene Fabry-Pérot interferometer. *Nat Commun* **3**, 1239 (2012).

[109] C.-H. Park, Y.-W. Son, L. Yang, M. L. Cohen, and S. G. Louie. Electron beam supercollimation in graphene superlattices. *Nano Letters* **8**, 2920 (2008).

[110] J. R. Williams, T. Low, M. S. Lundstrom, and C. M. Marcus. Gate-controlled guiding of electrons in graphene. *Nat Nano* **6**, 222 (2011).

[111] K. J. Vahala. Optical microcavities. *Nature* **424**, 839 (2003).

[112] A. B. Matsko and V. S. Ilchenko. Optical resonators with whispering gallery

modes I: basics. *IEEE J. Sel. Top. Quantum Electron* **12**, 3 (2006).

[113] M. Pöllinger, D. O'Shea, F. Warken, and A. Rauschenbeutel. Ultrahigh-Q tunable whispering-gallery-mode microresonator. *Phys. Rev. Lett.* **103**, 053901 (2009).

[114] L. Rayleigh. CXII. the problem of the whispering gallery. *The London, Edinburgh, and Dublin Philosophical Magazine and Journal of Science* **20**, 1001 (1910).

[115] V. V. Nesvizhevsky, A. Yu. Voronin, R. Cubitt, and K. V. Protasov. Neutron whispering gallery. *Nat Phys* **6**, 114 (2010).

[116] G. Reecht, H. Bulou, F. Scheurer, V. Speisser, B. Carrière, F. Mathevet, and G. Schull. Oligothiophene nanorings as electron resonators for whispering gallery modes. *Phys. Rev. Lett.* **110**, 056802 (2013).

[117] J. A. Stroscio and W. J. Kaiser. *Scanning tunneling microscopy*, volume 27. Academic Press (1993).

[118] G. M. Rutter, J. N. Crain, N. P. Guisinger, T. Li, P. N. First, and J. A. Stroscio. Scattering and interference in epitaxial graphene. *Science* **317**, 219 (2007).

[119] S. Jung, G. M. Rutter, N. N. Klimov, D. B. Newell, I. Calizo, A. R. Hight-Walker, N. B. Zhitenev, and J. A. Stroscio. Evolution of microscopic localization in graphene in a magnetic field from scattering resonances to quantum dots. *Nat Phys* **7**, 245 (2011).

[120] J. Chae, S. Jung, A. F. Young, C. R. Dean, L. Wang, Y. Gao, K. Watanabe, T. Taniguchi, J. Hone, K. L. Shepard, P. Kim, N. B. Zhitenev, and J. A. Stroscio. Renormalization of the graphene dispersion velocity determined from scanning tunneling spectroscopy. *Phys. Rev. Lett.* **109**, 116802 (2012).

[121] J. Cserti, A. Pályi, and C. Péterfalvi. Caustics due to a negative refractive index in circular graphene p-n junctions. *Phys. Rev. Lett.* **99**, 246801 (2007).

[122] R. L. Heinisch, F. X. Bronold, and H. Fehske. Mie scattering analog in graphene: Lensing, particle confinement, and depletion of Klein tunneling. *Phys. Rev. B*

87, 155409 (2013).

[123] N. Agrawal, S. Ghosh, and M. Sharma. Scattering of massless Dirac fermions in circular *p-n* junctions with and without magnetic field. *Journal of Physics: Condensed Matter* **26**, 155301 (2014).

[124] J. H. Bardarson, M. Titov, and P. W. Brouwer. Electrostatic confinement of electrons in an integrable graphene quantum dot. *Phys. Rev. Lett.* **102**, 226803 (2009).

[125] H.-Y. Chen, V. Apalkov, and T. Chakraborty. Fock-Darwin states of dirac electrons in graphene-based artificial atoms. *Phys. Rev. Lett.* **98**, 186803 (2007).

[126] P. G. Silvestrov and K. B. Efetov. Quantum dots in graphene. *Phys. Rev. Lett.* **98**, 016802 (2007).

[127] A. Matulis and F. M. Peeters. Quasibound states of quantum dots in single and bilayer graphene. *Phys. Rev. B* **77**, 115423 (2008).

[128] J.-S. Wu and M. M. Fogler. Scattering of two-dimensional massless Dirac electrons by a circular potential barrier. *Phys. Rev. B* **90**, 235402 (2014).

[129] M.-C. Chang and Q. Niu. Berry phase, hyperorbits, and the Hofstadter spectrum: Semiclassical dynamics in magnetic bloch bands. *Phys. Rev. B* **53**, 7010 (1996).

[130] M.-C. Chang and Q. Niu. Berry curvature, orbital moment, and effective quantum theory of electrons in electromagnetic fields. *Journal of Physics: Condensed Matter* **20**, 193202 (2008).

[131] G. Sundaram and Q. Niu. Wave-packet dynamics in slowly perturbed crystals: Gradient corrections and Berry-phase effects. *Phys. Rev. B* **59**, 14915 (1999).

[132] A. D. Stone. Einstein's unknown insight and the problem of quantizing chaos. *Physics Today* **58**, 37 (2005).

[133] V. A. Volkov and S. A. Mikhailov. Edge magnetoplasmons: low frequency weakly damped excitations in inhomogeneous two-dimensional electron systems.

Sov. Phys. JETP **67**, 1639 (1988).

[134] W. Wang, S. P. Apell, and J. M. Kinaret. Edge magnetoplasmons and the optical excitations in graphene disks. *Phys. Rev. B* **86**, 125450 (2012).

[135] I. Crassee, M. Orlita, M. Potemski, A. L. Walter, M. Ostler, Th. Seyller, I. Gaponenko, J. Chen, and A. B. Kuzmenko. Intrinsic terahertz plasmons and magnetoplasmons in large scale monolayer graphene. *Nano Letters* **12**, 2470 (2012).

[136] H. Yan, Z. Li, X. Li, W. Zhu, P. Avouris, and F. Xia. Infrared spectroscopy of tunable Dirac terahertz magneto-plasmons in graphene. *Nano Letters* **12**, 3766 (2012).

[137] I. Petković, F. I. B. Williams, K. Bennaceur, F. Portier, P. Roche, and D. C. Glattli. Carrier drift velocity and edge magnetoplasmons in graphene. *Phys. Rev. Lett.* **110**, 016801 (2013).

[138] A. Ramasubramaniam. Large excitonic effects in monolayers of molybdenum and tungsten dichalcogenides. *Phys. Rev. B* **86**, 115409 (2012).

[139] Q. H. Wang, K. Kalantar-Zadeh, A. Kis, J. N. Coleman, and M. S. Strano. Electronics and optoelectronics of two-dimensional transition metal dichalcogenides. *Nat Nano* **7**, 699 (2012).

[140] X. Xu, W. Yao, D. Xiao, and T. F. Heinz. Spin and pseudospins in layered transition metal dichalcogenides. *Nat Phys* **10**, 343 (2014).

[141] A. Srivastava and A. Imamoğlu. Signatures of bloch-band geometry on excitons: Nonhydrogenic spectra in transition-metal dichalcogenides. *Phys. Rev. Lett.* **115**, 166802 (2015).

[142] J. Zhou, W.-Y. Shan, W. Yao, and D. Xiao. Berry phase modification to the energy spectrum of excitons. *Phys. Rev. Lett.* **115**, 166803 (2015).

[143] S. Zhong, J. Orenstein, and J. E. Moore. Optical gyrotropy from axion electrodynamics in momentum space. *Phys. Rev. Lett.* **115**, 117403 (2015).

[144] A. Kumar, A. Nemilentsau, K. H. Fung, G. Hanson, N. X. Fang, and T. Low. Chiral plasmon in gapped Dirac systems. *Phys. Rev. B* **93**, 041413 (2016).

[145] J. C. W. Song and M. S. Rudner. Chiral plasmons without magnetic field. *Proceedings of the National Academy of Sciences* **113**, 4658 (2016).

[146] A. Jorio, R. Saito, G. Dresselhaus, and M. S. Dresselhaus. *Raman Spectroscopy in Graphene Related Systems*. Wiley-VCH, Berlin (2011).

[147] R. Saito, M. Hofmann, G. Dresselhaus, A. Jorio, and M. S. Dresselhaus. Raman spectroscopy of graphene and carbon nanotubes. *Advances in Physics* **60**, 413 (2011).

[148] A. C. Ferrari and D. M. Basko. Raman spectroscopy as a versatile tool for studying the properties of graphene. *Nat Nano* **8**, 235 (2013).

[149] A. Grüneis, R. Saito, T. Kimura, L. G. Cançado, M. A. Pimenta, A. Jorio, A. G. Souza Filho, G. Dresselhaus, and M. S. Dresselhaus. Determination of two-dimensional phonon dispersion relation of graphite by Raman spectroscopy. *Phys. Rev. B* **65**, 155405 (2002).

[150] A. C. Ferrari. Raman spectroscopy of graphene and graphite: Disorder, electronphonon coupling, doping and nonadiabatic effects. *Solid State Communications* **143**, 47 (2007).

[151] L. M. Malard, M. A. Pimenta, G. Dresselhaus, and M. S. Dresselhaus. Raman spectroscopy in graphene. *Physics Reports* **473**, 51 (2009).

[152] S. Pisana, M. Lazzeri, C. Casiraghi, K. S. Novoselov, A. K. Geim, A. C. Ferrari, and F. Mauri. Breakdown of the adiabatic Born-Oppenheimer approximation in graphene. *Nat Mater* **6**, 198 (2007).

[153] J. Yan, Y. Zhang, P. Kim, and A. Pinczuk. Electric field effect tuning of electron-phonon coupling in graphene. *Phys. Rev. Lett.* **98**, 166802 (2007).

[154] A. C. Ferrari, J. C. Meyer, V. Scardaci, C. Casiraghi, M. Lazzeri, F. Mauri, S. Piscanec, D. Jiang, K. S. Novoselov, S. Roth, and A. K. Geim. Raman spectrum of graphene and graphene layers. *Phys. Rev. Lett.* **97**, 187401 (2006).

[155] L. G. Cançado, M. A. Pimenta, B. R. A. Neves, M. S. S. Dantas, and A. Jorio. Influence of the atomic structure on the Raman spectra of graphite edges. *Phys. Rev. Lett.* **93**, 247401 (2004).

[156] A. K. Gupta, T. J. Russin, H. R. Gutirrez, and P. C. Eklund. Probing graphene edges via Raman scattering. *ACS Nano* **3**, 45 (2009).

[157] C. Casiraghi, A. Hartschuh, H. Qian, S. Piscanec, C. Georgi, A. Fasoli, K. S. Novoselov, D. M. Basko, and A. C. Ferrari. Raman spectroscopy of graphene edges. *Nano Letters* **9**, 1433 (2009).

[158] L. G. Cançado, A. Jorio, E. H. Martins Ferreira, F. Stavale, C. A. Achete, R. B. Capaz, M. V. O. Moutinho, A. Lombardo, T. S. Kulmala, and A. C. Ferrari. Quantifying defects in graphene via Raman spectroscopy at different excitation energies. *Nano Letters* **11**, 3190 (2011).

[159] M. A. Pimenta, G. Dresselhaus, M. S. Dresselhaus, L. G. Cancado, A. Jorio, and R. Saito. Studying disorder in graphite-based systems by Raman spectroscopy. *Phys. Chem. Chem. Phys.* **9**, 1276 (2007).

[160] J. Maultzsch, S. Reich, and C. Thomsen. Double-resonant Raman scattering in graphite: Interference effects, selection rules, and phonon dispersion. *Phys. Rev. B* **70**, 155403 (2004).

[161] C. Thomsen and S. Reich. Double resonant Raman scattering in graphite. *Phys. Rev. Lett.* **85**, 5214 (2000).

[162] R. Saito, A. Jorio, A. G. Souza Filho, G. Dresselhaus, M. S. Dresselhaus, and M. A. Pimenta. Probing phonon dispersion relations of graphite by double resonance Raman scattering. *Phys. Rev. Lett.* **88**, 027401 (2001).

[163] R. Saito, A. Grüneis, Ge. G. Samsonidze, V. W. Brar, G. Dresselhaus, M. S. Dresselhaus, A. Jorio, L. G. Cançado, C. Fantini, M. A. Pimenta, and A. G. Souza Filho. Double resonance Raman spectroscopy of single-wall carbon nanotubes. *New Journal of Physics* **5**, 157 (2003).

[164] S. Reich and C. Thomsen. Raman spectroscopy of graphite. *Philosophical*

Transactions of the Royal Society of London A: Mathematical, Physical and Engineering Sciences **362**, 2271 (2004).

[165] M. S. Dresselhaus, A. Jorio, M. Hofmann, G. Dresselhaus, and R. Saito. Perspectives on carbon nanotubes and graphene Raman spectroscopy. *Nano Letters* **10**, 751 (2010).

[166] R. P. Vidano, D. B. Fischbach, L. J. Willis, and T. M. Loehr. Observation of Raman band shifting with excitation wavelength for carbons and graphites. *Solid State Communications* **39**, 341 (1981).

[167] Y. Wang, D. C. Alsmeyer, and R. L. McCreery. Raman spectroscopy of carbon materials: structural basis of observed spectra. *Chemistry of Materials* **2**, 557 (1990).

[168] H. Terrones, R. Lv, M. Terrones, and M. S. Dresselhaus. The role of defects and doping in 2D graphene sheets and 1D nanoribbons. *Reports on Progress in Physics* **75**, 062501 (2012).

[169] E. B. Barros, H. Son, Ge. G. Samsonidze, A. G. Souza Filho, J. Mendes Filho, G. Dresselhaus, and M. S. Dresselhaus. Laser-energy-dependent Raman scattering studies of graphitic foams. *Phys. Rev. B* **76**, 035444 (2007).

[170] A. Eckmann, A. Felten, I. Verzhbitskiy, R. Davey, and C. Casiraghi. Raman study on defective graphene: Effect of the excitation energy, type, and amount of defects. *Phys. Rev. B* **88**, 035426 (2013).

[171] A. Eckmann, A. Felten, A. Mishchenko, L. Britnell, R. Krupke, K. S. Novoselov, and C. Casiraghi. Probing the nature of defects in graphene by Raman spectroscopy. *Nano Letters* **12**, 3925 (2012).

[172] E. H. Martins Ferreira, M. V. O. Moutinho, F. Stavale, M. M. Lucchese, R. B. Capaz, C. A. Achete, and A. Jorio. Evolution of the Raman spectra from single-, few-, and many-layer graphene with increasing disorder. *Phys. Rev. B* **82**, 125429 (2010).

[173] M. M. Lucchese, F. Stavale, E. H. Martins Ferreira, C. Vilani, M. V. O.

Moutinho, R. B. Capaz, C. A. Achete, and A. Jorio. Quantifying ion-induced defects and Raman relaxation length in graphene. *Carbon* **48**, 1592 (2010).

[174] P. Venezuela, M. Lazzeri, and F. Mauri. Theory of double-resonant Raman spectra in graphene: Intensity and line shape of defect-induced and two-phonon bands. *Phys. Rev. B* **84**, 035433 (2011).

[175] E. B. Barros, K. Sato, Ge. G. Samsonidze, A. G. Souza Filho, M. S. Dresselhaus, and R. Saito. D-band Raman intensity calculation in armchair edged graphene nanoribbons. *Phys. Rev. B* **83**, 245435 (2011).

[176] K. Sato, R. Saito, Y. Oyama, J. Jiang, L. G. Canado, M. A. Pimenta, A. Jorio, Ge. G. Samsonidze, G. Dresselhaus, and M. S. Dresselhaus. D-band Raman intensity of graphitic materials as a function of laser energy and crystallite size. *Chemical Physics Letters* **427**, 117 (2006).

[177] J. F. Rodriguez-Nieva, R. Saito, S. D. Costa, and M. S. Dresselhaus. Effect of ^{13}C isotope doping on the optical phonon modes in graphene: localization and Raman spectroscopy. *Phys. Rev. B* **85**, 245406 (2012).

[178] D. M. Basko. Theory of resonant multiphonon Raman scattering in graphene. *Phys. Rev. B* **78**, 125418 (2008).

[179] D. M. Basko. Effect of inelastic collisions on multiphonon Raman scattering in graphene. *Phys. Rev. B* **76**, 081405 (2007).

[180] D. M. Basko. Boundary problems for dirac electrons and edge-assisted Raman scattering in graphene. *Phys. Rev. B* **79**, 205428 (2009).

[181] C.-H. Park, F. Giustino, M. L. Cohen, and S. G. Louie. Velocity renormalization and carrier lifetime in graphene from the electron-phonon interaction. *Phys. Rev. Lett.* **99**, 086804 (2007).

[182] K. Ishikawa and T. Ando. Optical phonon interacting with electrons in carbon nanotubes. *Journal of the Physical Society of Japan* **75**, 084713 (2006).

[183] K. Sasaki and R. Saito. Pseudospin and deformation-induced gauge field in graphene. *Progress of Theoretical Physics Supplement* **176**, 253 (2008).

[184] H. Suzuura and T. Ando. Zone-boundary phonon in graphene and nanotube. *Journal of the Physical Society of Japan* **77**, 044703 (2008).

[185] A. J. Stone and D. J. Wales. Theoretical studies of icosahedral C60 and some related species. *Chemical Physics Letters* **128**, 501 (1986).

[186] S. Piscanec, M. Lazzeri, F. Mauri, A. C. Ferrari, and J. Robertson. Kohn anomalies and electron-phonon interactions in graphite. *Phys. Rev. Lett.* **93**, 185503 (2004).

[187] J. Jiang, R. Saito, Ge. G. Samsonidze, S. G. Chou, A. Jorio, G. Dresselhaus, and M. S. Dresselhaus. Electron-phonon matrix elements in single-wall carbon nanotubes. *Phys. Rev. B* **72**, 235408 (2005).